

Cosmological parameter constraints from galaxy–galaxy lensing and galaxy clustering with the SDSS DR7

Rachel Mandelbaum,^{1,2*} Anže Slosar,³ Tobias Baldauf,⁴ Uroš Seljak,^{4,5,6,7}
Christopher M. Hirata,⁸ Reiko Nakajima,⁹ Reinabelle Reyes¹⁰ and Robert E. Smith^{4,9}

¹*Peyton Hall Observatory, Princeton University, Peyton Hall, Princeton, NJ 08544, USA*

²*Department of Physics, Carnegie Mellon University, Pittsburgh, PA 15213, USA*

³*Brookhaven National Laboratory, Upton, NY 11375, USA*

⁴*Institute for Theoretical Physics, University of Zurich, 8057 Zurich, Switzerland*

⁵*Space Sciences Lab, Department of Physics and Department of Astronomy, University of California, Berkeley, CA 94720, USA*

⁶*Lawrence Berkeley National Lab, University of California, Berkeley, CA 94720, USA*

⁷*Institute of the Early Universe, Ewha Womans University, Seoul 120-750, Korea*

⁸*Department of Astronomy, Caltech M/C 350-17, Pasadena, CA 91125, USA*

⁹*Argelander-Institut für Astronomie, Universität Bonn, D-53121 Bonn, Germany*

¹⁰*Kavli Institute for Cosmological Physics and Enrico Fermi Institute, University of Chicago, Chicago, IL 60637, USA*

Accepted 2013 March 30. Received 2013 March 8; in original form 2012 July 5

ABSTRACT

Recent studies have shown that the cross-correlation coefficient between galaxies and dark matter is very close to unity on scales outside a few virial radii of galaxy haloes, independent of the details of how galaxies populate dark matter haloes. This finding makes it possible to determine the dark matter clustering from measurements of galaxy–galaxy weak lensing and galaxy clustering. We present new cosmological parameter constraints based on large-scale measurements of spectroscopic galaxy samples from the Sloan Digital Sky Survey (SDSS) data release 7. We generalize the approach of Baldauf et al. to remove small-scale information (below 2 and 4 h^{-1} Mpc for lensing and clustering measurements, respectively), where the cross-correlation coefficient differs from unity. We derive constraints for three galaxy samples covering 7131 deg², containing 69 150, 62 150 and 35 088 galaxies with mean redshifts of 0.11, 0.28 and 0.40. We clearly detect scale-dependent galaxy bias for the more luminous galaxy samples, at a level consistent with theoretical expectations. When we vary both σ_8 and Ω_m (and marginalize over non-linear galaxy bias) in a flat Λ cold dark matter model, the best-constrained quantity is $\sigma_8(\Omega_m/0.25)^{0.57} = 0.80 \pm 0.05$ (1σ , stat. + sys.), where statistical and systematic errors (photometric redshift and shear calibration) have comparable contributions, and we have fixed $n_s = 0.96$ and $h = 0.7$. These strong constraints on the matter clustering suggest that this method is competitive with cosmic shear in current data, while having very complementary and in some ways less serious systematics. We therefore expect that this method will play a prominent role in future weak lensing surveys. When we combine these data with *Wilkinson Microwave Anisotropy Probe 7-year (WMAP7)* cosmic microwave background (CMB) data, constraints on σ_8 , Ω_m , H_0 , w_{de} and $\sum m_\nu$ become 30–80 per cent tighter than with CMB data alone, since our data break several parameter degeneracies.

Key words: gravitational lensing: weak – cosmological parameters – cosmology: observations – large-scale structure of Universe.

1 INTRODUCTION

The currently accepted cosmological model that is broadly consistent with multiple observations, known as Λ cold dark matter

(Λ CDM), is dominated by dark ingredients: dark matter, which we observe through its gravitational effects, and dark energy, the presence of which was inferred due to the accelerated expansion of our Universe as detected using supernovae (Riess et al. 1998; Perlmutter et al. 1999). Further attempts to constrain this model, such as those described by the Dark Energy Task Force (Albrecht et al.

*E-mail: rmandelb@andrew.cmu.edu

2006), rely on observational methods that can broadly be classified in two ways: *geometric* measurements such as supernovae (standard candles) and baryon acoustic oscillations (BAO, standard rulers), and measurements of large-scale *structure growth*. The latter measurements of structure growth – particularly as a function of time – can constrain the initial amplitude of matter fluctuations, the matter density and even the nature of dark energy; the scale dependence of structure growth can be used to constrain the neutrino mass.

Theoretical predictions for structure growth, such as from perturbation theory or N -body simulations, are cleanest when expressed in terms of fluctuations in the density of dark matter. Fortunately, weak gravitational lensing provides us with a way of observing the total matter density (including dark matter), via the deflections of light due to intervening matter along the line of sight, which both magnifies and distorts galaxy shapes (for a review, see Bartelmann & Schneider 2001; Refregier 2003; Hoekstra & Jain 2008; Massey, Kitching & Richard 2010). The lensing measurement that is commonly used to constrain the amplitude and growth of matter fluctuations is ‘cosmic shear’, the autocorrelation of galaxy shape distortions due to intervening matter along the line of sight. Since the initial detections of cosmic shear a decade ago (Bacon, Refregier & Ellis 2000; Van Waerbeke et al. 2000; Rhodes, Refregier & Groth 2001; Hoekstra et al. 2002), increasingly enlarging data sets and sophisticated measurement techniques have led to steadily decreasing errors, both statistical and systematic (e.g. Schrabback et al. 2010; Heymans et al. 2013).

However, cosmic shear is, by its very nature, a difficult measurement: in the autocorrelation of galaxy shape distortions, coherent systematic errors (such as those induced by seeing or distortions in the telescope) become an additional additive term. Moreover, intrinsic alignments with the local density field that anticorrelate with the real gravitational shear (Hirata & Seljak 2004) can contaminate cosmic shear measurements in ways that are difficult to remove.

Baldauf et al. (2010) provided an alternate approach to constraining the growth of structure using gravitational lensing which is less subject to the aforementioned difficulties. This approach involves the combination of two measurements: the autocorrelation of galaxy positions (galaxy clustering) and the cross-correlation between foreground galaxy positions and background galaxy shears (galaxy–galaxy lensing, which measures the galaxy–mass cross-correlation). By combining these two measurements, we can recover the matter correlation function, the quantity that is most easily predicted by the theory. To reduce uncertainties associated with exactly how galaxies populate dark matter haloes, Baldauf et al. (2010) construct a two-point observable that explicitly eliminates all information below scales equal to a few times the typical dark matter halo virial radius. The use of these two observations allows for a direct measurement of the galaxy bias (the factor relating the matter and the galaxy density fluctuations, which can be both mass and scale dependent), thus eliminating one of the main systematic uncertainties in using galaxy clustering alone to constrain the matter power spectrum, by converting it to a statistical error over which we marginalize when constraining cosmology. This measurement can constrain the amplitude of matter fluctuations at quite low redshift, which is very useful when combined with higher redshift measurements, providing a measure of structure growth in the time when dark energy is most dominant. Also, since it relies on shear cross-correlations rather than autocorrelations, coherent additive errors in galaxy shapes can be removed from the analysis entirely.

This paper is a proof of concept of the method described in Baldauf et al. (2010) to constrain the amplitude of matter fluctuations at $z < 0.4$, using data from the Sloan Digital Sky Survey

(SDSS). For this measurement, we use lens samples that have spectroscopy: one sample of typical galaxies from the SDSS ‘Main’ galaxy sample, and two samples consisting of luminous red galaxies (LRGs), which are commonly used for large-scale structure measurements due to their homogeneous photometric properties, simple selection criteria and the large cosmological volume that they sample. By dividing our sample into three lens samples, we can test for consistency between the results at different redshifts (modulo the expected amount of evolution due to the different mean redshifts). We will demonstrate that even this very shallow survey can constrain the amplitude of matter fluctuations at the ~ 6 per cent level, which is especially cosmologically interesting when combined with cosmic microwave background (CMB) data.

We begin in Section 2 with a more detailed outline of the theoretical background behind the observation we wish to carry out, and simulations that we use for tests of this method. The data that we use are described in Section 3, and our observational methodology in Section 4. The observational results for the galaxy–galaxy lensing are in Section 5 and for the galaxy clustering, in Section 6. We show the resulting constraints on cosmological parameters and on galaxy bias in Section 7, and conclude in Section 8 with perspective on how this method may be used in upcoming surveys that will carry out deep, wide-field lensing observations.

Here, we note the cosmological model and units used in this paper. All estimates of observed quantities assume a flat Λ CDM universe with $\Omega_m = 0.25$, $\Omega_\Lambda = 0.75$; we discuss the implications of this choice in Section 2.3.3. Distances quoted for transverse lens–source separation are comoving h^{-1} Mpc, where $H_0 = 100 h$ km s $^{-1}$ Mpc $^{-1}$. Likewise, $\Delta\Sigma$ is computed using the expression for Σ_c^{-1} in comoving coordinates, equation (7). In the units used, H_0 scales out of everything, so our results are independent of this quantity. Finally, two-dimensional separations are indicated with capital R , three-dimensional radii with lowercase r (occasionally r may denote r -band magnitude as well; this should be clear from context).

2 THEORY

The most basic theory predictions for the growth of structure are phrased in terms of the statistics of the matter distribution – for example, the two-point matter autocorrelation function $\xi_{mm}(\mathbf{r})$ or the power spectrum $P_{mm}(\mathbf{k})$. Here, the matter autocorrelation function is defined in terms of the matter density contrast $\delta_m = \rho_m/\bar{\rho}_m - 1$ as

$$\xi_{mm}(\mathbf{r}) = \langle \delta_m(\mathbf{x})\delta_m^*(\mathbf{x} + \mathbf{r}) \rangle. \quad (1)$$

Perturbation theory is sufficient to predict such statistics of the matter distribution when the perturbations are linear (density contrast $\delta_m \ll 1$); N -body simulations are used to predict the non-linear power spectrum (e.g. Heitmann et al. 2010) in the absence of modifications due to gas physics, which may be significant on the scales used for typical weak lensing analyses (Zhan & Knox 2004; Jing et al. 2006; Rudd, Zentner & Kravtsov 2008; Zentner, Rudd & Hu 2008; Semboloni et al. 2011).

Galaxy redshift surveys allow us to constrain analogous autocorrelation functions for the galaxy density field, $\xi_{gg}(\mathbf{r})$ or $P_{gg}(\mathbf{k})$. Unfortunately, the connection between the theory predictions for the matter statistics to the two-point statistics of the galaxy density field is non-trivial. We can define the relation as

$$\xi_{gg}(r) = b^2(r)\xi_{mm}(r). \quad (2)$$

On large scales, it is possible to use the linear bias approximation, $b(r) = \text{constant}$, where the galaxy bias depends on the mass of the dark matter haloes hosting the galaxies. However, the bias is also scale dependent on smaller scales (Cole et al. 2005; Tinker et al. 2005; Smith, Scoccimarro & Sheth 2007; Sánchez & Cole 2008), $\lesssim 20 h^{-1}$ Mpc, for galaxies in very massive haloes. The existence of galaxy bias causes significant difficulty in inferring the statistics of the underlying matter density field from galaxy redshift surveys; additional information is needed.

Galaxy–galaxy weak lensing provides a simple way to probe the connection between galaxies and matter via their cross-correlation function

$$\xi_{\text{gm}}(\mathbf{r}) = \langle \delta_{\text{g}}(\mathbf{x}) \delta_{\text{m}}^*(\mathbf{x} + \mathbf{r}) \rangle. \quad (3)$$

This cross-correlation can be related to the projected¹ surface density around lensing galaxies

$$\Sigma(R) = \bar{\rho} \int \left[1 + \xi_{\text{gm}} \left(\sqrt{R^2 + \Pi^2} \right) \right] d\Pi, \quad (4)$$

where Π is the line-of-sight separation measured from the lens, and therefore $r^2 = R^2 + \Pi^2$. This surface density is then related to the observable quantity for lensing, the tangential shear distortion γ_t of the shapes of background galaxies, via

$$\Delta \Sigma(R) = \gamma_t(R) \Sigma_c = \bar{\Sigma}(< R) - \Sigma(R), \quad (5)$$

where

$$\bar{\Sigma}(< R) = \frac{2}{R^2} \int_0^R R' dR' \Sigma(R'). \quad (6)$$

When averaging over (‘stacking’) large numbers of lens galaxies to determine the average signal around them, the resulting matter distribution is axisymmetric about the line of sight. The observable quantity $\Delta \Sigma$ can be expressed as the product of two factors, a tangential shear γ_t and a geometric factor

$$\Sigma_c = \frac{c^2}{4\pi G} \frac{D_A(z_s)}{D_A(z_l) D_A(z_l, z_s) (1 + z_L)^2} \quad (7)$$

where $D_A(z_l)$ and $D_A(z_s)$ are angular diameter distances to the lens and source, $D_A(z_l, z_s)$ is the angular diameter distance between the lens and source and the factor of $(1 + z_L)^{-2}$ arises due to our use of comoving coordinates.

Generally, for some two-point statistic ζ (for example, the real-space correlation function ξ or Fourier-space power spectrum $P(k)$), we can relate the three possible two-point correlations that can be constructed out of the matter and galaxy fields, ζ_{mm} , ζ_{gg} and ζ_{gm} , as follows:

$$\zeta_{\text{gm}} = b^{(\zeta)} r_{\text{cc}}^{(\zeta)} \zeta_{\text{mm}}, \quad (8)$$

$$\zeta_{\text{gg}} = b^{(\zeta)2} \zeta_{\text{mm}} = \frac{b^{(\zeta)}}{r_{\text{cc}}^{(\zeta)}} \zeta_{\text{gm}}. \quad (9)$$

All quantities in these equations are a function of scale, where the scale depends on the exact statistic (e.g. 3D r , 2D R , Fourier wavenumber k , multipole ℓ). Here, $b^{(\zeta)}$ is the galaxy bias relating the galaxy and dark matter fluctuations, and $r_{\text{cc}}^{(\zeta)}$, defined as $r_{\text{cc}}^{(\zeta)} = \zeta_{\text{gm}} / \sqrt{\zeta_{\text{mm}} \zeta_{\text{gg}}}$, is the cross-correlation coefficient between the matter and galaxy fluctuations.² Generically, the galaxy bias

tends to a constant value on large scales (‘linear bias’), and the cross-correlation coefficient approaches one, but the rate at which this happens depends on the choice of statistic ζ . In particular, if ζ is defined as a product of either a Fourier mode (i.e. the power spectrum) or of a count in cell (of varying size, called the smoothing size), then $|r_{\text{cc}}^{(\zeta)}| < 1$ (note that no shot-noise subtraction is applied here). In this case, the deviation of $r_{\text{cc}}^{(\zeta)}$ from unity can be related to stochasticity (e.g. Dekel & Lahav 1999), which is defined as

$$\begin{aligned} \langle (\delta_{\text{g}} - b^{(\zeta)} \delta_{\text{m}})^2 \rangle &= \zeta_{\text{gg}} - 2b^{(\zeta)} \zeta_{\text{gm}} + (b^{(\zeta)})^2 \zeta_{\text{mm}} \\ &= 2(b^{(\zeta)})^2 (1 - r_{\text{cc}}^{(\zeta)}) \zeta_{\text{mm}}. \end{aligned} \quad (10)$$

This is zero if $r_{\text{cc}}^{(\zeta)} = 1$. However, the rate at which $r_{\text{cc}}^{(\zeta)}$ approaches unity as a function of either the size of the cell or the wavenumber of the Fourier mode is slow, because stochasticity (such as the shot noise caused by finite number of galaxies) contributes to it. This rate of convergence to unity is even worse if compensated windows with positive and negative weights, such as for the aperture mass statistic, are used (Schneider et al. 1998); this effect has been observed in practice by, e.g. Simon et al. (2009) and Jullo et al. (2012).

On the other hand, ζ can be defined as a correlation function, as in equation (1), not as a product of a field with itself (or another field), in which case the shot noise does not explicitly contribute to it except at zero lag. A related statistic in Fourier space is the shot-noise-subtracted power spectrum, where stochasticity is explicitly subtracted. In this case, as shown in Baldauf et al. (2010), $r_{\text{cc}}^{(\zeta)}$ is much closer to unity (except at zero lag) and the scale dependence of $b^{(\zeta)}$ is significantly reduced (which is why shot-noise subtraction is a standard procedure in the analysis of the galaxy power spectrum). Moreover, even on scales where $b^{(\zeta)}$ is strongly scale dependent, $r_{\text{cc}}^{(\zeta)}$ is close to unity, with deviations from unity of only a few per cent on scales above $3 h^{-1}$ Mpc, where the scale-dependent bias can be tens of per cent. In this case, $r_{\text{cc}}^{(\zeta)}$ has no relation to stochasticity, since its contribution does not enter or is explicitly subtracted from it, and we no longer need to have $|r_{\text{cc}}^{(\zeta)}| < 1$.

If we can ensure that we are working in a regime where the cross-correlation $r_{\text{cc}}^{(\zeta)} \approx 1$, or, more generally, if we have a robust model for its scale dependence, then we can infer the combination of the mean matter density and the correlation statistic of matter by combining the galaxy–galaxy lensing and galaxy clustering statistics. Note that the galaxy–galaxy lensing observable is not sensitive to just ζ_{gm} , but rather to $\bar{\rho}_{\text{m}} \zeta_{\text{gm}}$ (e.g. see equation 4), so this combination of observables gives

$$\bar{\rho}_{\text{m}}^2 \frac{\zeta_{\text{gm}}^2}{\zeta_{\text{gg}}} = \bar{\rho}_{\text{m}}^2 [r_{\text{cc}}^{(\zeta)}]^2 \zeta_{\text{mm}}. \quad (11)$$

As a result, on fully linear scales, g–g lensing and clustering together would constrain the product $\sigma_8 \Omega_{\text{m}}$; since the majority of analyses (including ours) have substantial constraining power in the non-linear regime, this changes the best-constrained parameter combination to $\sim \sigma_8 \Omega_{\text{m}}^{0.6}$.

So far, this discussion has been fairly general. Baldauf et al. (2010) carried out a detailed exploration of the behaviour of $r_{\text{cc}}^{(\zeta)}$ for a variety of statistics ζ , using a simulated sample of LRGs residing in dark matter haloes with masses $\gtrsim 3 \times 10^{13} h^{-1} M_{\odot}$, at $z = 0.23$. As shown there, a key point in determining the optimal statistic ζ is that we want to avoid information from within the halo virial radius, because those are the scales for which the correlation coefficient is intrinsically quite different from unity in a way that cannot be predicted from first principles (without some detailed model for how galaxies populate dark matter haloes). The observed lensing signal $\Delta \Sigma$ is therefore quite non-optimal from the perspective of

¹ In equation (4), we ignore the radial lensing window, which is so broad as to be insignificant on all but the largest scales, as was demonstrated explicitly in the context of this method by Baldauf et al. (2010).

² This statistic is often denoted by r . We use the subscript ‘cc’ to avoid confusion with 3D length-scales.

wanting to do cosmology using large scales only, because as shown in equations (5) and (6), at a given R it depends on the surface density of matter around galaxies all the way from $R = 0$.

The statistic that was proposed by Baldauf et al. (2010) and Mandelbaum et al. (2010) to remove small-scale information is known as the annular differential surface density (ADSD) Υ , defined as

$$\Upsilon(R; R_0) = \Delta\Sigma(R) - \left(\frac{R_0}{R}\right)^2 \Delta\Sigma(R_0) \quad (12)$$

$$\begin{aligned} &= \frac{2}{R^2} \int_{R_0}^R dR' R' \Sigma(R') \\ &\quad - \frac{1}{R^2} [R^2 \Sigma(R) - R_0^2 \Sigma(R_0)]. \end{aligned} \quad (13)$$

This statistic depends not only on projected separation R , but also on some scale R_0 ; as demonstrated in equation (13), $\Upsilon(R; R_0)$ is completely lacking any information from below R_0 . We thus have to choose a value of R_0 that is appropriate for our particular application. We will consider several R_0 values in this paper, but generally we would like this to be a few times the typical dark matter halo virial radius (a point that we examine in more detail in Section 2.4). As demonstrated in detail in Baldauf et al. (2010), the advantages of such a choice are that (a) the correlation coefficient $r_{cc}^{(\Upsilon)} \sim 1$ for all scales $R \geq R_0$, and (b) the few per cent deviations from 1 can be calculated quite accurately via perturbation theory (which is only applicable in this regime outside of halo virial radii). It was shown that the deviations of r_{cc} from unity can be described well with one free parameter related to non-linearity of the bias, b_2 . In this paper, we allow the data (specifically galaxy autocorrelations) to determine b_2 , which will in turn determine the small deviations of r_{cc} from unity. In addition, because Υ is a partially compensated statistic, it is not very susceptible to issues that can plague the projected correlation function (w_{gg}) such as sampling variance from large-scale modes uniformly shifting w_{gg} up or down.

The approach described here, which entails removing small-scale information completely, is a conservative approach that minimizes systematic uncertainties due to all the things we do not know on small scales (how galaxies populate dark matter haloes, baryonic effects on the matter power spectrum, etc.) at the expense of increasing the statistical errors. Baryonic effects are generally considered to be small above scales of several h^{-1} Mpc; however, there are studies that claim that baryonic effects can change the matter power spectrum even by ~ 10 per cent at $k = 1 h \text{ Mpc}^{-1}$ (van Daalen et al. 2011), because baryons may be expelled from haloes due to some mechanism such as AGN feedback, redistributing the dark matter potentially to several virial radii. While a detailed study of the implications for our work would require a comparison of the correlation functions, we note that given the correspondence $r \sim 1/k$ (for broad-band power) it is generally the case that this ~ 10 per cent contamination at $k = 1 h \text{ Mpc}^{-1}$ should correspond to $r = 1 h^{-1} \text{ Mpc}$ scales, which we do not use in our analysis. Our minimum $r = R_0$ that is several times larger means that the relevant effect from that paper is the ~ 1 per cent contamination that they find at $k \sim 0.3 h \text{ Mpc}^{-1}$; this is comparable to our other theoretical uncertainties and well below our observational uncertainties, so it does not have to be modelled directly. Alternatively, one can see this from the fact that the physical arguments given in that work suggest deviations in the power spectrum up to $\sim 2r_{\text{vir}}$, whereas the scales we have chosen are typically $> 3r_{\text{vir}}$ for the halo masses in our sample. Future studies with increased statistical precision may find it necessary to model this effect on the correlation function directly. It is also worth con-

sidering the mass dependence of this effect, which is lower for more massive haloes (McCarthy et al. 2011) and could thus influence the choice of which galaxy samples to use for these analyses.

This point about baryonic effects is another issue for which our method should be contrasted with cosmic shear. The problem caused by baryonic effects is exacerbated with shear–shear analyses since they are not localized to a given redshift, so that a given transverse physical scale can translate into a very large angular scale if these galaxies are nearby. In our case, we can use the lens galaxies with redshifts to explicitly remove scales below several h^{-1} Mpc, immunizing ourselves from this effect to a large degree. This is yet another reason that the approach we advocate here can be a powerful alternative to the shear–shear correlation functions which have been the focus of most weak lensing cosmological analyses to date.

Alternative approaches involving halo occupation distribution (HOD) modelling have also been considered (Yoo et al. 2006; Cacciato et al. 2009, 2013; Leauthaud et al. 2011, 2012; Tinker et al. 2012; van den Bosch et al. 2013) as ways to combine the galaxy–galaxy lensing and clustering observations to constrain cosmology. Those approaches can potentially give smaller statistical errors, since they use the small-scale lensing signals which typically have the best signal-to-noise ratio (S/N), but they are subject to additional systematic uncertainties both in terms of theory interpretation and observational uncertainties that are more pronounced on small scales (e.g. intrinsic alignments, magnification, data processing challenges near bright lens galaxies).

To be more quantitative, our approach is that the small-scale galaxy autocorrelation contains no cosmological information, since there is nothing in the distribution of galaxies within the halo that has a simple relation to cosmological parameters. While small-scale galaxy clustering can constrain HOD models, this by itself does not help in cosmological constraints. Moreover, it is potentially dangerous to rely on small-scale clustering to constrain cosmological models, because one can never be sure that the HOD parametrization is sufficiently general and that there is no artificial breaking of degeneracies with cosmological parameters due to insufficient generality. HOD models explored to date do not allow a reasonable degree of freedom in how galaxies are placed inside the haloes. For example, More et al. (2013) assume that the distribution of galaxies follows that of the dark matter, with just a 10 per cent uncertainty in the concentration–mass relation. Likewise, the 10-parameter HOD in Leauthaud et al. (2011) includes no freedom in the radial distribution of satellite galaxies, which is assumed to follow that of the dark matter. To date, no work has shown that either (a) cosmological information can be derived in a way that is completely unbiased with respect to these strong assumptions about the radial distribution of satellite galaxies, or (b) when one allows the radial distribution of satellites within haloes to be free, then one still gets any significant cosmological information from small-scale clustering.

Moreover, these HOD models ignore issues such as assembly bias (explicit dependence of clustering properties on assembly history, rather than just mass alone; Gao, Springel & White 2005, Gao & White 2007) that can change the relation between small- and large-scale clustering information. Once we are trying to place cosmological constraints at the ~ 5 per cent level, where these small details (such as the radial distribution of satellites within haloes and assembly bias) become more important, it is more robust simply to remove the small-scale clustering regime. Our approach explicitly does that.

When testing our procedure, we will apply it to a simulated mock sample, which we have generated using an HOD model known to reproduce the galaxy two-point correlation function, but our claim

is that our procedure should work on any sample. The reason for this claim is that despite using an HOD-based sample for the tests, the method itself does not assume a lack of assembly bias – in other words, the large-scale bias is not presumed to relate to the mean halo mass from the lensing measurement. Indeed, we could carry out this analysis on a sample with a significant assembly bias, but that assembly bias would not violate our much weaker assumption, which is that the same large-scale bias describes the weak lensing (via ξ_{gm}) and clustering (via ξ_{mm}). On large enough scales, this assumption must be true. One might worry that an assembly bias could change the trends in r_{cc} with scale. We see no reason a priori for this to be the case, but we caution that our method has not been tested with samples that were explicitly selected to include various levels of assembly bias, which we defer to future work.

While we believe that the galaxy autocorrelation contains no useful information on small scales, the galaxy–dark matter correlation does contain information on halo mass, which in combination with the galaxy autocorrelation on large scales can provide independent cosmological information using the method of Seljak et al. (2005). Our current method cannot take advantage of this additional information from the small-scale lensing, so in this sense it is suboptimal. But, again, using that small-scale lensing information would make us more obviously susceptible to errors due to assembly bias.

One additional aspect to our approach that is meant to reduce systematic uncertainties is that we do not simply use all of our lens galaxies in one large sample to get a small statistical error. Instead, we have several lens samples at different redshifts. This way, we can check for consistency of the results with each sample, and check for deviations from our assumptions about r_{cc} or observational systematics that scale with redshift (such as our understanding of the source redshift distribution, which is more important when the lens redshift approaches the typical source redshifts).

2.1 Simulations

While we argued in the previous section that our approach is, by design, fairly insensitive to the details of how galaxies occupy dark matter haloes, it is nevertheless useful to test the whole procedure on a mock data sample that is as close as possible to the real data. Here, we repeat the description of the N -body simulations that were used for validation of the method in Baldauf et al. (2010) and that we use for additional tests in this paper. We use the Zürich horizon ‘zHORIZON’ simulations, a suite of forty pure dissipationless dark matter simulations of the Λ CDM cosmology (Smith 2009). Each simulation models the dark matter density field in a box of length $L = 1500 h^{-1}$ Mpc, using $N_{\text{p}} = 750^3$ dark matter particles with a mass of $M_{\text{p}} = 5.55 \times 10^{11} h^{-1} M_{\odot}$. The cosmological parameters for the simulations in Table 1 are inspired by the results of the *Wilkinson Microwave Anisotropy Probe* (WMAP) CMB experiment (Spergel et al. 2003, 2007). The initial conditions were set up at redshift $z = 50$ using the 2LPT code (Scoccimarro

1998). The evolution of the N_{p} equal-mass particles under gravity was then followed using the publicly available N -body code GADGET-2 (Springel 2005). Finally, gravitationally bound structures were identified in each simulation snapshot using a Friends-of-Friends (FoF; Davis et al. 1985) algorithm with linking length of 0.2 times the mean interparticle spacing. We rejected haloes containing fewer than 20 particles, and identified the potential minimum of the particle distribution associated with the halo as the halo centre. In total, we identified haloes in the mass range $1.1 \times 10^{13} \leq M_{\text{vir}} \leq 4 \times 10^{15} h^{-1} M_{\odot}$.

We populate the haloes in these simulations with galaxies using the HOD. This model requires us to specify probability distributions for (a) the number of galaxies in our sample that occupy a halo of mass³ M , and (b) the radial distribution of galaxies within haloes. The HOD can be separated into terms representing ‘central’ galaxies living at the centre of haloes, and ‘satellite’ galaxies that are distributed more widely within the haloes.⁴ We assume that a halo can only contain a satellite if it also has a central galaxy. This assumption may not be entirely valid for a colour-selected sample such as LRGs, if the central galaxy is very bright but slightly too blue to be included in the sample. This will have effects on scales below the virial radius: the galaxy–dark matter correlations will be reduced on very small scales. It will also reduce galaxy clustering in cases when this satellite has another satellite in the same halo. We expect these effects to become small on scales larger than the virial radius.

Details of the five-parameter HOD that we used, and tests of how well it describes the sample abundance, lensing and clustering statistics, are given in Baldauf et al. (2010) and Reyes et al. (2010). The satellite fractions range from 10 per cent at the lower luminosity end to ~ 5 per cent at higher luminosity. These results are consistent with previous estimates of LRG environments (e.g. Reid & Spergel 2009).

2.2 Non-linear bias model

The analysis in Baldauf et al. (2010) was focused on modelling the cross-correlation coefficient r_{cc} , since this is the only quantity that is needed to relate the measurement of galaxy autocorrelation and galaxy–dark matter correlation to the dark matter autocorrelation. However, it is useful to analyse how well we model clustering and g–g lensing data separately with a given non-linear bias model. One reason to do so is that this allows us to choose different minimum scales (R_0) for galaxy–galaxy lensing and galaxy clustering. We expect that lensing information will be quite insensitive to the details of HOD modelling: both a satellite and a central galaxy give approximately the same g–g lensing signal for separations larger than the virial radius. So, we would expect the lensing signal to be fairly model independent down to the virial radius. In contrast, the clustering signal will depend very sensitively on how satellite galaxies are populated within the virial radius, so the clustering signal up to at least twice the virial radius will be quite model dependent. For example, if there are no satellites, then the clustering signal drops to almost zero within twice the virial radius, while if all the haloes have one central galaxy and one satellite radially distributed as the

Table 1. Cosmological parameters adopted for the simulations: matter density relative to the critical density, dark energy density parameter, dimensionless Hubble parameter, matter power spectrum normalization, primordial power spectrum slope and dark energy equation of state $p = w_{\text{de}}\rho$.

Ω_{m}	Ω_{Λ}	h	σ_8	n_{s}	w_{de}
0.25	0.75	0.7	0.8	1.0	−1

³ In principle, the number of satellite galaxies could depend on other parameters such as formation time; however, the HOD does not include dependence on anything other than mass.

⁴ Due to limited resolution, we do not attempt to place the satellites in subhalos, but rather distribute them probabilistically within the host halo.

dark matter, then the clustering signal is similar to the lensing signal. This sensitivity to how satellite galaxies populate haloes suggests that we should choose a larger value of R_0 for clustering than for lensing measurements. A second reason to use larger R_0 for clustering is that the statistical errors are significantly smaller than for lensing, so the analysis of clustering data is much more sensitive to inaccuracies in the theoretical model. A third reason is that if we can model both of these functions with a few free parameters, we can use the better-measured galaxy clustering data to determine these parameters.

To do so, we require models not just for r_{cc} , but also for scale-dependent bias, that are as realistic as possible. In order to interpret the measurements without taking ratios of noisy quantities, we must have some well-motivated way of describing the non-linear bias of the samples that we study. We consider the same local bias model of Fry & Gaztanaga (1993) as in Baldauf et al. (2010), $\delta_h = b\delta_m + (b_2/2)\delta_m^2 + (b_3/3!)\delta_m^3$, which contains a local bias relation between galaxy and dark matter density up to third order and combines it with standard perturbation theory (SPT), which expands the density perturbation into a series $\delta_m = \delta_m^{(1)} + \delta_m^{(2)} + \dots$, where $\delta_m^{(1)}$ is the Gaussian linear theory prediction and $\delta_m^{(n)}$ is of the order of $[\delta_m^{(1)}]^n$, to calculate the next-to-leading order corrections to the galaxy–galaxy and galaxy–matter power spectra. The third-order bias enters only through a renormalization of the leading order bias parameter, and does not have an explicit influence on the observable correlators. At the next-to-leading order, the corrections to the galaxy–galaxy and galaxy–matter power spectra come from the autocorrelation of δ_m^2 and its cross-correlation with the second-order density perturbation $\delta_m^{(2)}$. In evaluating these terms, we can define (Smith, Hernández-Monteagudo & Seljak 2009)

$$A(k) = \int \frac{d^3q}{(2\pi)^3} F_2(\mathbf{q}, \mathbf{k} - \mathbf{q}) P(q) P(|\mathbf{k} - \mathbf{q}|) \quad (14)$$

$$B(k) = \int \frac{d^3q}{(2\pi)^3} P(q) P(|\mathbf{k} - \mathbf{q}|), \quad (15)$$

where F_2 is the SPT mode coupling kernel (see, e.g. Bernardeau et al. 2002)

$$F_2(\mathbf{q}_1, \mathbf{q}_2) = \frac{5}{7}\alpha(\mathbf{q}_1, \mathbf{q}_2) + \frac{2}{7}\beta(\mathbf{q}_1, \mathbf{q}_2), \quad (16)$$

with

$$\alpha(\mathbf{q}_1, \mathbf{q}_2) = \frac{(\mathbf{q}_1 + \mathbf{q}_2) \cdot \mathbf{q}_1}{q_1^2},$$

$$\beta(\mathbf{q}_1, \mathbf{q}_2) = \frac{1}{2} (\mathbf{q}_1 + \mathbf{q}_2)^2 \frac{\mathbf{q}_1 \cdot \mathbf{q}_2}{q_1^2 q_2^2}. \quad (17)$$

Upon Fourier-transforming, we obtain the corresponding correlation functions, which are given by

$$\xi_{gg}(r, z) = b^2 \xi_{mm, NL}(r, z) + 2b b_2 \xi_A(r, z) + \frac{1}{2} b_2^2 \xi_B(r, z) \quad (18)$$

and

$$\xi_{gm}(r, z) = b \xi_{mm, NL}(r, z) + b_2 \xi_A(r, z). \quad (19)$$

$\xi_A(r)$ and $\xi_B(r)$ are the Fourier transforms of $A(k)$ and $B(k)$. In principle, $\xi_{mm, NL}$ should be the correlation function corresponding to one loop perturbation theory. Taking SPT at face value, the Fourier transform is ill behaved and we replace it by the non-linear correlation function measured in the N -body simulations. Note that $\xi_B = \xi_{lin}^2$.

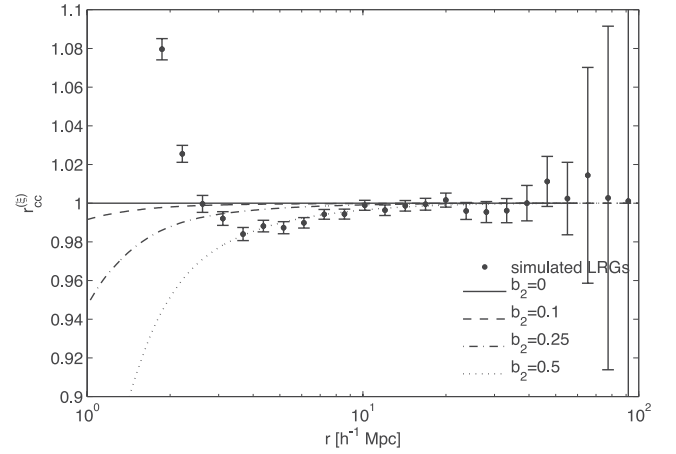


Figure 1. Correlation function cross-correlation coefficient between mock LRGs and dark matter (data points) in the simulations described in Section 2.1, with errors determined from the box to box variations in simulations. Lines represent predictions from our model, with $r_{cc}^{(\xi)} = 1 - (1/4)(b_2/b)^2 \xi_{lin}(r)$, using a large-scale bias of $b = 2.07$ (selected to match the observed large-scale ξ_{gg} and ξ_{gm} in the mock LRG sample) and different values of b_2 , with $b_2 = 0.5$ providing the best fit to the simulated clustering and lensing observable quantities. The plot goes to larger r compared to the 2D values of R used in our analysis, because the measured observables at some R depend on the 3D correlation functions to larger r .

As shown in Baldauf et al. (2010), the above model can be used to predict the cross-correlation coefficient in the linear and weakly non-linear regime. It predicts r_{cc} to be unity on large scales and to drop below unity as one goes to smaller scales, with explicit functional form given by $r_{cc}^{(\xi)} = 1 - (1/4)(b_2/b)^2 \xi_{lin}(r)$. We know this model to be imperfect in the sense that other non-linear bias parameters at a quadratic and cubic level may be needed to properly model the data (Baldauf et al. 2012; Chan, Scoccimarro & Sheth 2012), but these higher order parameters may not be that different in terms of their effect on the scale dependence of the statistics we study here, so we group them into a single parameter b_2 for the purpose of this paper.

As seen in Fig. 1, this model (with parameters chosen to match mock LRG catalogues, and in particular, best-fitting $b = 2.07$ and $b_2 = 0.5$) describes the correlation coefficient down to $3 h^{-1}$ Mpc, below which physics from within the virial radius begins to affect the results. As argued above, we expect that these effects are more significant for the autocorrelation than for the cross-correlation. We must choose the minimum scale at which we can still adopt this model. Our method for doing so will be described in Section 2.4; it is based on carrying out our analysis on simulated data, and checking that we can recover the true cosmology in the simulations. Before we can do so, we next describe how we model the observable quantities in real and simulated data, Υ_{gg} and Υ_{gm} .

2.3 Modeling the observables

Our approach is to use equations (18) and (19) to model the two observables. The data are used to constrain linear b , quadratic bias b_2 and the dark matter power spectrum times the matter density, as in equation (11). This is the full, non-linear matter power spectrum, as shown in Baldauf et al. (2010). We will use Markov chain Monte Carlo (MCMC) methods, in which the data are compared to the

Table 2. Properties of the lens samples described in Section 3. For each sample, we show the redshift range, the mean redshifts, the effective redshift for the lensing as in equation (25) and the number density.

Sample name	N_{gal}	z range	$\langle z \rangle$	$z_{\text{eff, gm}}$	\bar{n} [$(h \text{ Mpc}^{-1})^3$]
Main-L5	69 150	$0.02 \leq z < 0.155$	0.115	0.109	10^{-3}
LRG	62 081	$0.16 \leq z < 0.36$	0.278	0.257	10^{-4}
LRG-highz	35 088	$0.36 \leq z < 0.47$	0.407	0.398	$[8 - 6((z - 0.36)/0.11)] \times 10^{-5}$

model, hence for each set of cosmological parameters we must compute the fully non-linear dark matter power spectrum.

2.3.1 Matter power spectrum

We obtain the estimated linear $\xi_{\text{mm}}(r)$ by specifying the cosmological parameters using the `CAMB` linear gravity solver (Lewis, Challinor & Lasenby 2000), which is part of the `COSMOMC` package that we use for the estimation of the cosmological parameters (Lewis & Bridle 2002). We increase the accuracy of the solver, by setting `accuracy_level=1.5`, and checked that increasing `accuracy_level` does not change our results. The correlation functions $\xi_{\text{mm}}(r)$ are calculated at the effective redshifts of the three galaxy samples, given in Table 2.

To obtain a precise prediction for the non-linear matter power spectrum as a function of cosmological parameters, we are unable to use a standardized and publicly available emulator such as the one presented by Lawrence et al. (2010) for two reasons. First, we wish to explore variations of the Hubble parameter, H_0 , which cannot be independently varied using that emulator. Secondly, the emulator only provides predictions for the power spectrum to a maximum wavenumber of $k = 1 h \text{ Mpc}^{-1}$, but power at higher k is important when computing the matter power spectrum at our minimum scale of $R = 2 h^{-1} \text{ Mpc}$ to the required precision.

Thus, given the need to compute the non-linear power spectrum for arbitrary cosmological parameters θ that differ from our fiducial ones (θ_0), there are several possible approaches that we could take (given our simulations that are on a grid of cosmological parameters). The change in cosmological parameters affects the non-linear power spectrum in two ways: first, via the change in the linear power spectrum; and secondly, via the change in non-linearity corrections. Since the first effect is dominant, we account for it accurately using analytic calculations of the linear matter power spectrum, only interpolating on our simulation grid to account for the second (much smaller) effect. If we relate the non-linear and linear correlation functions via

$$\xi_{\text{nl}}(r|\theta) = \xi_{\text{lin}}(r|\theta) \frac{\xi_{\text{nl}}(r|\theta)}{\xi_{\text{lin}}(r|\theta)} \equiv \xi_{\text{lin}}(r|\theta) \alpha(r|\theta), \quad (20)$$

then we can Taylor-expand $\alpha(r)$ around our fiducial cosmological parameters,

$$\begin{aligned} \xi_{\text{nl}}(r|\theta) &= \xi_{\text{lin}}(r|\theta) \left[\alpha(r|\theta_0) + \sum_i \left. \frac{\partial \alpha(r|\theta)}{\partial \theta_i} \right|_{\theta_0} \Delta \theta_i \right] \\ &= \xi_{\text{lin}}(r|\theta) \alpha(r|\theta_0) \left[1 + \sum_i \left. \frac{\partial \log \alpha(r|\theta)}{\partial \theta_i} \right|_{\theta_0} \Delta \theta_i \right], \quad (21) \end{aligned}$$

where the index i runs over the parameters for which we have ξ_{mm} on a grid (σ_8 , n_s , Ω_m , H_0 and redshift z). As an example of how this works for one parameter, changing σ_8 mostly changes the amplitude of the correlation functions by the square of the ratio of two values of

σ_8 under consideration and this change is propagated exactly. Only the second-order change in the shape of the non-linear corrections is Taylor-expanded.

Our fiducial model has $\Omega_m = 0.25$, $\sigma_8 = 0.8$, $n_s = 1.0$, $h = 0.7$ and $z = 0.23$; we have eight simulations of this cosmology. To obtain the derivatives of non-linear corrections with respect to cosmological parameters (needed in equation 21), we use further models with $\Omega_m = (0.2, 0.3)$, $\sigma_8 = (0.7, 0.9)$, $n_s = (0.95, 1.05)$, $H_0 = (65, 75) \text{ km s}^{-1} \text{ Mpc}^{-1}$ and seven different redshift slices between $z = 0$ and $z = 0.51$. Non-linear correlation functions for these models are obtained from N -body simulations (Smith 2009). For each non-fiducial model, all parameters but one are kept at the fiducial value. For the parameters for which we have two simulations bracketing the fiducial value (Ω_m , σ_8 , z , H_0), we use different derivatives depending on whether the corresponding value for the target model is above or below the fiducial value. We opted to do this rather than calculating the second derivative to avoid numerical errors blowing up when the quadratic term becomes dominant. By construction, such modelling exactly reproduces the non-linear matter correlation function for models for which we have simulations.

2.3.2 Massive neutrinos

We would also like to place constraints on massive neutrinos, which requires some additional corrections to the formalism in Section 2.3.1. We parametrize the neutrino mass effect as the sum of masses for the three neutrino families, $\sum m_\nu$, and include three different ways that they affect the matter power spectrum. First, lensing is sensitive to the total gravitational potential, which includes a contribution from massive neutrinos. This requires us to use the Poisson equation to relate potential to density perturbations, the latter of which must include the neutrino contribution ($\delta\rho = \rho_{\text{cdm}}\delta_{\text{cdm}} + \rho_b\delta_b + \rho_\nu\delta_\nu$, where cdm, b and ν subscripts denote cold dark matter, baryons and neutrinos, respectively). For $\sum m_\nu = 0.15 \text{ eV}$, $f_\nu = \rho_\nu/(\rho_{\text{cdm}} + \rho_b) = 0.6$ per cent, and since neutrino perturbations go from $\delta_\nu = \delta_{\text{cdm}}$ on large scales to $\delta_\nu = 0$ on small scales, this effect suppresses the weak lensing power spectrum on small scales by 1.2 per cent.

The second effect is the usual suppression of matter fluctuations due to the fact that neutrino fluctuations are suppressed on small scales, which in turn leads to a suppressed growth of CDM and baryon fluctuations. For $\sum m_\nu = 0.15 \text{ eV}$, this effect leads to a 8 per cent suppression of the matter power spectrum. The two effects combined thus lead to 9.2 per cent suppression.

The third effect is the non-linear evolution correction, which further enhances this effect. For $k < 0.1 h \text{ Mpc}^{-1}$, the effect of neutrinos on the matter power spectrum in the linear regime can be described as a reduction of the amplitude and a red tilt (Bird, Viel & Haehnelt 2012). For $\sum m_\nu = 0.15 \text{ eV}$, this is a 4 per cent reduction in σ_8 and -0.01 reduction in n_s . Most of the mode coupling responsible for the non-linear effects comes from the long-wavelength modes with

$k < 0.1 h \text{ Mpc}^{-1}$, so it is reasonable to assume that the non-linear effects can be described with a change of amplitude and slope, scaling linearly with $\sum m_\nu$,

$$n_{s,\text{eff}} = n_s - 0.01 \frac{\sum m_\nu}{0.15 \text{ eV}}. \quad (22)$$

The change of amplitude, $\sigma_{8,\text{eff}} = \sigma_8 - 0.04[\sum m_\nu/(0.15 \text{ eV})]$, is already automatically included since we compute σ_8 for a given cosmological model using its power spectrum. The spectral index seen by the non-linear correction is not the actual one, but the effective one given by the above equation. This is justified by noting that the most important quantities that determine the shape of the non-linear correction are the amplitude and slope of the power spectrum at a relevant pivot scale ($k \sim 0.1 h \text{ Mpc}^{-1}$ in our case). Since the change in amplitude is already included in the change of σ_8 , we just approximate the change in the slope of the linear power spectrum at the pivot point for m_ν as the change in the spectral index.

To test this procedure, we compare the resulting non-linear to linear power spectrum correction for massive neutrinos to the full simulations presented in Bird et al. (2012). For example, for the total neutrino mass of $\sum m_\nu = 0.15 \text{ eV}$, we find that the reduced linear amplitude of the power spectrum at the pivot point is 8 per cent, corresponding to a 4 per cent change in σ_8 . This leads to a further non-linear suppression of power, up to 3 per cent at $k \sim 1 h \text{ Mpc}^{-1}$. In addition, the effective slope is reduced by 0.01 at the pivot point. This means that for massive neutrinos there is more power on large scales than in the zero-mass case, relative to the pivot point. As a result, there is more mode–mode coupling which increases the small-scale non-linear power, countering the effect from the reduced linear amplitude. The net effect is that the non-linear correction peaks at $k \sim 1 h \text{ Mpc}^{-1}$, but this quickly reverses sign above $2 h \text{ Mpc}^{-1}$. The overall effect is in good agreement with the results of the full simulations of massive neutrinos in Bird et al. (2012). This suggests that we can parametrize the non-linear effect of massive neutrinos simply with the change in the effective amplitude and slope of the linear power spectrum.

To summarize the neutrino mass effects at $k \sim 0.5 h \text{ Mpc}^{-1}$, which is the peak of the contribution to Υ at $R = 5 h^{-1} \text{ Mpc}$ and $R_0 = 3 h^{-1} \text{ Mpc}$ (fig. 2 of Baldauf et al. 2010) and where we expect to have the most stringent constraints from our data set, we expect about 10 per cent suppression of the power for $\sum m_\nu = 0.15 \text{ eV}$, relative to the zero-mass case.

2.3.3 Cosmology corrections

When estimating the signal from the data, we assume a cosmological model in order to convert angular distances $\Delta\theta$, shears γ_t and redshift-space separations Δz to transverse separation R , lensing surface density contrast $\Delta\Sigma$ and line-of-sight separation Π . Thus, for the model predictions for any other cosmology than the fiducial cosmology, we should in principle include a factor in both the transverse separation and the amplitude of the measured signals to account for the fact that the wrong cosmology was used to do these conversions from observed to physical separations. However, for the highest redshift sample (for which this is most important), the size of the corrections is typically $\lesssim 1$ per cent for the range of allowed cosmological models. The correction is even smaller for the other samples; therefore, it is well within the statistical error for this analysis, and we do not include it.

2.3.4 Combining the model ingredients

Finally, we need to combine these model ingredients to obtain $\xi_{\text{gm}}(r)$ and $\xi_{\text{gg}}(r)$. We do so by using the non-linear matter power spectrum for a given cosmology from Section 2.3.1 along with equations (18) and (19).

The results are then integrated to obtain the projected statistics that we use in reality. For the lensing signals, we integrate the correlation function along the line of sight to $\pm 140 h^{-1} \text{ Mpc}$, consistent with the fact that the lensing window is extremely broad. We do not include that window directly, but as shown in Baldauf et al. (2010, fig. 9), its effects are very small on the scales we use for science, and can be corrected for in a single factor that includes the clustering line-of-sight integration length, redshift-space distortions (RSD) and the lensing window. Given that this correction factor is ~ 3 per cent at $60 h^{-1} \text{ Mpc}$, much smaller than the observational errors, and ~ 1 per cent below $30 h^{-1} \text{ Mpc}$, we neglect this correction.⁵ For clustering, we integrate along the line of sight to $\pm 60 h^{-1} \text{ Mpc}$, consistent with the observational measurements. Finally, for both the lensing and clustering we use the projected surface densities to obtain Υ .

Because we have some uncertainty in the calibration of the lensing signal due to several systematic errors (Section 4.2.1), we include a nuisance calibration bias parameter for the g–g lensing, which is assumed to have a mean zero and a Gaussian width of (4, 4 and 5) per cent for the three samples. The calibration bias is assumed to be the same at all radii and for all samples – i.e. if the calibration bias is 4 per cent for Main-L5, then it is 4 and 5 per cent for LRG and LRG-highz. This treatment is appropriate since the lensing calibration biases originate from the same sources for each sample, and improper estimation and removal of those biases would affect all samples nearly equally.

2.4 Choice of R_0

Baldauf et al. (2010) considered relatively large values of R_0 such as 3 and $5 h^{-1} \text{ Mpc}$. Use of a large value of R_0 is advantageous from the perspective of systematic error, because it means that we are less sensitive to several effects that tend to be worse at small scales: cross-correlation coefficient deviations from 1, deviations from our model for non-linear bias and observational issues such as intrinsic alignments.

However, use of larger R_0 will necessarily remove more of the measured signal, resulting in a noisier measurement. We therefore revisit the choice of R_0 in order to achieve a fair compromise between statistical and systematic error. Moreover, unlike in Baldauf et al. (2010), we permit different R_0 for the galaxy–galaxy lensing and the galaxy clustering, which is possible in the case that we explicitly model the signals (i.e. using different R_0 means that results cannot be obtained by taking ratios of the two signals). The galaxy clustering signal is more sensitive than the galaxy–galaxy lensing to the fidelity of the non-linear bias model (because it has higher S/N), so it might require a higher R_0 to avoid systematic errors.

We choose values of R_0 for the two measurements based on modelling the simulated LRG sample using the same machinery that we use to model the data (but without adding lensing shape noise, so that deviations from the real cosmology in the simulations are due

⁵ Technically, we have only done this test for the LRG sample. However, for the higher redshift and mass sample, the galaxy bias is higher and therefore RSD are even less important. For the lower redshift and mass sample, while the galaxy bias is lower and RSD are more important, we will see that the observational errors are also larger than for LRG.

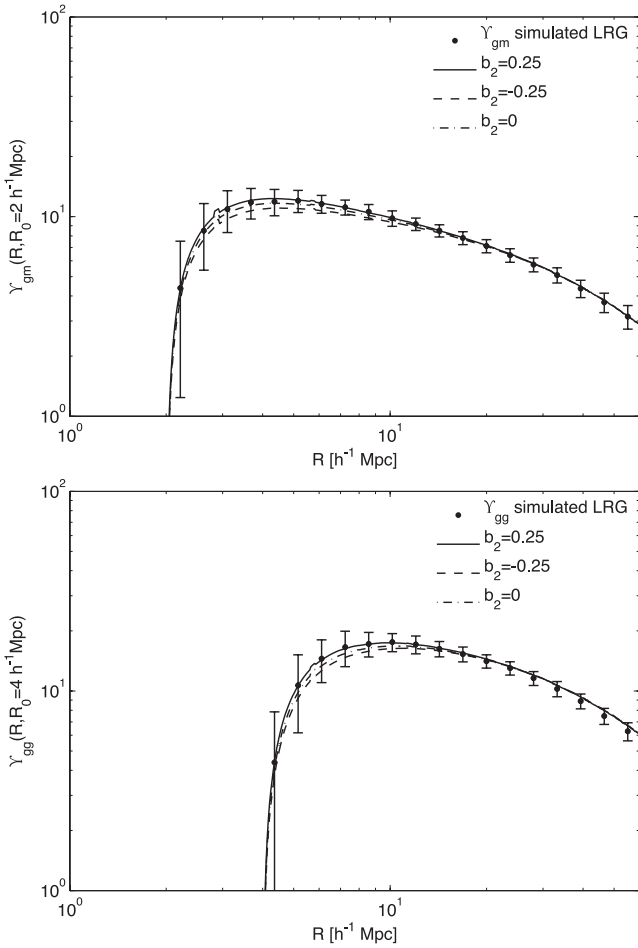


Figure 2. Top: Υ_{gm} for mock LRGs and the model predictions. Bottom: Υ_{gg} for mock LRGs and the model predictions.

to a real analysis bias). We decided to use $R_0 = 2$ and $4 h^{-1}$ Mpc for galaxy–galaxy lensing and galaxy clustering, respectively, since we find that this choice still gives a small systematic error compared to the statistical error, as shown in Appendix A. The corresponding plots of Υ are shown in Fig. 2, and we see that the simulated data and the best model agree reasonably well both for galaxy–galaxy lensing and galaxy clustering, with $b_2 = 0.25$ working acceptably. Note that $b_2 = 0.5$ best describes the cross-correlation coefficient for ξ , as seen in Fig. 1. In fact for the simulated data, values in the range from $b_2 = 0.25$ to 0.5 are able to describe the data within the limits of our error bars. A study carried out independently from this work (Cacciato et al. 2012) has also studied the value of R_0 for which we can safely achieve $r_{\text{cc}} \sim 1$ at all $R > R_0$, in the context of a more general HOD model. They identify $3 h^{-1}$ Mpc as a reasonable choice of R_0 (assuming the same R_0 is used for both measurements), nicely consistent with our findings.

2.5 Parameter values and constraints

Our convention is to quote parameter values based on the median of the posterior distribution after marginalization over all other parameters. Except where explicitly stated otherwise, we include a prior that is a function of σ_8 , based on our calibration on simulations in Appendix A. The quoted error bars come from using the probability distribution function (PDF) to determine the 68, 95 and 99.7 per cent confidence intervals.

3 DATA

Here, we describe the data used in this paper, all of which comes from the SDSS. The SDSS (York et al. 2000) imaged roughly π steradians of the sky, and followed up approximately one million of the detected objects spectroscopically (Eisenstein et al. 2001; Richards et al. 2002; Strauss et al. 2002). The imaging was carried out by drift-scanning the sky in photometric conditions (Hogg et al. 2001; Ivezić et al. 2004), in five bands (*ugriz*) (Fukugita et al. 1996; Smith et al. 2002) using a specially designed wide-field camera (Gunn et al. 1998). These imaging data were used to create the cluster and source catalogues that we use in this paper. All of the data were processed by completely automated pipelines that detect and measure photometric properties of objects, and astrometrically calibrate the data (Lupton et al. 2001; Pier et al. 2003; Tucker et al. 2006). The SDSS-I/II imaging surveys were completed with a seventh data release (DR7) (Abazajian et al. 2009), though this work will rely as well on an improved data reduction pipeline that was part of the eighth data release, from SDSS-III (Aihara et al. 2011), and an improved photometric calibration (‘ubercalibration’; Padmanabhan et al. 2008).

Below we describe the samples that are used as lenses and as sources.

3.1 Main sample lenses

The first lens sample that we use for this work is the flux-limited Main galaxy sample (Strauss et al. 2002) from SDSS DR7. The nominal flux limit is $r < 17.77$, when defined using Petrosian magnitudes⁶ (based on a modification of Petrosian 1976 described in Blanton et al. 2001 and Yasuda et al. 2001). In reality, the actual flux limit varies slightly across the survey area. We use the Main sample selection from the New York University (NYU) Value-Added Galaxy Catalog (VAGC, Blanton et al. 2005), which includes 7966 deg^2 of spectroscopic coverage (though we will employ further area cuts, described below).

We select our sample using the ‘Large-Scale Structure (LSS) sample’ DR7-2 in the VAGC, which carefully tracks the spectroscopic flux limit and completeness across the sky. The particular LSS samples that we use are ‘dr72full8’ through ‘dr72full10’, where ‘full’ samples have the following properties:

- (i) they use all galaxies from $r > 10$ to the position-dependent flux limit;
- (ii) they use areas with any level of completeness (even < 0.5 , which occurs very rarely) and
- (iii) Galaxies that did not get a spectrum due to fibre collisions are assigned a redshift using the nearest-neighbour method.

The ‘8’, ‘9’ and ‘10’ subsamples have the following properties, some of which will be subject to more cuts described below:

- (i) Redshift $0.001 < z < 0.4$.
- (ii) The k -corrections are to $z = 0.1$ (KCORRECT v4_1_4; Blanton & Roweis 2007).
- (iii) The distance modulus $\mu = 5 \log [D_L / (10 \text{ pc})]$ is determined using $\Omega_m = 0.3$, $\Omega_\Lambda = 0.7$. This is formally inconsistent with the numbers used in the rest of this paper. However, this is not a significant issue here where we simply seek a reasonably volume-limited

⁶ All magnitudes quoted in this paper are corrected for Galactic extinction using the dust maps from Schlegel, Finkbeiner & Davis (1998) and the extinction-to-reddening ratios from Stoughton et al. (2002).

and consistent sample (particularly given the weak dependence of the distance modulus on cosmology for these redshifts).

(iv) The luminosity evolution is assumed to have the form

$$M(z) = M(z = 0.1) - 2[1 - (z - 0.1)](z - 0.1), \quad (23)$$

which is chosen to match the number counts of SDSS spectroscopic galaxies.⁷ Given the redshift limits of our sample, this correction is constrained to lie within the range $[-0.17, 0.10]$.

(v) The absolute magnitude is defined, in terms of the Petrosian magnitude r and galaxy redshift z , correcting for luminosity evolution, as

$$M_r = r - [\mu + k_{0.1}(z) + M(z) - M(z = 0.1)]. \quad (24)$$

Given that the luminosity evolution is such that galaxies were brighter in the past, the definition here removes that trend, connecting galaxies at one redshift to those that were suitably brighter at earlier times according to the empirically determined evolution law in equation (23).

(vi) The absolute magnitude is then required to be in the range $[-22, -21]$, $[-21, -20]$ and $[-20, -19]$ for the three samples, respectively.

The effective area of the LSS sample is 7279 deg^2 . We then imposed some additional cuts on the area, removing regions without any source galaxies in the background or within a Tycho bright star map (Høg et al. 2000). These cuts reduce the effective area to 7131 deg^2 .

We wish to avoid overlap with the LRG lens samples described in the upcoming subsection, so that the cross-covariance between the signals with different lens samples can be assumed to be zero. Thus, we first require $0.02 < z < 0.155$ (where the lower redshift cut removes galaxies for which it would be computationally prohibitive to measure correlations to $70 h^{-1} \text{ Mpc}$, and the upper redshift cut removes overlaps with LRGs). We then defined the three LSS samples using the notation from Mandelbaum et al. (2006a): L3 with $-19 > M_r \geq -20$, L4 with $-20 > M_r \geq -21$, L5 with $-21 > M_r \geq -22$. We do not define any brighter samples because their low abundance means that there are very few galaxies in those samples after the $z < 0.155$ cut.

In practice, carrying out the analysis with all three samples requires caution: if the redshift ranges overlap (as naturally occurs for a flux-limited sample), then for scales above $R \sim 8 h^{-1} \text{ Mpc}$, we find that the clustering and lensing signals exhibit high cross-correlations between the samples – typically 80 per cent – because they trace similar large-scale structures. When limiting to volume-limited samples that do not overlap, the statistical power of L3 and L4 becomes relatively low on cosmological scales. In addition, our non-linear bias model in Section 2 was only tested on simulations with relatively high-mass haloes ($M_{\text{vir}} \gtrsim 1 \times 10^{13} h^{-1} M_{\odot}$). Given the typical halo masses for L3 and L4 in Mandelbaum et al. (2006a), we conclude that the optimal way of including the Main sample in this analysis is to use L5 only. This sample (referred to as ‘Main-L5’ in the rest of the paper) includes 69 150 galaxies, and is volume limited for the redshift range that we use.

For computation of cosmological observables, we require a set of random points that are distributed in the same way as the lens sample. We therefore use the sets of random points distributed for this sample in the VAGC LSS sample; this includes a proper redshift distribution that depends on the position-dependent flux limit at each

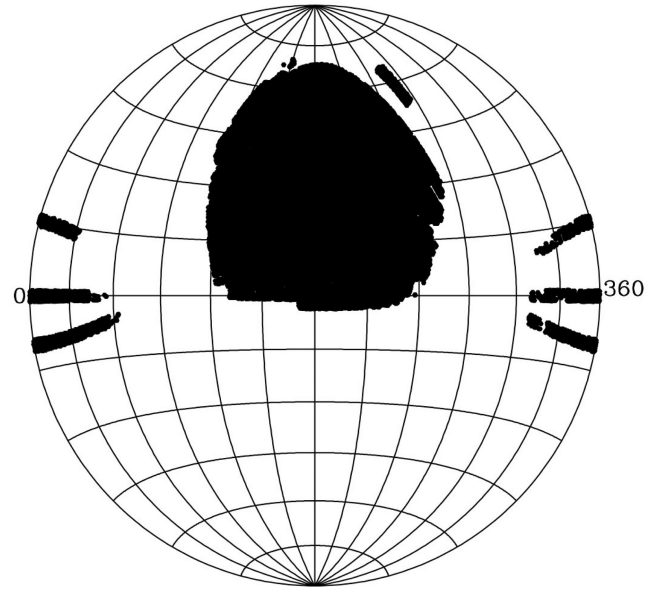


Figure 3. Area coverage of the lens samples used in this paper.

point. For weighting, we use the inverse of the ‘sector completeness’ defining the redshift success rate. The sector completeness for this sample has a median value of 0.972; 95 per cent of the galaxies have completeness above 0.924.

The area coverage of the lens sample (7131 deg^2 , or $f_{\text{sky}} = 0.17$) is shown in Fig. 3. This coverage is strictly a subsample of the source catalogue from Reyes et al. (2012) that we describe in Section 3.3.

The redshift distribution dp/dz and the comoving number density \bar{n} are shown for the Main-L5 sample, and for the other samples described in subsequent subsections, in Fig. 4. For the Main-L5 sample, the comoving number density is $\sim 10^{-3} (h \text{ Mpc}^{-1})^3$.

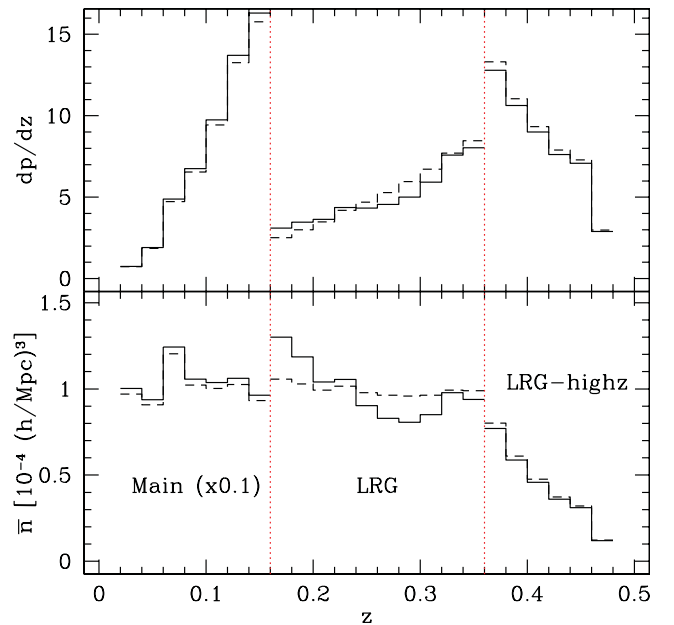


Figure 4. Top: redshift distribution dp/dz for the three lens samples used in this work, as labelled on the plot. The solid and dashed lines show the unweighted and weighted histograms, respectively. Bottom: comoving number density \bar{n} , in units of $10^{-4} (h \text{ Mpc}^{-1})^3$ (multiplied by 0.1 for Main-L5 for easier viewing). The dotted vertical lines show the delineation between the different lens samples.

⁷ <http://sdss.physics.nyu.edu/vagc/lss.html>

The properties of this sample (and those introduced in subsequent sections) are summarized in Table 2. For the lensing, the effective redshift $z_{\text{eff, gm}}$ is determined not just by the lens redshift distribution, but also by geometric factors related to the relation between lens and source redshifts that come into the weighting scheme we use for estimating the signals (Section 4):

$$z_{\text{eff, gm}} = \frac{\sum_{l_s} w_{l_s} z_{l_s}}{\sum_{l_s} w_{l_s}}. \quad (25)$$

3.2 LRG sample lenses

We also define two lens samples consisting of LRGs (Eisenstein et al. 2001). These galaxies have been used for numerous cosmology analyses with SDSS, most notably the detection of BAO, which is enabled by the high galaxy bias of ~ 2 and the large volume probed by this sample, $\sim 0.65 (h^{-1} \text{Gpc})^3$.

For selection of LRGs, we follow the methodology⁸ of Kazin et al. (2010), which also starts from the NYU VAGC LSS sample described in the previous subsection. In this case, only regions with completeness ≥ 0.6 are included; this definition is inconsistent with that used for Main-L5, but in practice, the discrepancy only affects 13 deg², or 0.2 per cent of the area. Our selection is otherwise identical to that from Kazin et al. (2010), with the exception of area cuts to restrict to the footprint of the source catalogue, eliminating 8 per cent of the LRGs.

Rest-frame absolute magnitudes in the g band are calculated starting from the r -band extinction-corrected apparent Petrosian magnitude. The distance modulus assumes $\Omega_m = 0.25$, $\Omega_\Lambda = 0.75$. k -corrections and evolution corrections from Eisenstein et al. (2001) are used to convert r to M_g .

Kazin et al. (2010) have a well-defined procedure for calculating weights, completeness factors, dealing with fibre collisions, and distributing random points. In brief, they begin with a calculation of sector completeness to account for all sources of incompleteness except for fibre collisions (i.e. this calculation accounts for galaxies *that were allocated fibres* and did not get a spectrum). This completeness is used when distributing random points in the survey area; in any given region, they are diluted according to that region's sector completeness. To deal with the ~ 2 per cent of LRG targets that were not allocated fibres due to fibre collisions, a special weight is assigned; e.g. in a group of three LRGs of which only two were allocated a fibre, those two would each get a weight of 1.5. The random points – of which there are 15 times as many as real points – are assigned a random redshift drawn from the $p(z)$ of the real LRGs.

We define two redshift samples, which we call ‘LRG’ ($0.16 \leq z < 0.36$) and ‘LRG-highz’ ($0.36 \leq z < 0.47$). In both cases, the absolute magnitude limits are $-23.2 < M_g < -21.2$; the former is approximately volume limited, whereas the latter is flux limited but relatively narrow⁹ (see Fig. 4). In the first case, we adopt a radial

weighting scheme that reduces the impact of large-scale structure fluctuations on the redshift histogram. This scheme is taken directly from Kazin et al. (2010, appendix A2), is optimized for BAO studies and does not significantly change the results, but we use it directly in order to enable a comparison between our results and other large-scale structure measurements with LRGs. In short, they bin the redshift histogram into bins of width $\Delta z = 0.015$, and define a smooth $n(z)$ by doing a spline fit to that histogram. Then, the radial weight is defined as $1/(1 + n(z)P_{\text{fid}})$ where $P_{\text{fid}} = 4 \times 10^4 (h \text{Mpc}^{-1})^3$. Thus, for the LRG sample, the weights used for real points are

$$w_{\text{LRG}} = \left[\frac{\text{fibre collision weight}}{\text{completeness}} \right] \left[\frac{1}{1 + n(z)P_{\text{fid}}} \right] \quad (26)$$

and for random points, the same but without any fibre collision weights.¹⁰ For the LRG-highz sample, we use

$$w_{\text{LRG-highz}} = \frac{\text{fibre collision weight}}{\text{completeness}}. \quad (27)$$

In this case, since the $n(z)$ is a stronger function of redshift, it is not clear that it makes sense to include it in the weighting, and particularly not in a lensing analysis where the source density is dropping rapidly with redshift.

Once we include the redshift-dependent weighting, the LRG sample has a comoving number density that is nearly constant at $10^{-4} (h \text{Mpc}^{-1})^3$, a factor of 10 smaller than for Main-L5. The LRG-highz sample has a comoving number density that drops with redshift because the sample is flux limited. More details of these samples are shown in Table 2.

3.3 Sources

The catalogue of source galaxies with measured shapes used in this paper is described in Reyes et al. (2012, hereafter R12), which uses the re-Gaussianization method (Hirata & Seljak 2003) of correcting for the effects of the point spread function (PSF) on the observed galaxy shapes. The treatment of systematic errors is updated and improved compared to the previous SDSS source catalogue using this PSF-correction method (Mandelbaum et al. 2005), in part using tests of simulated SDSS images using real galaxies from the Cosmological Evolution Survey (COSMOS) and real SDSS PSFs (Mandelbaum et al. 2012). To estimate source redshifts, we use photometric redshifts (photo- z) based on the five-band photometry from the Zurich Extragalactic Bayesian Redshift Analyzer (ZEBRA; Feldmann et al. 2006), which were characterized by Nakajima et al. (2012, hereafter N12). In particular, we use the maximum-likelihood mode for ZEBRA, and choose the best-fitting photo- z after marginalizing over the SED template.

The catalogue production procedure was described in detail in R12, so we describe it only briefly here. Galaxies were selected in a 9243 deg² region, with an average number density of 1.2 arcmin⁻².

and/or clustering signals have additional assumptions that *would* be violated at some level in a flux-limited sample, because the small- and large-scale lensing signals scale with $M^{2/3}$ and b , respectively, so the effective mean halo mass and bias inferred from small- and large-scale lensing signals would not in general lie on the cosmological halo mass versus bias relation.

¹⁰ When normalizing ratios of real versus random points, we use weights rather than absolute numbers of galaxies, and must watch out for the fact that if $N_{\text{real}} = N_{\text{rand}}$, $\sum w_{\text{real}} \neq \sum w_{\text{rand}}$, because of the fibre collision weighting on the real points.

⁸ <http://cosmo.nyu.edu/~eak306/SDSS-LRG.html>

⁹ One might legitimately wonder whether the method described in Section 2 can be applied to a flux-limited sample, in which the sample properties clearly evolve with redshift. However, as emphasized there, all we are assuming is that the large-scale bias describing the galaxy autocorrelation is the same as that describing the galaxy–mass cross-correlation, and the stochasticity is near 1 on the scales we use. Using the notation from Section 2, it is possible to show that our method should be broadly applicable for galaxy populations with mixes of properties, provided that the above assumptions are true. In contrast, methods that use the small-scale lensing

The selection was based on cuts on the imaging quality, data reduction quality, galactic extinction $A_r < 2$ defined using the dust maps from Schlegel et al. (1998) and the extinction-to-reddening ratios from Stoughton et al. (2002), apparent magnitude (extinction-corrected $r < 21.8$), photo- z and template used to estimate the photo- z , and galaxy size compared to the PSF. The apparent magnitude cut used model magnitudes,¹¹ which are defined by fitting the galaxy profile in the r band to a Sérsic profile with $n = 1$ (exponential) and $n = 4$ (de Vaucouleurs), choosing the better of the two models, and then using that same rescaled profile to get magnitudes in all the bands. For comparing the galaxy size to that of the PSF, we use the resolution factor R_2 which is defined using the trace of the moment matrix of the PSF T_P and of the observed (PSF-convolved) galaxy image T_1 as

$$R_2 = 1 - \frac{T_P}{T_1}. \quad (28)$$

We require $R_2 > 1/3$ in both r and i bands.

The software pipeline used to create this catalogue obtains galaxy images in the r and i filters from the SDSS ‘atlas images’ (Stoughton et al. 2002). The basic principle of shear measurement using these images is to fit a Gaussian profile with elliptical isophotes to the image, and define the components of the ellipticity

$$(e_+, e_\times) = \frac{1 - (b/a)^2}{1 + (b/a)^2} (\cos 2\phi, \sin 2\phi), \quad (29)$$

where b/a is the axis ratio and ϕ is the position angle of the major axis. The ellipticity is then an estimator for the shear,

$$(\gamma_+, \gamma_\times) = \frac{1}{2\mathcal{R}} ((e_+, e_\times)), \quad (30)$$

where $\mathcal{R} \approx 0.87$ is called the ‘shear responsivity’ and represents the response of the ellipticity (equation 29) to a small shear (Kaiser, Squires & Broadhurst 1995; Bernstein & Jarvis 2002); $\mathcal{R} = 1 - e_{\text{rms}}^2$. In the course of the re-Gaussianization PSF-correction method, corrections are applied to account for non-Gaussianity of both the PSF and the galaxy surface brightness profiles (Hirata & Seljak 2003).

For this work, we do not use the entire source catalogue, only the portion overlapping the aforementioned lens samples and around the edges. Fig. 5 shows histograms of the source galaxy r -band apparent magnitude and photo- z .

4 OBSERVATIONAL METHOD

In this section, we describe how we use the galaxy catalogues from Section 3 to measure our two observables, the galaxy–galaxy lensing and the galaxy clustering.

4.1 Galaxy–galaxy lensing

Here, we describe the computation of the lensing signal. For this computation, we rely on the lens catalogues in Sections 3.1 and 3.2, and the catalogues of random lenses with the corresponding area coverage and redshift distributions. First, pairs of lenses and sources that are physically close on the sky and satisfy $z_s > z_l$ (using photo- z for sources) are identified. Here, ‘physically close’ is determined using the comoving transverse separation at the lens redshift; we require $0.02 < R < 32.9 h^{-1}$ Mpc for Main-L5, and $0.02 < R <$

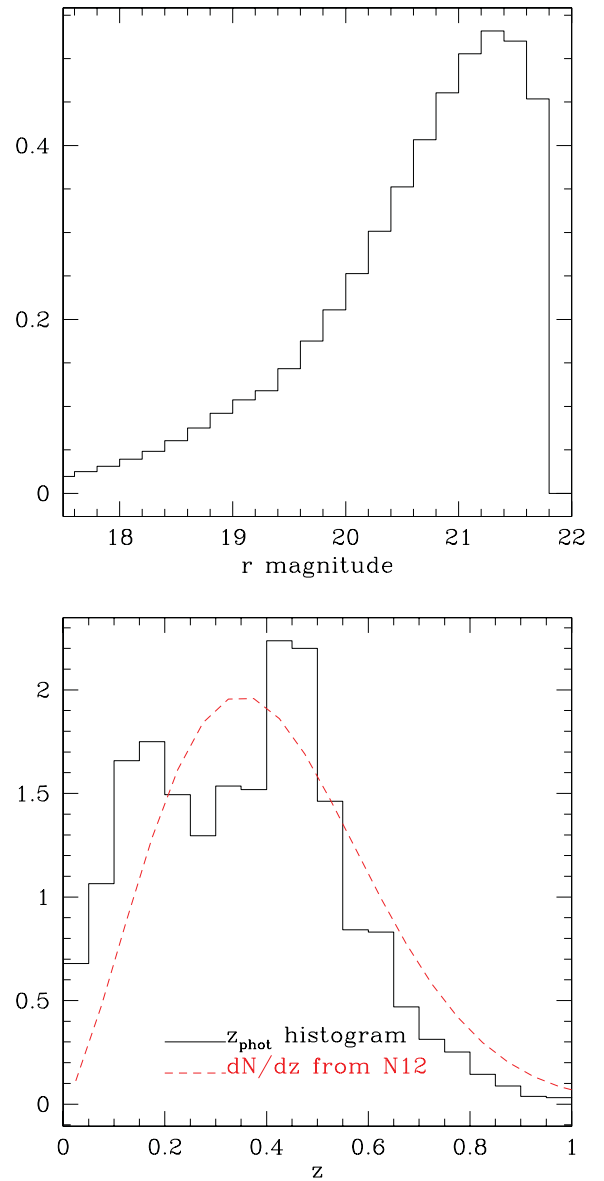


Figure 5. Histograms of source galaxy properties, derived from a random subsample of 5 per cent of the catalogue after imposing all cuts ($\sim 2 \times 10^6$ galaxies). Top: histogram of r -band extinction corrected model magnitude. Bottom: photo- z histogram, and the inferred true dN/dz from N12.

$73.1 h^{-1}$ Mpc for the two LRG samples. These ranges are split into 37 or 41 logarithmic radial bins with $\Delta(\ln R) = 0.2$.

Lens–source pairs are assigned weights according to the error on the source shape measurement via

$$w_{\text{ls}} = \frac{1}{\Sigma_c^2 (\sigma_s^2 + \sigma_{\text{SN}}^2)}, \quad (31)$$

where σ_s^2 is the estimated shape measurement error due to pixel noise (validated in R12 by comparing measured shapes in repeat observations), and σ_{SN}^2 , the intrinsic shape noise, was found in R12 to be 0.365, independent of magnitude. The factor of Σ_c^{-2} means that we weight by inverse variance of the expected lensing signal, thus downweighting pairs that are close in redshift because the lensing geometry is suboptimal.

¹¹ http://www.sdss3.org/dr8/algorithms/magnitudes.php#mag_model

Once we have computed these weights, the lensing signal in each annular bin can be computed via a summation over lens–source pairs ‘ls’ and random lens–source pairs ‘rs’:

$$\Delta\Sigma(R) = \frac{\sum_{\text{ls}} w_{\text{ls}} e_t^{(\text{ls})} \Sigma_{c,\text{ls}}}{2\mathcal{R} \sum_{\text{rs}} w_{\text{rs}}}, \quad (32)$$

where the factor of $2\mathcal{R}$ arises due to our definition of ellipticity and is needed to convert tangential ellipticity e_t to shear γ_t . Note that this is equivalent to the procedure in previous works such as Mandelbaum et al. (2005) of using $\sum_{\text{ls}} w_{\text{ls}}$ in the denominator and then multiplying the result by the boost factor,

$$B(R) = \frac{\sum w_{\text{ls}}}{\sum w_{\text{rs}}}. \quad (33)$$

The division by $\sum w_{\text{rs}}$ is necessary to account for the fact that some of our ‘sources’ are physically associated with the lens, and therefore not lensed by it.¹²

Due to the observational strategy in SDSS, there is a tendency for the PSF to align coherently along the scan direction. This tendency gives rise to a so-called systematic shear if the PSF correction is not perfectly efficient at removing the PSF ellipticity from the galaxy shapes, which turns out to be the case at a low level for our PSF-correction method. If a lens has a uniform distribution of sources around it, the contribution of the coherently aligned systematic shear to the average tangential shear is zero. Thus, the systematic shear can contribute to the lensing signal primarily due to the inclusion of lenses near survey boundaries, since they lack a symmetric distribution of sources. To remove this systematic shear, we can simply subtract the lensing signal $\Delta\Sigma_{\text{rand}}$ measured around random points, which will capture the geometry-dependent effect of the systematic shear. As noted by Mandelbaum et al. (2005), this correction may be imperfect in the case that the lens density fluctuates due to some effect that also modulates the systematic shear, if this modulation is not included in the random point distribution. We will return to this issue in Section B5.

To compute Υ using equation (12) on our noisy, binned data, we use the following procedure. We first determine $\Delta\Sigma(R_0)$; a discussion of how this procedure can affect results is in Mandelbaum et al. (2010). For this project, as we will show in Section B1, we are helped by the fact that around R_0 there is a range of scales on which $\Delta\Sigma(R)$ is well approximated by a power law. This situation is different from that of Mandelbaum et al. (2010), which used galaxy clusters with R_0 well within the cluster virial radius, so that the scaling of $\Delta\Sigma(R)$ was inconsistent with a power law. Thus, in this paper (unlike previous work) we can fit $\Delta\Sigma$ to a power law over a fixed range of scales, which will minimize the noise in estimation of $\Delta\Sigma(R_0)$ that gets propagated into Υ . We present details and tests of this procedure in Section B1. After estimating $\Delta\Sigma(R_0)$, we compute Υ in each radial bin using equation (12) directly.

For science, we only use scales above $2h^{-1}$ Mpc ($4h^{-1}$ Mpc) for the lensing (clustering), which results in the inclusion of 18 radial bins for LRGs and 14 for Main sample lenses (14 and 10). These bin counts take into account the fact that we exclude the nominal first radial bin above $4h^{-1}$ Mpc for the clustering, because while the bin centre is above R_0 , the lower edge is below R_0 , and we do not attempt to model Υ in this rapidly varying regime. The

maximum scales of ~ 30 and $\sim 70h^{-1}$ Mpc for Main-L5 and the LRG samples, respectively, were chosen based on considerations related to systematic error, which will be described in Appendix B5. In brief, our finding is that there seem to be fluctuations of lens number densities that correlate with systematic errors in the shear for larger scales and lead to a situation where our systematic uncertainty exceeds the statistical error on the signal.

To determine errors on the lensing signal $\Delta\Sigma$ or derived quantities like Υ , we divide the survey area into 100 equal-area¹³ jackknife subregions, each of size ~ 71 deg² or typical length-scale ~ 8.4 . The same division of the area into regions will be used when computing the galaxy clustering signal, so that we can also estimate the covariance between the two. This number of regions was motivated by a desire to balance two competing effects. First, we require that the number of regions be significantly larger than the number of radial bins (18), to reduce the noise in the covariance matrix (Hirata et al. 2004). Secondly, we require that the region size be larger than the maximum scale used for science. For the Main sample, $30h^{-1}$ Mpc (comoving) at $z = 0.11$ corresponds to 5.3 ; for LRGs, $70h^{-1}$ Mpc at $z = 0.27$ corresponds to 5.2 . Thus, our typical region size is 60 per cent larger than the maximum angular scale used for science.

When computing the covariance for derived quantities, such as Υ , we estimate Υ for each jackknife sample to get the covariance matrix, rather than using the covariance matrix for $\Delta\Sigma$ and propagating errors.

It is well known that jackknife covariance matrices cannot be used to get cosmological constraints without some correction due to the finite level of noise (e.g. Hirata et al. 2004; Hartlap, Simon & Schneider 2007); this is a consequence of the fact that the inverse of a noisy, unbiased estimator of the covariance matrix is *not* an unbiased estimator of the inverse covariance matrix. We handle this issue by modelling the covariance matrix to eliminate noise. (While this might seem to eliminate the need to make many jackknife regions to reduce noise, as we have already done, we still need the covariance matrix to be reasonably well determined in order to easily model it empirically.) Details of this approach will be described in Sections 5.2 and 6.2. However, we note that our results are insensitive to whether we use the noisy jackknife covariances with a correction factor (Hartlap et al. 2007) after inverting to obtain the inverse covariance, or whether we use the covariance matrices that we have modelled to reduce the noise. This finding suggests that our results are not significantly impacted by systematics related to our handling of covariance matrices.

4.2 Lensing systematic errors

A thorough treatment of systematic errors with this source catalogue is in R12. Here, we include only a brief summary of the issues, along with the impact for this work.

4.2.1 Calibration biases

In R12, we considered several different types of systematic errors for which we applied corrections and estimated a total error budget. In this work, we consider the same set of systematic errors, with the only change being that the lens samples are at different redshifts,

¹²This correction is formally correct in the limit that other effects that modulate the source number density, such as magnification or difficulty in detecting sources due to software or light from the lens, are negligible. This condition is satisfied on all scales used in this work.

¹³For an arbitrary survey geometry, it is difficult to achieve equal-area and contiguous regions. We have opted for equal-area regions, roughly 10 per cent of which are not contiguous.

thus changing the values of many of the systematic errors and their uncertainties.

To summarize briefly, our approach to estimating the systematic error budget is to consider a full list of systematic errors that affect the lensing signal calibration. We correct for our best estimate of any biases, and assign systematic errors using the following prescription: for those types of biases that are inherently connected, we assume that systematic uncertainties add linearly (e.g. two sources of 1 per cent-level uncertainty become a combined 2 per cent uncertainty); for those that are independent, we add them in quadrature (i.e. in the previous example, the combined uncertainty would be $\sqrt{2}$ per cent).

There are three calibration biases related to shear estimation that we consider to be inherently connected: errors in the correction for PSF dilution due to the PSF correction method not being perfect, noise rectification bias and selection biases (due to our resolution cut favouring galaxies that are aligned with the shear). In R12, we described tests using realistic galaxy simulations (Mandelbaum et al. 2012) to constrain these three uncertainties together, which yielded a combined 3.5 per cent uncertainty largely independent of the lens redshift.

The other calibration biases that we consider to be independent are the impact of photo- z error (as discussed thoroughly in N12); stellar contamination, which we constrain using space-based data; PSF model uncertainty; and shear responsivity errors due to incorrect estimation of the rms galaxy ellipticity. Of these, the first is the dominant one (1, 2 and 3 per cent uncertainty for Main-L5, LRG and LRG-highz respectively – because as shown in N12, the systematic uncertainty is larger for higher redshift samples, where cosmic variance in the calibration samples is more important). Both stellar contamination and PSF model uncertainties are $\lesssim 0.5$ per cent. Shear responsivity uncertainty is 1 per cent for all samples. Thus, the three shear biases listed previously are the dominant uncertainty for all samples; when we add up the independent effects in quadrature, we obtain a 4, 5 and 5 per cent systematic uncertainty for Main-L5, LRG and LRG-highz, respectively.

For the purpose of simplifying the modelling, we assume that this final calibration uncertainty has a Gaussian error distribution, which may not be quite correct in detail. Moreover, since the errors were assessed in the same way for each lens sample, we assume that they are 100 per cent correlated – i.e. if the calibration is really 4 per cent too high for Main-L5, then it is 5 per cent too high for LRG and LRG-highz. We include this calibration uncertainty in the modelling of the lensing signal.

To test our understanding of the calibration biases, we present several ratio tests (Mandelbaum et al. 2005), i.e. comparisons of the signal computed using the same lens samples, but with different subsamples of the source catalogue. After we correct for our understanding of the calibration biases, we should find that the ratios of these signals are consistent with 1 within the errors.¹⁴

4.2.2 Scale-dependent systematics

Mandelbaum et al. (2010) includes a list of scale-dependent systematic errors that complicate the inference of cluster masses from the cluster lensing signal. Fortunately, many such errors are sufficiently small for galaxy-scale lenses and/or on the $> 2 h^{-1}$ Mpc scales that

we use for science that we can ignore them. The scale-dependent systematic errors that we do consider are intrinsic alignments of galaxy shapes (e.g. Hirata & Seljak 2004), given that we know some of our ‘sources’ are really physically associated with the lens and therefore may tend to point towards the lens. In principle, this effect can be quite important if we have no way of removing galaxies that are physically associated with lenses from our source sample; fortunately, our photo- z are sufficiently good that we are fairly successful at doing so. In Section B3, we estimate the importance of this effect based on the fraction of physically associated galaxies as a function of scale (see also Blazek et al. 2012).

The other main scale-dependent systematic error is the ‘systematic shear’ described in Section 4.1. While we can use the procedure described there to correct for it, we also must test the validity of that correction procedure, which we will do once we present the results in Section B5. Moreover, the systematic shear is the main factor that determines the maximum scale that we use; our maximum scales of ~ 30 (Main-L5) and $\sim 70 h^{-1}$ Mpc (LRG, LRG-highz) are motivated by a desire to avoid a situation where the correction for systematic shear is comparable in size to the real lensing shear.

4.3 Galaxy clustering

We compute the galaxy clustering signals using the same logarithmic binning size and maximum R as for the lensing, but with a minimum $R = 0.3 h^{-1}$ Mpc (which provides some measurements below R_0 for estimating $w_{\text{gg}}(R_0 = 4)$).

The estimation of clustering signals for the lens samples relies on SDSSPIX¹⁵ software to rapidly identify galaxy pairs within the required separation on the sky. To compute the galaxy autocorrelation $w_{\text{gg}}(R)$, we begin by computing the 3D galaxy correlation function ξ_{gg} on a grid of values in (R, Π) where Π is the comoving line-of-sight separation with respect to the mean position of the galaxies in the pair. Our estimator for the correlation function is a generalization of that from Landy & Szalay (1993),

$$\xi_{\text{gg}}(R, \Pi) = \frac{DD - 2DR + RR}{RR}, \quad (34)$$

using sums of products of weights rather than numbers of pairs of data–data, data–random and random–random pairs.¹⁶ Here, the weights for a given pair come from the product of the weight for each galaxy in the pair, where the weight per galaxy is initially defined as in Section 3 (e.g. equation 26). For the LRG and LRG-highz samples, there is an additional factor in the weight, to account for the fact that the g–g lensing and galaxy clustering measurements would have different effective weights since the g–g lensing automatically includes a lensing weight factor that depends on the redshift distribution of the source galaxies. This lensing weight is a decreasing function of redshift, and we include it in the clustering analysis so that the two measurements will not have different effective amplitudes (or even shapes, since the full scale-dependent matter clustering and non-linear bias can evolve with redshift). We define this weight by taking a grid of lens redshifts starting at our minimum lens redshift and having $\Delta z = 0.01$, and for each lens redshift on the grid, we use our source sample to identify lens–source pairs in the full range of R used for this analysis, with $w(z) = \sum_{\text{ls}} w_{\text{ls}}$. The

¹⁵ <http://dls.physics.ucdavis.edu/~scranton/SDSSPIX/>

¹⁶ To reduce the noise, we have many more random points than real points. Here, all numbers such as DR and RR (or their generalization in terms of pairs of products of weights) are properly normalized to account for this fact.

¹⁴ For the combinations of lens and source redshifts used here, the predicted differences in those ratios due to reasonable variations on our adopted cosmological model are at the 0.1 per cent level, well within the errors.

weight therefore includes the photometric redshift distribution of the sources, and all appropriate weight factors. In practice, it turns out that this weight is not important for Main-L5 because those galaxies are well below the bulk of the source redshift distribution and because the Main-L5 redshift distribution is rather narrow. For LRGs, it is more important, changing the effective redshift of the clustering measurement by $\Delta z = 0.03$.

The projected correlation function $w_{\text{gg}}(R)$ is formally defined as

$$w_{\text{gg}}(R) = \int \xi_{\text{gg}}(r = \sqrt{R^2 + \Pi^2}) d\Pi \quad (35)$$

integrated along the entire line of sight. In practice, we compute $w_{\text{gg}}(R)$ via a limited summation,

$$w_{\text{gg}}(R) = \Delta\Pi \sum_i \xi_{\text{gg}}(R, \Pi_i), \quad (36)$$

in 40 bins in Π that are linearly spaced with $\Delta\Pi = 3 h^{-1}$ Mpc, spanning a range $-\Pi_{\text{max}} \leq \Pi \leq \Pi_{\text{max}}$, for $\Pi_{\text{max}} = 60 h^{-1}$ Mpc (we consider the impact of this choice of Π_{max} in Appendix C).

To estimate $\Upsilon_{\text{gg}}(R)$, we use equation (13), replacing Σ with w_{gg} , which requires an estimate of $w_{\text{gg}}(R_0)$. As for the lensing signal, we identify a range of scales for which the signal is approximately a power law, and fit w_{gg} to a power law on those scales to estimate $w_{\text{gg}}(R_0)$. Tests of this determination of $w_{\text{gg}}(R_0)$ are presented in Section C1. We then employ equation (13) to get Υ_{gg} ; the first term, an integral over all scales above R_0 , is done via summation. For each bin, we effectively assume a constant w within the bin, and we carefully account for partial bins that fall in the R range of interest.

As for the lensing signal, we use the division of the lens samples into equal-area jackknife regions to compute covariance matrices, and we present the results of the jackknife covariances and modelling them to reduce the noise in Section 6.2.

4.4 Galaxy clustering systematic errors

There are several possible systematic errors in the calculation of the galaxy clustering statistics.

One issue is the handling of the integral in equation (36), with the finite line-of-sight cutoff. Naively, we can account for this in our modelling of the clustering signal by integrating the theoretical 3D correlation function to the same line-of-sight cutoff. However, as illustrated by Padmanabhan, White & Eisenstein (2007), this approach is uncertain at the level of tens of per cent on large scales by RSD, and a linear treatment (Kaiser 1987) is not likely to be adequate on these scales (e.g. Reid & White 2011). Fortunately, as illustrated by Baldauf et al. (2010), the uncertainty induced by the RSD is far less important for the observable that we use for science, Υ_{gg} . As shown in Fig. 8 (right-hand panel) in that paper, the impact of RSD and the finite line-of-sight cutoff is reduced from ~ 30 per cent bias on w_{gg} to ~ 5 per cent bias on Υ_{gg} at the maximum scale that we use for science, and is very small below $30 h^{-1}$ Mpc. We could apply a correction for this small, residual systematic error, but as described in Section 2.3.4, a combined correction for this effect and others (e.g. the lensing window, which goes in the opposite direction) is so small as to be negligible for our analysis.

Because Υ_{gg} is a partially compensated statistic, it is also less sensitive to large-scale density fluctuations that can shift w_{gg} up and down. We will demonstrate the effect of this on the cosmic variance component of the errors in Section 6.2. The same argument is true for the integral constraint, which will lead to a constant offset in w_{gg} which goes away when computing Υ_{gg} .

There are also a question of how sample definition choices affect the measured statistics. Kazin et al. (2010) consider several such effects for w_{gg} , including the method of distributing the random points in redshift, and the way of handling fibre collisions in the weighting. Their conclusion that these issues are only important at the few per cent level at most is also applicable to our results, and thus this systematic error is subdominant to the statistical and systematic uncertainties in the lensing signal.

5 RESULTS OF LENSING MEASUREMENTS

In this section, we present the galaxy–galaxy lensing measurements (Section 5.1), the error estimates (Section 5.2). Tests for systematic errors are in Appendix B.

5.1 Observations

The lensing signals for all three samples are shown in Fig. 6. This figure shows the observable quantity, $\Delta\Sigma$, and also the quantity used for cosmological constraints, $\Upsilon_{\text{gm}}(R_0 = 2 h^{-1}$ Mpc), plotted as $R\Upsilon$ for easier viewing on a linear scale. Clearly the S/N of the observable is quite high – typically ~ 25 averaged over all scales, using

$$\frac{S}{N} = (\mathbf{x}^T \mathbf{C}^{-1} \mathbf{x})^{1/2}, \quad (37)$$

where \mathbf{x} is the vector of $\Delta\Sigma$ values in each radial bin and \mathbf{C} is their covariance matrix, to account for correlations between bins. The shear is well constrained down to a level of $\sim 5 \times 10^{-5}$ (at $\sim 5^\circ$ angular separations), and the results are statistically consistent with previously published ones for LRGs with $R < 4 h^{-1}$ Mpc (Mandelbaum et al. 2006b). A comparison with previous Main-L5 observations is complicated by our imposition of a redshift cut

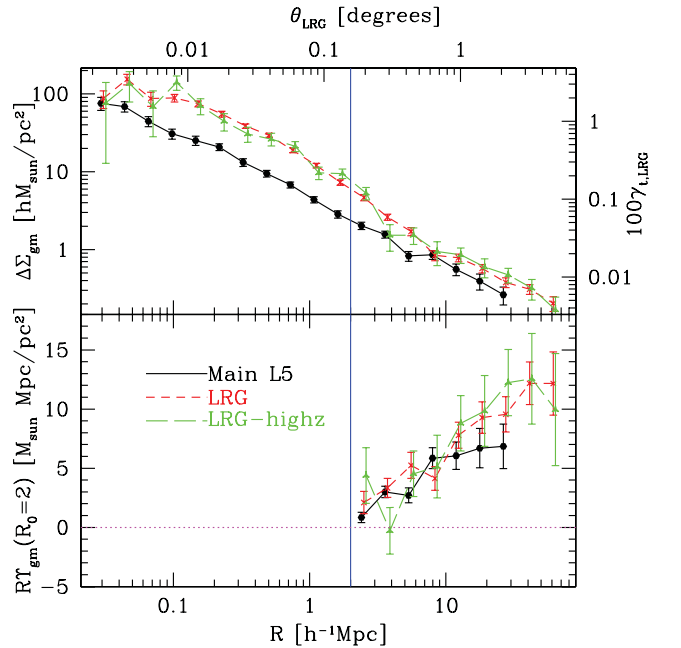


Figure 6. Top: observed lensing signal $\Delta\Sigma_{\text{gm}}(R)$ for all three lens samples. The vertical line indicates the minimum scale used for cosmological constraints. The axes on the top and right indicate the angular scale θ and the tangential shear $100\gamma_t$ for the LRG sample. Bottom: $R\Upsilon_{\text{gm}}(R; R_0 = 2)$ for all three samples as labelled on the plot.

$z < 0.155$, and this is the first such galaxy–galaxy lensing observation for LRG-highz.

Υ_{gm} is a lower S/N quantity, with total average S/N of 11, 14 and 8 for Main-L5, LRG and LRG-highz, respectively, averaged over the range of scales ($2 < R < 70 h^{-1}$ Mpc) shown on the plot.

A detailed discussion of tests for systematic errors in the lensing signal is in Appendix B.

5.2 Covariance matrices

Here, we present the error estimates for the Υ_{gm} results shown above. As stated in Section 4.1, the noisiness of the jackknife covariance matrices requires some correction in order to get cosmological parameter estimates. Rather than modifying the procedure for using them to get confidence intervals, as in Hirata et al. (2004) or Hartlap et al. (2007), we instead model the matrices to make noiseless versions.

The process begins by modelling the diagonal terms of the covariance matrix as a function of R . We refer to the covariance matrix for Υ_{gm} as $\mathbf{C}_{\text{gm}}^{(\Upsilon)}$ with elements corresponding to radial bins i and j of $\mathbf{C}_{\text{gm}}^{(\Upsilon)}(R_i, R_j)$. Our smooth model is

$$\mathbf{C}_{\text{gm}}^{(\Upsilon)}(R_i, R_j) = AR^{-2}[1 + (R/R_t)^2], \quad (38)$$

with an amplitude A and a turnover radius R_t . This two-parameter model is motivated as follows: on all scales, we expect sampling variance to be minimal because of the large area and the compensated nature of Υ , so shape noise should be the dominant source of error. The shape noise variance scales like R^{-2} for logarithmically spaced annular bins, and we fit for the amplitude A of this term. However, as shown in Jeong, Komatsu & Jain (2009), above some radius the shape noise fails to decrease as rapidly with R , in the regime where R is significantly larger than the typical separation between lenses. In that case, the lens–source pairs in the annular bin include many of the same sources around nearby lenses, so the shape noise does not decrease by adding more lenses. The term in brackets in equation (38) represents this flattening of the errors with scale. (There will also be a corresponding increase in bin-to-bin correlations on those scales, as will shortly be apparent.)

Our approach is to model the diagonal elements of the covariance matrix by directly fitting for (A, R_t) for each lens sample using χ^2 minimization, doing an unweighted fit for $\log C_{\text{gm}}^{(\Upsilon)}(R_i, R_i)$ as a function of $\log R$. The scale on which the term in brackets in equation (38) becomes important is $R_t = (8, 31, 41) h^{-1}$ Mpc for the three samples. This trend of R_t is unsurprising given the trends in lens number density for the three samples. In the top panel of Fig. 7, we show a comparison between the jackknife covariance diagonal terms and those from the model, for the LRG sample. As shown, the RMS level of fluctuations of the jackknife variances compared to those in the model is 12 per cent.

Next, we model the off-diagonal terms, which are also somewhat noisy. Off-diagonal terms can arise due to (a) cosmic variance (not very significant for this sample), (b) correlated shape noise due to the large R compared to the separation between lenses and (c) the fact that $\Upsilon(R)$ at some radius depends on the $\Delta\Sigma(R_0)$, which tends to anticorrelate bins at $R \sim R_0$ with each other. Since there are several sources of correlations, they are not as simple to model analytically. Thus, we take a non-parametric approach, by generating the correlation matrix, i.e. \mathbf{C}_{corr} , defined by

$$\mathbf{C}_{\text{corr},i,j} = \frac{\mathbf{C}_{\text{gm}}^{(\Upsilon)}(R_i, R_j)}{\sqrt{\mathbf{C}_{\text{gm}}^{(\Upsilon)}(R_i, R_i)\mathbf{C}_{\text{gm}}^{(\Upsilon)}(R_j, R_j)}}. \quad (39)$$

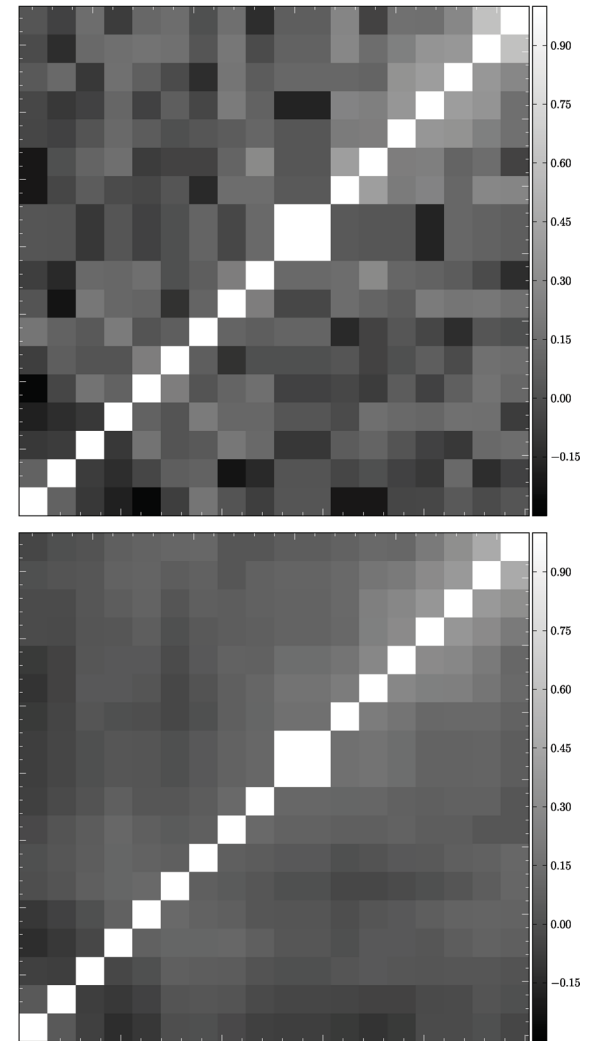
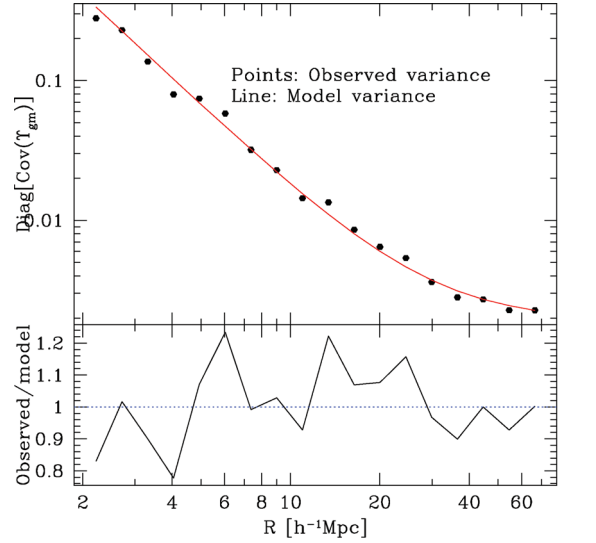


Figure 7. Top: a comparison of the jackknife covariance matrix diagonal terms for Υ_{gm} for the LRG lens sample with the model covariance matrix terms as a function of transverse separation R . Middle: Jackknife correlation matrix for Υ_{gm} , again for LRG lenses. Bottom: smoothed correlation matrix for Υ_{gm} .

We then apply a boxcar smoothing algorithm with a length of three bins in radius to this matrix, to reduce the noise. The middle and bottom panels of Fig. 7 show the unsmoothed and smoothed correlation matrix for the LRG sample. As shown, the smoothing has not resulted in any significant modification of the apparent real trends, but has eliminated the majority of the noise.

6 RESULTS OF CLUSTERING MEASUREMENTS

In this section, we present the galaxy clustering measurements (Section 6.1), the error estimates (Section 6.2) and cross-covariance with the lensing results (Section 6.3). Tests for systematic errors in the clustering measurements are in Appendix C.

6.1 Observations

The clustering signals for all three samples are shown in Fig. 8. This figure shows the observable quantity, w_{gg} , and also the quantity used for cosmological constraints, $\Upsilon_{\text{gg}}(R_0 = 4 h^{-1} \text{ Mpc})$ (plotted as $R\Upsilon$ for easier viewing on a linear scale). Clearly the S/N of the observable is quite high, significantly more so than for the lensing observable. Υ gives a total average S/N of 19, 33 and 32 (Main, LRG, LRG-highz) when averaged over scales $R > 4 h^{-1} \text{ Mpc}$ using equation (37).

As discussed in Section 4.3, these results include a redshift-dependent weighting factor so that the effective redshift will be the same as for the galaxy–galaxy lensing measurement. Thus, they cannot be directly compared with previous measurements of LRG and LRG-highz sample clustering without checking the effect of this weighting. We find that for the LRG (LRG-highz) sample, inclusion

of the lens-weighting factor has lowered the amplitude of w_{gg} by 4 (2) per cent¹⁷ and increased the errors by ~ 10 per cent. Thus, if we had not included it, then with the same lensing signal but a higher clustering signal we would have inferred a lower σ_8 by 2 (1) per cent when analysing these samples, which is of similar order as other calibration factors we have considered and therefore validates our choice to include this redshift weighting properly.

The bottom panel of Fig. 8 shows the ratio of the measured signal for the LRG sample from Zehavi et al. (2005) to our measurement *without the lens weighting*, with the differences being due to our use of nearly twice as much area (7131 versus 3836 degrees²) and the different line-of-sight integration lengths (± 60 versus $\pm 80 h^{-1} \text{ Mpc}$). Even with these differences, the results agree at the 1 per cent level; the results agree to well within the naively propagated errors because the results are actually correlated to some extent, and this agreement shows that we have not done anything substantively different from the perspective of systematic errors. Additional tests for systematic errors in the clustering measurements are in Appendix C.

6.2 Covariance matrix

Here, we present the error estimates for the quantities shown above, in particular, the Υ_{gg} results. We follow the approach from Section 5.2 of modelling the covariance matrices to reduce the noise, again showing results for the LRG sample as an example.

The process begins by modelling the diagonal terms of the covariance matrix as a function of R . We refer to the covariance matrix for $\Upsilon_{\text{gg}}^{(\Upsilon)}$ as $\mathbf{C}_{\text{gg}}^{(\Upsilon)}$ with elements corresponding to radial bins i and j of $\mathbf{C}_{\text{gg}}^{(\Upsilon)}(R_i, R_j)$. Our smooth four-parameter model is

$$\mathbf{C}_{\text{gg}}^{(\Upsilon)}(R_i, R_j) = A_1 R^{\alpha_1} + A_2 R^{\alpha_2}, \quad (40)$$

a sum of a shallower and a steeper power law, which dominate on larger and smaller scales, respectively. The choice of this functional form comes from the fact that for Υ_{gg} there is an additional noise component on small scales due to propagated uncertainty in $w_{\text{gg}}(R_0)$.

We model this term by directly fitting for $(A_1, \alpha_1, A_2, \alpha_2)$ for each lens sample using χ^2 minimization, doing an unweighted fit for $\log \mathbf{C}_{\text{gg}}^{(\Upsilon)}(R_i, R_j)$ as a function of $\log R_j$. In the top panel of Fig. 9, we show a comparison between the jackknife covariance diagonal terms and those from the model, for the LRG sample. As shown, the level of fluctuations of the observed variances compared to those in the model is 17 per cent (but there is a fairly extreme outlier; excluding that one noticeably decreases the estimated scatter). Smoothing the diagonal terms to reduce the influence of this outlier is important; too low a variance would result in that bin unfairly dominating the fits.

Next, we model the off-diagonal terms, which are also somewhat noisy. Off-diagonal terms can arise due to cosmic variance (not very significant for this compensated statistic Υ_{gg}), but also a small contribution from the fact that $\Upsilon_{\text{gg}}(R)$ at some radius depends on $w_{\text{gg}}(R_0)$, which tends to anticorrelate bins at $R \sim R_0$ with each other. Since there are several sources of these correlations, they are not

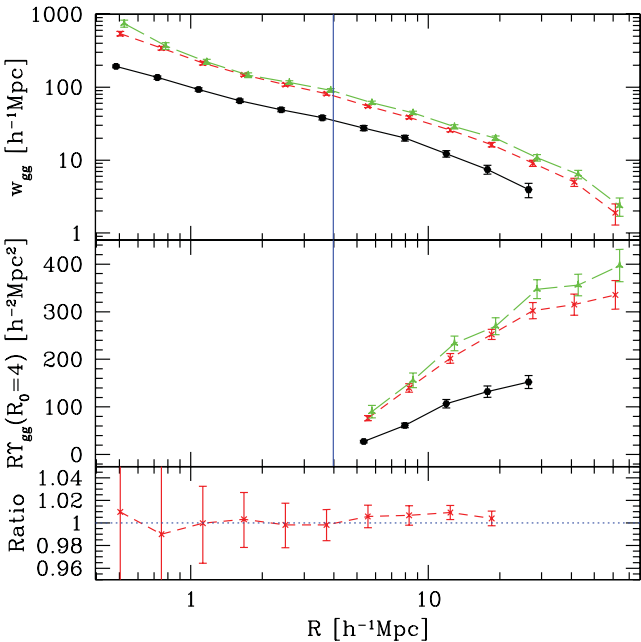


Figure 8. Top: observed clustering signal $w_{\text{gg}}(R)$ for all three lens samples, including lens-weighting factors for LRG and LRG-highz. The vertical line indicates the minimum scale used for cosmological constraints. Line colours and types indicate the sample, using the same scheme as Fig. 6. Middle: $R\Upsilon_{\text{gg}}(R; R_0 = 4)$ for all three samples as labelled on the plot. Bottom: for the LRG sample, the ratio of w_{gg} from Zehavi et al. (2005) to that from our work without lens-weighting, after accounting for the different radial binning.

¹⁷ The expected sign and magnitude of the effect is not completely clear; for a passively evolving population, the sign should in fact be the opposite. However, we have split the LRG samples into redshift slices and confirmed that within the redshift range of the LRG sample, the amplitude of w_{gg} evolves by as much as 10 per cent, with lower amplitude at lower redshift, consistent with our findings with lens weighting included.

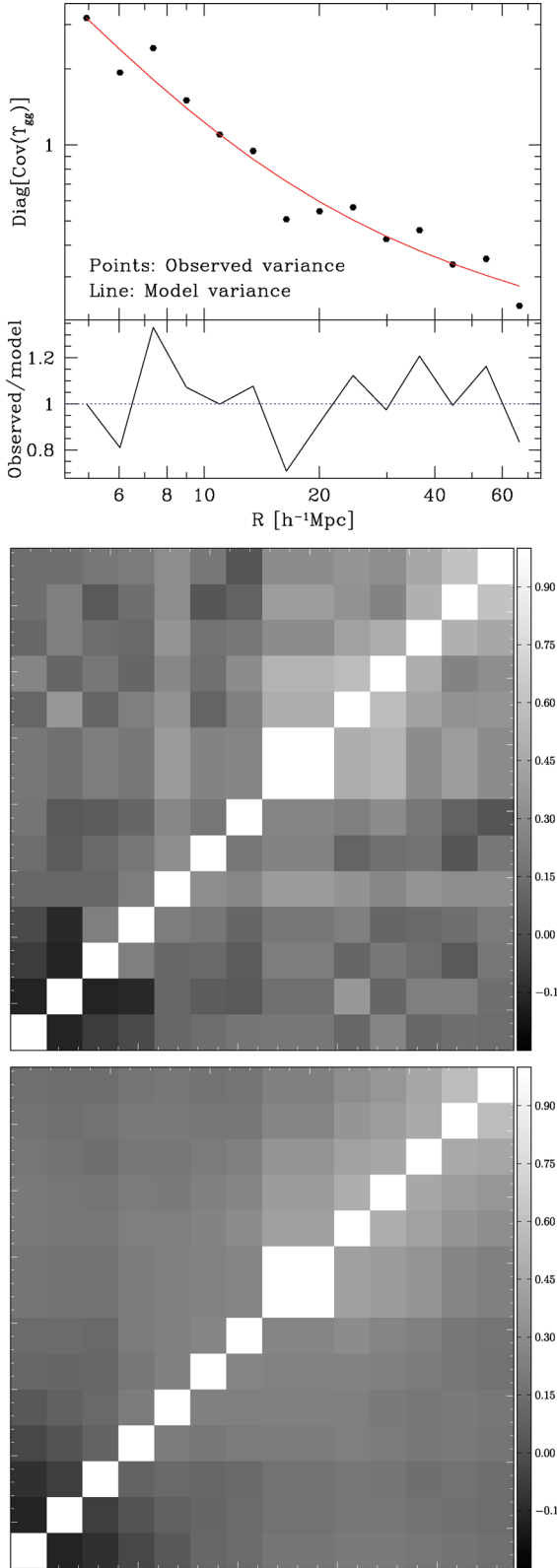


Figure 9. Top: a comparison of the jackknife covariance matrix diagonal terms for Υ_{gg} for the LRG sample, with the model covariance matrix terms as a function of transverse separation R . Middle: Jackknife correlation matrix for Υ_{gg} for the LRG lens sample. Bottom: smoothed correlation matrix for Υ_{gg} .

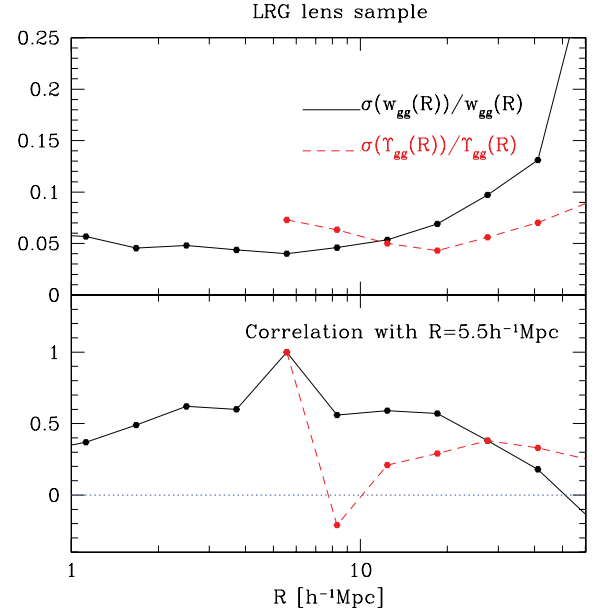


Figure 10. Error comparison for w_{gg} (black solid lines) and Υ_{gg} (red dashed lines) for the LRG lens sample. Top: standard deviation of these statistics (i.e. the square root of the diagonal covariance matrix elements) as a function of R , divided by the signal itself. Bottom: correlation of the data at each bin in radius with the bin above $R = R_0 h^{-1} \text{Mpc}$.

as simple to model analytically. Thus, we take a non-parametric approach, by generating the correlation matrix, i.e. \mathbf{C}_{corr} , defined by

$$\mathbf{C}_{\text{corr},i,j} = \frac{\mathbf{C}_{gg}^{(\Upsilon)}(R_i, R_j)}{\sqrt{\mathbf{C}_{gg}^{(\Upsilon)}(R_i, R_i)\mathbf{C}_{gg}^{(\Upsilon)}(R_j, R_j)}}. \quad (41)$$

We then apply a boxcar smoothing algorithm with a length of three bins in radius to this matrix, to reduce the noise. The middle and bottom panels of Fig. 9 show the unsmoothed and smoothed correlation matrix for the LRG sample. As shown, the smoothing has not resulted in any significant modification of the apparent real trends, but has eliminated the majority of the noise.

We also compare the covariance matrices for w_{gg} and Υ_{gg} , to check that they behave in the way that we expect with respect to reduced cosmic variance in the latter due to its compensated nature (Section 2). Fig. 10 illustrates this difference, using the LRG sample as an example. Here, we have rebinned the data and covariances by a factor of 2, because we do not have a smoothed version of the covariance matrix for w_{gg} . As shown, the relative error (top panel) on Υ_{gg} is larger near R_0 , because Υ_{gg} is defined to be near zero there, but on large scales, w_{gg} has a larger fractional error due to cosmic variance. We also study the correlation properties of these statistics. As shown (bottom panel), w_{gg} exhibits larger correlations between nearby bins. This is a consequence of cosmic variance: large-scale modes can coherently shift w_{gg} up or down, resulting in bin-to-bin correlations. In contrast, Υ_{gg} shows less significant correlation patterns.

We also compare these error properties versus the expected ones from the simulations. For the simulations, the volume has been divided into $1.5 \times 1.5 \times 0.3 = 0.67(\text{Gpc } h^{-1})^3$ subvolumes, almost exactly the size of our observed volume but with slightly different geometry. There are 40 such subvolumes, which we use to estimate covariance matrices by comparing the signals computed in each one. This test serves as a check on the jackknife method that we

Table 3. Fits for cosmological parameters described in Section 7.1. In each case, parameters that are fixed to a single value are in bold; those that are fit are shown with 68 per cent confidence limits after marginalizing over all other fitted parameters.

Fit	Sample	σ_8	Ω_m	b (L5)	b_2 (L5)	b (LRG)	b_2 (LRG)	b (LRG-highz)	b_2 (LRG-highz)	χ^2	ν	$p(> \chi^2)$
1	L5	$0.89^{+0.07}_{-0.08}$	0.25	1.25 ± 0.05	-0.12 ± 0.18	–	–	–	–	29.8	19	0.06
2	LRG	0.79 ± 0.06	0.25	–	–	2.07 ± 0.05	$0.98^{+0.28}_{-0.24}$	–	–	19.3	27	0.86
3	LRG-highz	0.81 ± 0.10	0.25	–	–	–	–	2.26 ± 0.06	$0.94^{+0.66}_{-0.54}$	20.5	27	0.81
4	All	0.80 ± 0.05	0.25	1.38 ± 0.05	-0.02 ± 0.20	2.03 ± 0.05	$0.94^{+0.24}_{-0.20}$	2.28 ± 0.06	$1.00^{+0.46}_{-0.50}$	71.3	77	0.66
5	All	0.76 ± 0.08	$0.269^{+0.038}_{-0.034}$	1.46 ± 0.06	-0.06 ± 0.26	2.15 ± 0.07	$0.96^{+0.36}_{-0.26}$	2.44 ± 0.11	$0.84^{+0.58}_{-0.64}$	71.6	76	0.63

carry out on the real data. We find that the scaling of $\sigma(w_{\text{gg}})/w_{\text{gg}}$ in the simulations and data is extremely similar for all scales that we use. For Υ_{gg} the same is generally true, though the errors near R_0 seem to be ~ 20 per cent larger in the simulations than in the data, but the opposite is true at higher R , with the two in agreement around $8 h^{-1}$ Mpc. This may be attributed to the method of determining $w_{\text{gg}}(R_0)$, which differs slightly between the data analysis and simulations. Nonetheless, the comparison between errors in the simulations and in the real data is very similar, and should alleviate any concerns about the jackknife error bars used in practise. We have also confirmed that the correlation properties for w_{gg} and Υ_{gg} in the simulations are consistent with those we observe in the real data (bottom of Fig. 10).

6.3 Cross-covariance with lensing

Using the jackknife resampling, we are able to compute the cross-covariance between the lensing and clustering observations. Our findings are that on all scales, these correlations are consistent with zero, except possibly on the largest scales where they reach 10–15 per cent. This result is unsurprising given that the dominant source of error in our observations is the lensing shape noise. So, for the purpose of cosmological parameter constraints, we set the cross-terms between lensing and clustering in the covariance matrix to precisely zero.

For future work with surveys that are not as limited by shape noise, these covariances will be important to model accurately.

7 COSMOLOGICAL PARAMETER CONSTRAINTS

In this section, we present cosmological parameter constraints derived from the data that were shown in the previous section.

7.1 Constraints with these data alone

We use the standard `COSMOMC` (Lewis & Bridle 2002) package to make statistical inferences from our data. The package has been extended with a module that models our signals as described above and provides the likelihood that can be turned into posterior probability either alone or in conjunction with another data set. We use the standard `COSMOMC` parametrization of cosmology with flat priors on the following parameters $\omega_b = \Omega_b h^2$ (baryon density), ω_{cdm} (cold dark matter density), θ (angular diameter distance of the surface of last scattering, a proxy for Hubble’s constant), τ (optical depth to the surface of last scattering), w (dark energy equation of state), n_s (spectral index of primordial fluctuations) and A (amplitude of the primordial fluctuations; however, we quote our results in terms of the more commonly used parameter σ_8). On top of these priors,

we include a prior that is flat in σ_8^5 , based on our calibration on simulations in Appendix A. We vary parameters specific to our data set: two bias parameters for each data set and a common calibration parameter c as discussed in Sections 2.3.4 and 4.2.1.

We start by performing the analysis using SDSS lensing and clustering data without any external priors from e.g. CMB data; this analysis is carried out both in individual redshift bins and combined. For these tests, we fix the cosmological parameters to $\Omega_m = 0.25$, $n_s = 0.96$ and $h = 0.7$, only varying σ_8 , the bias parameters, and the lensing calibration parameter. We do this fit for each sample separately, and for all three together (Table 3, fits 1–4).

With these fits, we can do a basic sanity test for consistency between samples. In Fig. 11, we show the data with the best-fitting signals. The model appears to fit the data quite well, without any signs of systematic tension, consistent with the reasonable χ^2 and p -values in Table 3.

Fig. 12 shows the posterior distributions for the bias parameters for each sample; we show the results from fits 1–3 (fitting for the samples separately) and 4 (fitting all together). Fig. 13 shows the 1D posterior distributions for σ_8 for each sample separately and the combined result (fits 1–4), in all cases marginalized over the bias parameters. The corresponding limits on σ_8 when using all samples together (as in Table 3, fit 4) are 0.80 ± 0.05 (68 per cent confidence level, stat. + sys.). Figs 11–13 demonstrate clearly that there is no statistically significant tension between cosmological parameter constraints from the different samples.

The results in Fig. 12 suggest that for LRG and LRG-highz, we detect non-linear bias at the $>3\sigma$ and $\sim 1.5\sigma$ levels, respectively (the results in Table 3 are deceptive; they suggest less significant detections, because the error bars are quite non-Gaussian). The non-detection for L5 does not mean that we find that the bias is linear on all scales, only above $\sim 4 h^{-1}$ Mpc. Quantitatively, we find a $\Delta\chi^2$ for the best-fitting model with b_2 free versus that with $b_2 = 0$ (linear bias only) of (0.2, 32, 4.5) for Main-L5, LRG and LRG-highz, respectively. That number for Main-L5 confirms the non-detection of non-linear bias, but the $\Delta\chi^2$ for LRG suggests a $>3\sigma$ detection of non-linear bias, with a marginal detection for LRG-highz. As expected, the best-fitting model with $b_2 = 0$ has higher $\sigma_8 = 0.85, 0.83$ for LRG and LRG-highz, to accommodate the increased clustering below $10 h^{-1}$ Mpc due to non-linear bias. Note that the hierarchy of bias values for these samples roughly mirrors the trends previously detected for galaxy bias as a function of luminosity determined in SDSS using relative bias measurements, for example by Swanson et al. (2008). Furthermore, the LRG linear and quadratic biases are consistent with values that were previously measured using a combination of the two- and three-point correlation functions (Marín 2011). While the value of b_2 for the LRG sample is roughly 2σ above the value that describes the simulated sample in Fig. 1, this may simply reflect slightly stronger clustering

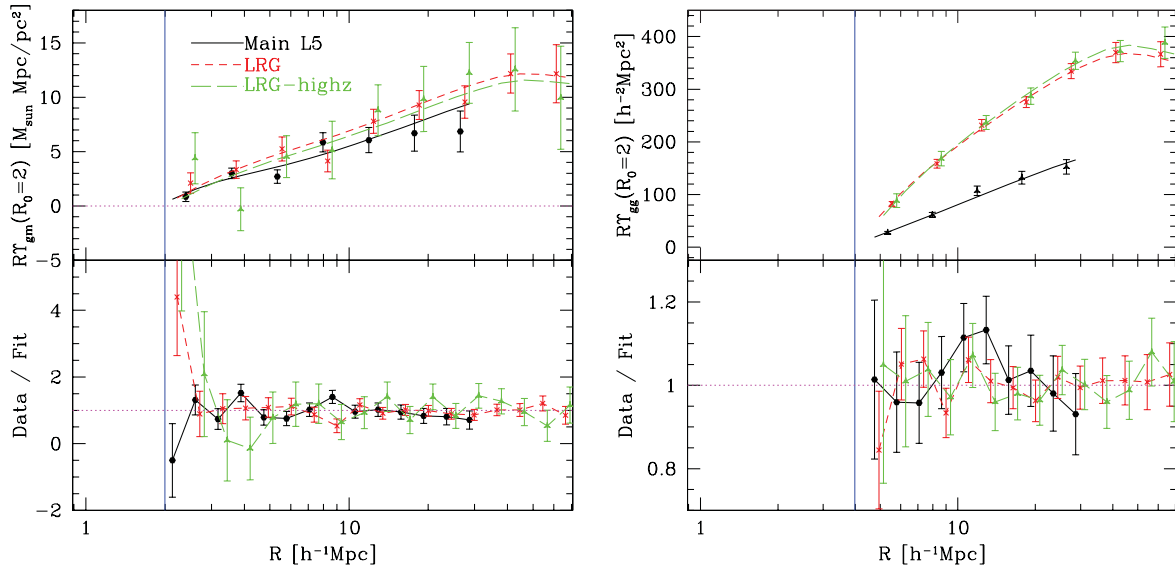


Figure 11. Top left: observed RT_{gm} with best-fitting signals from fits 1–3 in Table 3; for these fits, the data were fit separately for each sample. Data have been rebinned for easier viewing. Bottom left: ratio of observed to best-fitting signal from the top panel, using the original narrower binning as for the actual fit. Right: same as left, but for clustering RT_{gg} .

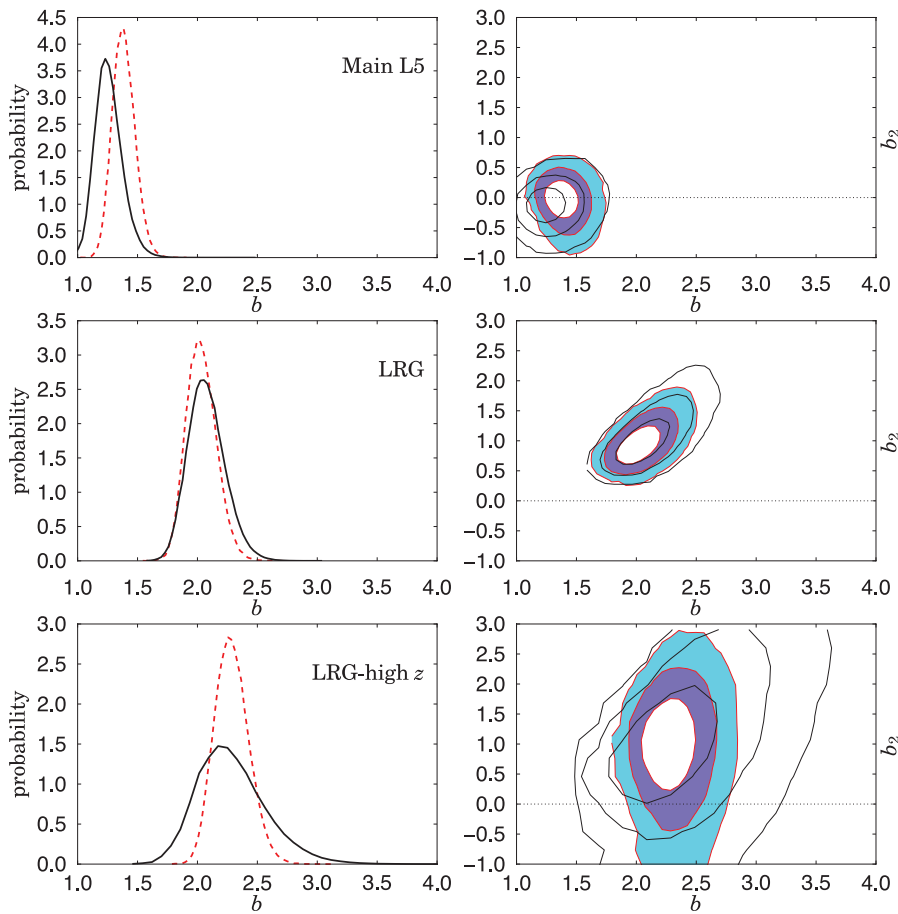


Figure 12. Best-fitting galaxy bias parameters for Main-L5 (top), LRG (middle) and LRG-high z (bottom). Left: the posterior probability distribution for the large-scale galaxy bias b , marginalized over other parameters including the non-linear bias parameter b_2 . The solid black lines show the results for fits 1–3, fitting for each sample separately; the dashed red lines are the results from fit 4, jointly fitting all samples. Right: contour plots for the large-scale bias b versus non-linear bias parameter b_2 (1, 2 and 3σ). The black line contours show the results from fits 1–3, fitting for each sample separately; the coloured contours show the results from fit 4, jointly fitting all samples.

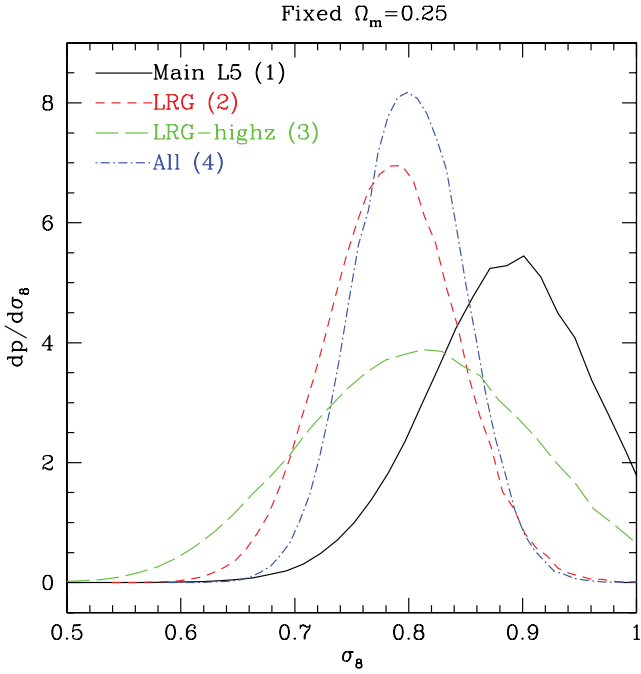


Figure 13. Posterior distribution for σ_8 marginalized over all other fit parameters, for fits 1–4 (Ω_m fixed).

on small scales, which can result from even slightly larger satellite fractions.

As described in Section 2.3.4, we have included an arbitrary galaxy–galaxy lensing signal calibration uncertainty with a Gaussian standard deviation of (0.04, 0.04, 0.05) for the three samples, assuming that the calibration is perfectly correlated between them. Given this prior, we find that the best fit is obtained with a calibration that is 0.1σ from the expected value (this decrease in the signal is illustrated in Fig. 11 via an increase of the theoretical model). If we instead fix the lensing calibration without allowing any freedom, the best-fitting σ_8 changes by an amount that is well below our quoted error, and the errors become smaller by 20 per cent. These findings suggest that systematic uncertainty due to uncertain lensing calibration is not completely negligible, but does not dominate our error budget.

We have also carried out these fits with the off-diagonal elements of the covariance matrix set to zero for both lensing and clustering for all samples, in order to test how sensitive we are to the treatment of off-diagonal elements. We find that the best-fitting σ_8 changes by 0.01 (0.2σ), and the size of the error regions becomes smaller by 15 per cent. Thus, our results are relatively stable to inclusion of correlations between radial bins.

As an empirical test of the σ_8^5 prior that was justified using simulated data in Appendix A, we confirm that when we remove the σ_8^5 prior for fit 4, σ_8 for the most likely point in the full fit parameter space does not correspond to that of the median of the posterior distribution after marginalizing over nuisance parameters. The sign of the difference is the same of that in the simulated data in the Appendix; the magnitude of the difference is slightly larger than that in the simulations, but the effects are consistent in the simulations and real data once we take into account the far larger noise in the real data. Thus, there is no indication from the data that the assumptions behind our σ_8^5 prior are incorrect, so we use this prior for all fits that include the SDSS lensing and clustering data.

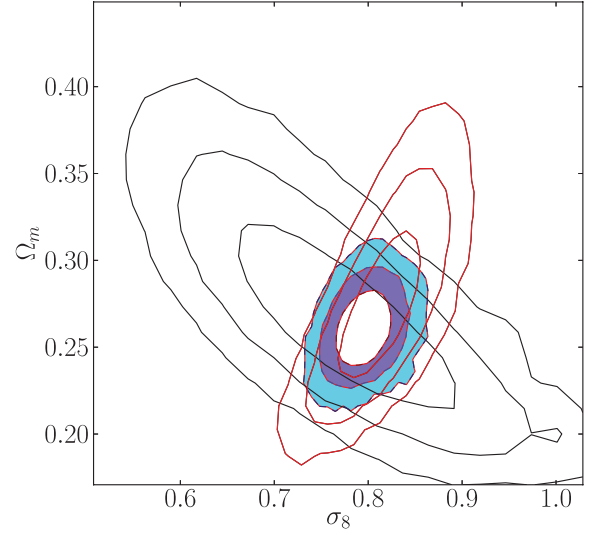


Figure 14. Open black lines show the contours in the σ_8 versus Ω_m plane (fit 5) for our data set, marginalizing over all linear and non-linear bias parameters and lensing calibration. The contours that are shown are 1, 2 and 3σ . The nearly orthogonal open red contours are for *WMAP7* (also fitting for n_s , H_0 and other parameters in flat Λ CDM as in Section 7.2), and the filled contours are for *WMAP7* combined with our data.

Next, we have allowed the matter density Ω_m to vary (fit 5 in Table 3, using all three samples together). In this case, there is a classic degeneracy between σ_8 and Ω_m in the lensing data, with higher σ_8 requiring a lower Ω_m to fit the data. Because of this degeneracy, the allowed range of σ_8 becomes broader, $\sigma_8 = 0.76 \pm 0.08$ when marginalized over Ω_m , the bias parameters and the lensing calibration (still a 10 per cent constraint on σ_8 even with this degeneracy). When marginalizing over σ_8 , we can constrain $\Omega_m = 0.269^{+0.038}_{-0.034}$. The resulting 2D contour plot for these two parameters is shown in Fig. 14. The best-constrained parameter combination, which is a better illustration of our overall S/N, is $\sigma_8(\Omega_m/0.25)^{0.57} = 0.80 \pm 0.05$ (1σ , stat. + sys.), representing a 6 per cent uncertainty in the amplitude of matter fluctuations. We do not show the best-fitting signal for this case, because it differs very little from that shown in Fig. 11.

7.2 Combination with other data

We combine these data with *WMAP7* CMB results (Komatsu et al. 2011), anticipating significant benefit from a tight prior on the amplitude of matter fluctuations at early times. For the first combined fit, we vary (A , ω_{dm} , ω_b , θ , τ , n_s) (see definitions at start of Section 7.1), the six bias parameters for the three galaxy samples and the lensing calibration with its (4, 5, 5) per cent Gaussian prior – with fixed $w_{\text{de}} = -1$ and $\Omega_k = 0$. We include lensing of the CMB and marginalize over a Sunyaev-Zeldovich (SZ) template as in Komatsu et al. (2011). All results in this section that use our data include our σ_8^5 prior from Appendix A, but that prior was not included for the analyses that use *WMAP7* data alone.

Fig. 15 shows 2D parameter contours with *WMAP7* alone and combined with these data (the Ω_m versus σ_8 contour was already shown in Fig. 14). We can see that since the degeneracy direction for σ_8 versus Ω_m for the CMB data is orthogonal to that for lensing data (Fig. 14), adding our data to the *WMAP7* data roughly halves the size of the allowed regions in parameter space. However, the top panel of Fig. 15 shows that the constraints on n_s are,

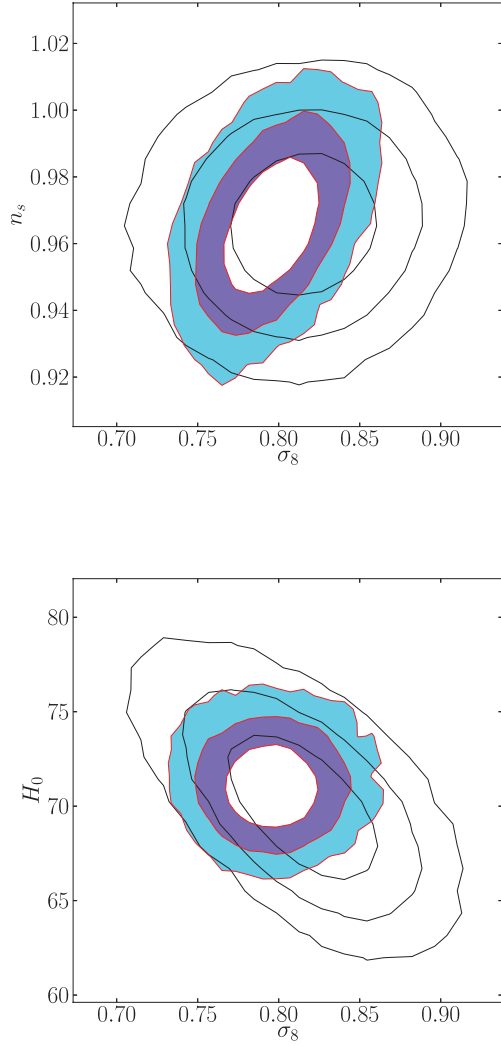


Figure 15. Contour plots of 2D probability distributions for fits using the *WMAP7* data along with our new results for galaxy–galaxy lensing and galaxy clustering in SDSS, assuming flat Λ CDM. In all cases, we have marginalized over the nuisance parameters (bias and calibration) for our data, and over any cosmological parameters not shown on the plot. The black lines show 1, 2 and 3σ contours for *WMAP7* alone. The contours shown in colour are *WMAP7* and our data together. Top: σ_8 versus n_s ; bottom: σ_8 versus H_0 .

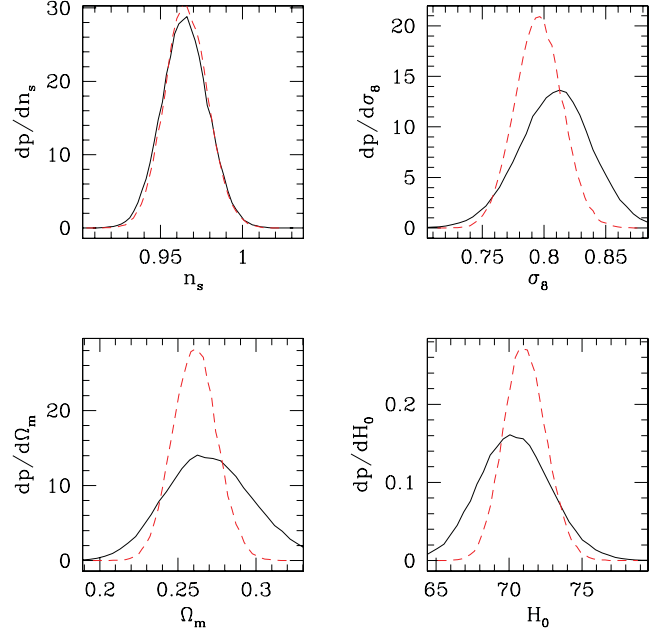


Figure 16. 1D probability distributions for fits using the *WMAP7* data along with our new results for galaxy–galaxy lensing and galaxy clustering in SDSS, assuming flat Λ CDM as in Fig. 15. In all cases, we have marginalized over the nuisance parameters (bias and calibration) for our data, and over any cosmological parameters not shown on the plot. The solid black lines are for *WMAP7* alone; the red dashed lines are for *WMAP7* and our data together.

unsurprisingly, set exclusively by the *WMAP7* data. The bottom panel shows that we also provide additional constraining power on H_0 , through the stronger constraint on Ω_m (and the fact that CMB constrains a different parameter combination, $\Omega_m h^2$). The resulting 1D probability distributions for $(n_s, \sigma_8, \Omega_m, H_0)$, marginalized over other parameters, are shown in Fig. 16.

Table 4 gives best-fitting parameters and their 68 per cent confidence intervals from these fits, for *WMAP7* alone and for *WMAP7* plus these data (fits 6 and 7). As shown in Figs 15 and 16, the parameters for which constraints improve significantly by combination of these data sets are σ_8 , Ω_m and H_0 . In these combined fits, there is little tension between the data sets, and the best-fitting galaxy bias, and lensing calibration bias parameters are largely unchanged from their values when fitting only to the SDSS data. As in the previous section, we can identify the best-fitting combination of σ_8 and Ω_m ,

Table 4. Fits for cosmological parameters using *WMAP7* and our data as described in Section 7.2. In each case, parameters that are fixed to a single value are in bold; those that are fit are shown with 68 per cent confidence limits after marginalizing over all other fitted parameters. The exception to this convention is the sum of neutrino masses, for which the 95 per cent upper limit is shown.

Fit	Data	σ_8	Ω_m	n_s	H_0 (km s ⁻¹ Mpc ⁻¹)	w_{de}	Ω_k	$\sum m_\nu$ (eV)
6	<i>WMAP7</i>	0.810 ± 0.029	$0.270^{+0.030}_{-0.027}$	0.965 ± 0.014	70.4 ± 2.5	-1	0	0
7	<i>WMAP7</i> +our data	0.796 ± 0.019	0.261 ± 0.014	0.966 ± 0.013	71.1 ± 1.5	-1	0	0
8	<i>WMAP7</i>	$0.83^{+0.10}_{-0.11}$	$0.26^{+0.10}_{-0.07}$	0.969 ± 0.014	72 ± 11	$-1.05^{+0.33}_{-0.30}$	0	0
9	<i>WMAP7</i> +our data	0.82 ± 0.08	$0.25^{+0.04}_{-0.03}$	0.968 ± 0.014	73 ± 6	-1.07 ± 0.20	0	0
10	<i>WMAP7</i>	$0.77^{+0.09}_{-0.07}$	$0.42^{+0.21}_{-0.17}$	0.964 ± 0.015	57^{+16}_{-10}	$-0.94^{+0.30}_{-0.34}$	$-0.03^{+0.03}_{-0.05}$	0
11	<i>WMAP7</i> +our data	$0.81^{+0.07}_{-0.08}$	$0.25^{+0.04}_{-0.03}$	0.969 ± 0.014	72^{+6}_{-5}	$-1.05^{+0.22}_{-0.24}$	0.00 ± 0.01	0
12	<i>WMAP7</i>	$0.72^{+0.07}_{-0.08}$	$0.32^{+0.07}_{-0.05}$	0.961 ± 0.016	66 ± 4	-1	0	<1.1
13	<i>WMAP7</i> +our data	$0.76^{+0.04}_{-0.05}$	$0.28^{+0.03}_{-0.02}$	0.968 ± 0.013	69 ± 2	-1	0	<0.56

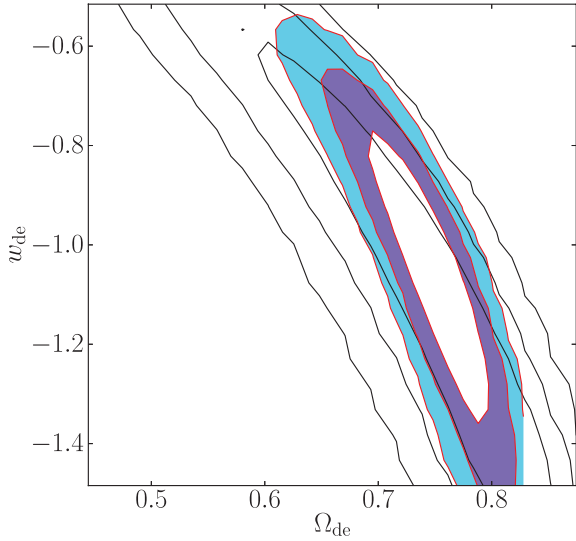


Figure 17. 2D contour plot for flat w CDM fits with the equation of state of dark energy allowed to vary from our fiducial value of -1 (but assumed to be constant in time). Line and contour styles are as in Fig. 15.

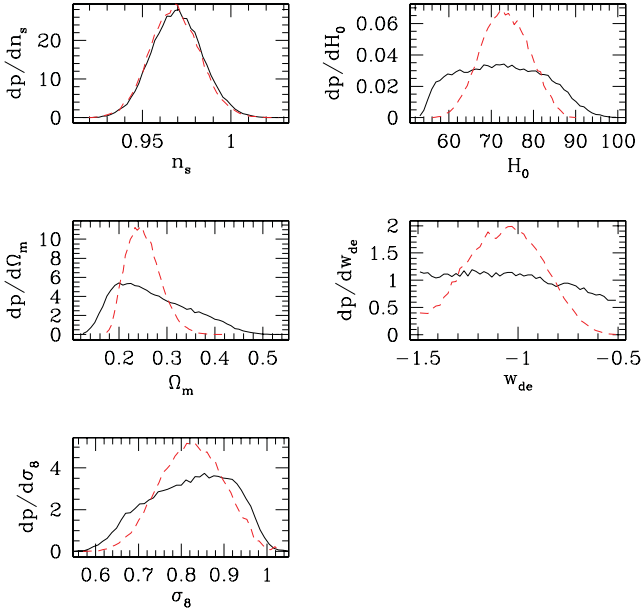


Figure 18. 1D probability distributions for flat w CDM fits with the equation of state of dark energy allowed to vary from our fiducial value of -1 (but assumed to be constant in time), as in Fig. 17. Line styles are as in Fig. 16.

which has changed from $\sigma_8(\Omega_m/0.25)^{0.57} = 0.80 \pm 0.05$ (our data alone) to $\sigma_8(\Omega_m/0.25)^{-0.13} = 0.79 \pm 0.02$ (*WMAP7* + our data)

Next, we allow the equation of state of dark energy (w_{de}) to vary from a cosmological constant. Figs 17 and 18 show 2D contours and 1D parameter distributions, respectively, and Table 4 gives best-fitting parameter constraints, again with *WMAP7* alone (fit 8) and with our data included (fit 9). As in the Λ CDM case, our data do not provide significant additional constraining power on n_s , but it does improve the constraints on all the other parameters, most dramatically on w_{de} (because adding our data provides a constraint on the amplitude of matter fluctuations at times well after dark energy has become important).

Next, we relax the assumption of flatness (while still allowing the equation of state of dark energy to vary from a cosmological

constant). Figs 19 and 20 show 2D and 1D constraints, respectively, and Table 4 gives best-fitting parameter constraints, again with *WMAP7* alone (fit 10) and with our data included (fit 11). We can see that with these relaxed assumptions about w_{de} and Ω_k , the posterior probability distributions for Ω_m , H_0 and w_{de} are very broad; our data play a crucial role in reducing the allowed region of parameter space for all parameters except n_s .

Finally, we revert to the assumption of flat Λ CDM, but we allow for the presence of massive neutrinos using the formalism in Section 2.3. Fig. 21 shows 1D posterior probability distributions and Table 4 gives best-fitting parameter constraints, again with *WMAP7* alone (fit 12) and with our data included (fit 13). In addition to tightening constraints on σ_8 , Ω_m and H_0 as before, our data help to rule out models with neutrino masses on the higher end of those allowed by *WMAP7*, such that the one-sided 95 per cent upper limit on neutrino mass goes down from 1.1 eV with *WMAP7* alone to 0.56 eV with *WMAP7* and our data. In general, the presence of massive neutrinos can significantly broaden the allowed parameter space for Ω_m and H_0 from CMB alone, and our data rule out some of the allowed high- Ω_m or low- H_0 values.

7.3 Comparison with previous work

The results of the previous section illustrate that our data provide cosmological parameter constraints that are consistent with and complementary to those from *WMAP7*. Here, we compare our constraints with those from other cosmological probes.

We do not compare our results against those from a pure clustering analysis of the shape and amplitude of the galaxy power spectrum, due to systematic uncertainties in treatments of non-linear galaxy bias, RSD and other issues. However, it is valuable to compare against measurements of BAO, a measure of the expansion history of the universe rather than the growth of structure, since it is significantly less prone to such uncertainties. The most recent measurement of BAO in the SDSS DR7 (Mehta et al. 2012; Padmanabhan et al. 2012; Xu et al. 2012) represents the first use of the ‘reconstruction’ technique (Eisenstein et al. 2007) to reduce the effects of non-linear evolution of the density field in smoothing the BAO peak. Mehta et al. (2012) demonstrates that when combining the BAO peak position with CMB data, they find $\Omega_m = 0.280 \pm 0.014$ (in the context of flat Λ CDM). This result is fully consistent with our data when fitting for σ_8 and Ω_m , which yielded $\Omega_m = 0.257^{+0.038}_{-0.034}$ (Section 7.1). This consistency is non-trivial, given that the BAO results use an identical sample to make a fully geometric constraint on cosmology, whereas we measure the amplitude of clustering well below the BAO peak.

We can also compare against the BAO results from the Baryon Oscillation Spectroscopic Survey presented in Anderson et al. (2012). Assuming flat Λ CDM, when using *WMAP7* and the BAO results for two galaxy samples, they find $\Omega_m = 0.293 \pm 0.012$ and $H_0 = 68.8 \pm 1.0 \text{ km s}^{-1} \text{ Mpc}^{-1}$. We compare this with our fit 7 (combining our data with *WMAP7*), which gave $\Omega_m = 0.261 \pm 0.014$ and $H_0 = 71.1 \pm 1.5 \text{ km s}^{-1}$. A naive comparison of the results – neglecting the fact that both measurements include *WMAP7* – suggests a 1.7σ and 1.3σ discrepancy for Ω_m and H_0 , respectively. While these are not very significant, the tension is in fact worse since a significant part of the constraining power comes from the CMB data, which is the same for both measurements. We defer exploration of this possible tension between the BAO and our lensing constraints to future work; however, we note that fit 13 suggests that including the effects of massive neutrinos would help to reduce this tension. We also compare our results against those from other

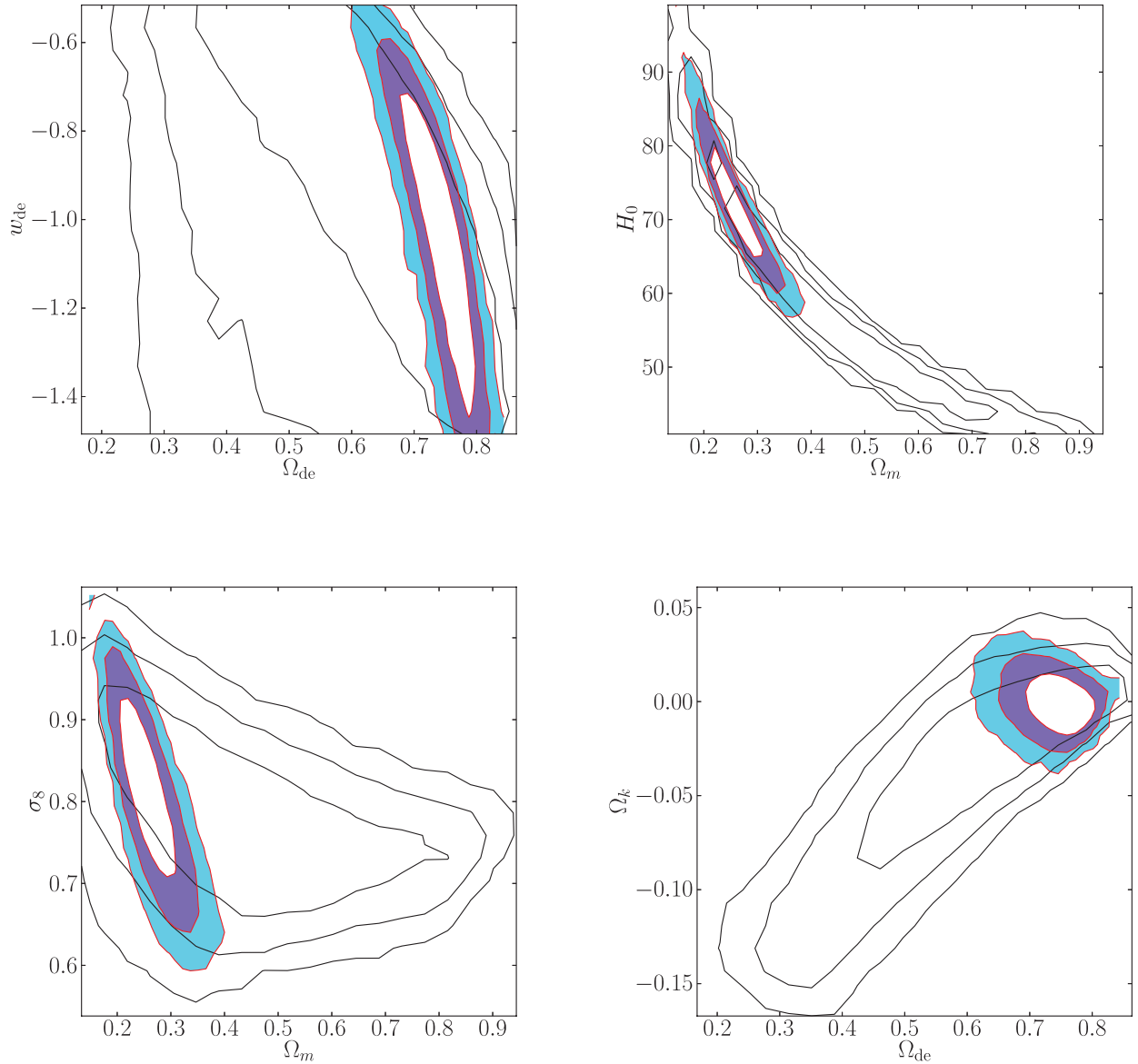


Figure 19. 2D contour plot for w CDM fits without the assumption of flatness. Line and contour styles are as in Fig. 15.

lensing analyses, particularly cosmic shear. First, we compare against those from the COSMOS survey, including the original analysis from Massey et al. (2007) and a re-analysis in Schrabback et al. (2010). The results from Massey et al. (2007) used a 3D analysis to infer $\sigma_8(\Omega_m/0.3)^{0.44} = 0.866^{+0.085}_{-0.068}$ (68 per cent CL, stat. + sys.). We can compare this result against our result when fitting for σ_8 and Ω_m , $\sigma_8(\Omega_m/0.25)^{0.57} = 0.80 \pm 0.05$ marginalized over nuisance parameters. The COSMOS results are $\sim 1.6\sigma$ above ours, giving a higher amplitude of clustering. The 3D COSMOS lensing analysis in Schrabback et al. (2010) gives, for flat Λ CDM, a value $\sigma_8(\Omega_m/0.3)^{0.51} = 0.75 \pm 0.08$, consistent with our results at the $\sim 0.2\sigma$ level. Part of the reason for the lower quoted clustering amplitude in Schrabback et al. (2010) is a different treatment of the non-linear power spectrum (more consistent with ours): if they use the same treatment as Massey et al. (2007), they find 0.79 ± 0.09 , higher by 5 per cent. Other differences in clustering amplitude between the two COSMOS results could come from the different treatment of PSF estimation, charge-transfer inefficiency, the availability of more photometric data to improve the photometric

redshifts, or differences in analysis methods (scales used and so on). In short, the COSMOS lensing results are consistent with ours, with the exact comparison depending on the method of analysis and the treatment of systematic errors.

We can also compare against cosmic shear results from stripe 82 of the SDSS itself. There are two such results that use largely independent analysis methods on the same data, by Huff et al. (2011) and Lin et al. (2012). The work in Huff et al. (2011) used the same PSF correction technique as we have used, and also the same simulation method relying on space-based training data (Mandelbaum et al. 2012) to calibrate the shape measurements, so its systematic errors may not be fully independent from ours. However, given that the area of stripe 82 is ~ 3 per cent of the area used here, we can consider those results to be statistically independent of ours. With fixed Ω_m close to our value, Huff et al. (2011) find a relatively low amplitude of matter fluctuations, $\sigma_8 = 0.636^{+0.109}_{-0.154}$, which can be compared with our 0.80 ± 0.05 . Assuming completely independent errors, this represents a 1.4σ discrepancy, which is not statistically significant mainly due to the small size of stripe 82 and the limited

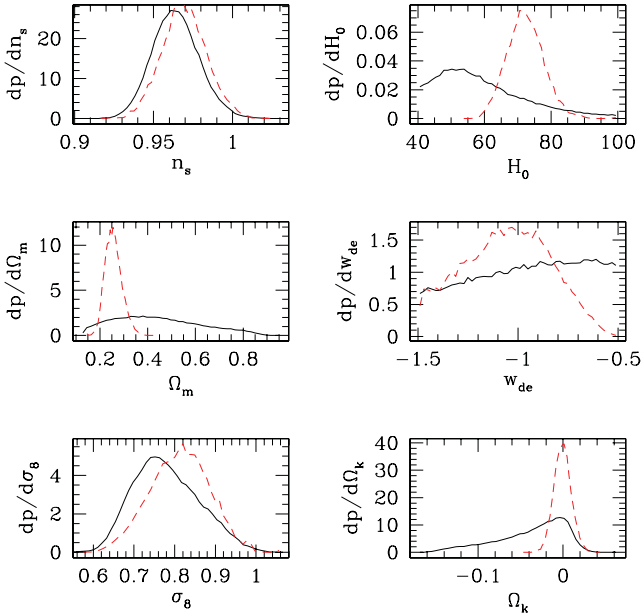


Figure 20. 1D probability distributions for w CDM fits without the assumption of flatness, as in Fig. 19. Line styles are as in Fig. 16.

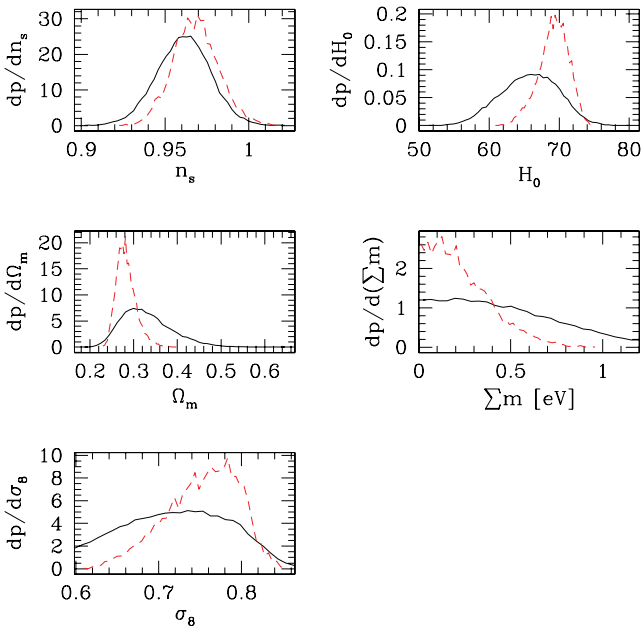


Figure 21. 1D probability distributions for flat Λ CDM fits with massive neutrinos. Line styles are as in Fig. 16.

source number density due to the SDSS seeing. Comparing with Lin et al. (2012), they find for flat Λ CDM that $\sigma_8 \Omega_m^{0.7} = 0.252_{-0.052}^{+0.032}$. For our value of $\Omega_m = 0.25$, that constraint becomes $\sigma_8 = 0.665_{-0.137}^{+0.084}$, quite similar to that from Huff et al. (2011). In both cases, we therefore see a slight tension with our results, but only at the $\sim 1.4\sigma$ level.

We also compare against the most recent cosmic shear results from the Canada–France–Hawaii Telescope Legacy Survey, presented in Heymans et al. (2013). The sample in this analysis covers 154 deg^2 and has a median redshift of $z_{\text{med}} = 0.70$. After computing tomographic cosmic shear signals and marginalizing over a model for intrinsic alignments, they find a best-constrained pa-

rameter combination of $\sigma_8(\Omega_m/0.27)^{0.46 \pm 0.02} = 0.774_{-0.041}^{+0.032}$ before combining with any external data sets. This result is completely consistent with our findings of $\sigma_8(\Omega_m/0.25)^{0.57} = 0.80 \pm 0.05$.

Finally, we compare our results with those from analyses that used small-scale lensing and clustering measurements, despite our caveats from Section 2. First, Cacciato et al. (2013) carried out a joint lensing and clustering analysis of SDSS ‘Main’ sample galaxies to constrain cosmology. They employed the alternate approach, discussed briefly in Section 2, of using the measurements to small scales, which requires use of an HOD model for how galaxies populate dark matter haloes in order to interpret the measurements. Despite the use of SDSS data, that measurement is somewhat independent of this one because it (a) uses a subset of the area and (b) employs smaller scales than this one. Their results for the flat Λ CDM model with *WMAP7* priors on n_s , h and Ω_b are consistent with ours, $\Omega_m = 0.278_{-0.026}^{+0.023}$ and $\sigma_8 = 0.763_{-0.049}^{+0.064}$ (95 per cent CL). Secondly, we compare with the results from Tinker et al. (2012), who used the mass versus richness calibration based on weak lensing, and the galaxy clustering (using an HOD). These measurements should be somewhat but not highly correlated with ours, because of the different range of scales used. For their combination of observables and modelling method, they find $\sigma_8 \Omega_m^{0.5} = 0.465 \pm 0.026$, or $\sigma_8(\Omega_m/0.25)^{0.5} = 0.93 \pm 0.05$ (1σ). Compared with our result of $\sigma_8(\Omega_m/0.25)^{0.57} = 0.80 \pm 0.05$, there is clearly some tension, since the discrepancy is 2.5σ assuming independent errors, and in fact there should be some correlation between the results. Understanding the exact source of this tension is beyond the scope of this work, but likely it lies in the different assumptions behind the methods. We also note that when combining with CMB data, they find $\Omega_m = 0.290 \pm 0.016$ and $\sigma_8 = 0.826 \pm 0.020$, which should be compared with our flat Λ CDM results of $\Omega_m = 0.270_{-0.027}^{+0.030}$ and $\sigma_8 = 0.810 \pm 0.029$. Here, the tension is less evident, presumably because of the combination with identical CMB data.

8 DISCUSSION

We have used updated measurements of galaxy–galaxy weak lensing and galaxy clustering for several samples of spectroscopic galaxies in the SDSS DR7 to place competitive constraints on the amplitude of matter fluctuations and, by combining with *WMAP7* data, the growth of structure with time. The novelty in comparison with previous lensing cosmology constraints is that we have used galaxy–galaxy lensing (a cross-correlation of lens galaxy positions and the background shear field) rather than cosmic shear (the autocorrelation of the shear field). From a statistical perspective, the former is more detectable in low-redshift surveys such as SDSS; however, even at higher redshift, the galaxy–galaxy lensing typically has a lower systematic error budget, because the use of cross-correlations allows us to more easily remove several systematic errors (intrinsic alignments, additive shear systematics) that plague cosmic shear. To avoid contamination from the smallest scales, where there are uncertainties in the galaxy-mass cross-correlation due to the way that galaxies populate haloes, we have used the ADSD statistic Υ , which strictly removes contributions below some scale R_0 (chosen based on comparison with simulations to be $4h^{-1} \text{ Mpc}$ for the clustering analysis, and $2h^{-1} \text{ Mpc}$ for the lensing analysis). We apply this approach to three different non-overlapping samples extracted from SDSS DR7: an intermediate-redshift ($0.16 < z < 0.36$) LRG sample, high-redshift ($0.36 < z < 0.47$) LRG sample and a low-redshift sample ($z < 0.155$) with a fainter absolute magnitude limit and no colour selection. We have opted to model the signals

using the non-linear matter power spectrum along with a perturbation theory-based model for the non-linear galaxy bias, containing parameters over which we marginalize. We see clear evidence for a scale-dependent bias in our LRG sample with large-scale bias around 2, while there is no evidence for the scale-dependent bias for the lower luminosity sample with large-scale bias around 1.25. This trend is consistent with theoretical expectations based on simulations and analytic predictions (Baldauf et al. 2012).

Using our data and fixing all cosmological parameters except for σ_8 and Ω_m , we find $\sigma_8(\Omega_m/0.25)^{0.57} = 0.80 \pm 0.05$ (1σ , stat. + sys.) after marginalizing over the galaxy bias parameters and a nuisance parameter for the lensing calibration. This result is highly consistent with that from the *WMAP7* CMB analysis, and with many other cosmological measurements as discussed in Section 7.3. The 6 per cent error bar, including both statistical and systematic contributions, indicates that the SDSS is a quite powerful survey for weak lensing cosmology at low redshift (in the context of other extant lensing data sets). Moreover, given its low effective redshift of ~ 0.27 , we imagine future benefits from the combination with other lensing measurements that typically have higher effective redshifts.

When we include *WMAP7* data in the analysis, we find that for flat Λ CDM, we are able to provide significant additional constraining power on σ_8 , Ω_m and H_0 due to orthogonal degeneracy directions, effectively halving the allowed region in parameter space; we do not provide significant additional constraining power on n_s . When we allow the equation of state of dark energy w_{de} to vary from -1 (while still assuming it is constant in time), when we further allow the possibility of curvature, or when we include massive neutrinos in the context of flat Λ CDM, we likewise find that our low-redshift constraint on the amplitude of matter fluctuations is crucial for reducing major parameter degeneracies. It will be interesting to combine these results with a low-redshift constraint on the expansion history of the universe, such as from BAO; we defer this exercise to future work, but note that Section 7.3 suggests that inclusion of massive neutrinos may be necessary to reduce some tension between constraints on Ω_m and H_0 from the two probes.

We emphasize that these results represent an entirely new opportunity for the field of lensing to constrain cosmological parameters in a way that is largely independent of the details of how galaxies populate dark matter haloes, but also less sensitive than cosmic shear to several important observational and astrophysical systematic errors. Among these are all additive contributions such as telescope or atmosphere effects that induce shear–shear correlations but not shear–galaxy correlations. Intrinsic alignments also do not contribute to shear–galaxy correlations as long as the redshift separation between lenses and sources, using photometric redshift information, is effective. In contrast, the dominant intrinsic alignment contribution to shear–shear correlations, induced by correlations between sheared galaxies in the background and intrinsically aligned galaxies in the foreground, cannot be eliminated simply by using photometric redshift information (Hirata & Seljak 2004).

In addition to the intrinsic value of these cosmological constraints in and of themselves, this work is a proof of concept for this analysis technique for the next generation of large, wide-field surveys that will carry out lensing measurements, such as Hyper Suprime-Cam¹⁸ (Miyazaki et al. 2006), Dark Energy Survey¹⁹ (The Dark Energy Survey Collaboration 2005), the Kilo-Degree Survey²⁰,

the Panoramic Survey Telescope and Rapid Response System²¹ (Kaiser et al. 2010) and even more ambitious programmes such as the Large Synoptic Survey Telescope²² (LSST Science Collaborations et al. 2009), Euclid²³ and the Wide-Field Infrared Survey Telescope²⁴. The ability to make cosmological measurements with galaxy–galaxy lensing rather than cosmic shear is particularly important for making use of early data from upcoming surveys, when additive shear systematics will be less well-understood. We expect that this approach will yield results that are competitive and complementary to shear–shear analysis for these future surveys as well.

The data used for the cosmological parameter constraints, and the MCMC chains, can be downloaded directly from the first author’s website.

ACKNOWLEDGEMENTS

We thank the anonymous referee for providing numerous comments that improved the presentation of this work. We thank Jim Gunn, Robert Lupton, Benjamin Joachimi and David Spergel for useful discussions related to this work, and we also thank Eyal Kazin for helpful discussions on selection of the LRG sample. RM was supported for part of the duration of this project by the US Department of Energy Early Career Program. During this project, US was supported in part by the US Department of Energy under Contract No. DE-AC02-98CH10886, the Swiss National Foundation under contract 200021-116696/1 and the WCU grant R32-10130. During this project, CH has been supported by the US Department of Energy (DOE-FG03-92-ER40701 and DOE-DE-SC0006624), the National Science Foundation (NST AST-0807337) and the David & Lucile Packard Foundation. RES acknowledges support from a Marie Curie Reintegration Grant and an award for Experienced Researchers from the Alexander von Humboldt Foundation. We thank V. Springel for making public GADGET-2 and for providing his B-FoF halo finder, and R. Scoccimarro for making public his 2LPT code.

Funding for the SDSS and SDSS-II has been provided by the Alfred P. Sloan Foundation, the Participating Institutions, the National Science Foundation, the US Department of Energy, the National Aeronautics and Space Administration, the Japanese Monbukagakusho, and the Max Planck Society and the Higher Education Funding Council for England. The SDSS website is <http://www.sdss.org/>.

The SDSS is managed by the Astrophysical Research Consortium (ARC) for the Participating Institutions. The Participating Institutions are the American Museum of Natural History, Astrophysical Institute Potsdam, University of Basel, University of Cambridge, Case Western Reserve University, The University of Chicago, Drexel University, Fermilab, the Institute for Advanced Study, the Japan Participation Group, The Johns Hopkins University, the Joint Institute for Nuclear Astrophysics, the Kavli Institute for Particle Astrophysics and Cosmology, the Korean Scientist Group, the Chinese Academy of Sciences (LAMOST), Los Alamos National Laboratory, the Max-Planck-Institute for Astronomy (MPIA), the Max-Planck-Institute for Astrophysics (MPA), New Mexico State University, Ohio State University, University of Pittsburgh, University of Portsmouth, Princeton University,

¹⁸ <http://www.naoj.org/Projects/HSC/index.html>

¹⁹ <https://www.darkenergysurvey.org/>

²⁰ <https://www.astro-wise.org/projects/KIDS/>

²¹ <http://pan-starrs.ifa.hawaii.edu/public/>

²² <http://www.lsst.org/lsst>

²³ <http://sci.esa.int/science-e/www/area/index.cfm?fareaid=102>

²⁴ <http://wfirst.gsfc.nasa.gov/>

the United States Naval Observatory and the University of Washington.

REFERENCES

- Abazjany K. et al., 2009, *ApJS*, 182, 543
 Aihara H. et al., 2011, *ApJS*, 193, 29
 Albrecht A. et al., 2006, preprint (astro-ph/0609591)
 Anderson L. et al., 2012, *MNRAS*, 427, 3435
 Bacon D. J., Refregier A. R., Ellis R. S., 2000, *MNRAS*, 318, 625
 Baldauf T., Smith R. E., Seljak U., Mandelbaum R., 2010, *Phys. Rev. D*, 81, 063531
 Baldauf T., Seljak U., Desjacques V., McDonald P., 2012, *Phys. Rev. D*, 86, 083540
 Bartelmann M., Schneider P., 2001, *Phys. Rep.*, 340, 291
 Bernardeau F., Colombi S., Gaztanaga E., Scoccimarro R., 2002, *Phys. Rep.*, 367, 1
 Bernstein G. M., Jarvis M., 2002, *AJ*, 123, 583
 Bird S., Viel M., Haehnelt M. G., 2012, *MNRAS*, 420, 2551
 Blanton M. R., Roweis S., 2007, *AJ*, 133, 734
 Blanton M. R. et al., 2001, *AJ*, 121, 2358
 Blanton M. R. et al., 2005, *AJ*, 129, 2562
 Blazek J., Mandelbaum R., Seljak U., Nakajima R., 2012, *J. Cosmol. Astropart. Phys.*, 5, 41
 Bridle S. et al., 2010, *MNRAS*, 405, 2044
 Cacciato M., van den Bosch F. C., More S., Li R., Mo H. J., Yang X., 2009, *MNRAS*, 394, 929
 Cacciato M., Lahav O., van den Bosch F. C., Hoekstra H., Dekel A., 2012, *MNRAS*, 426, 566
 Cacciato M., van den Bosch F. C., More S., Mo H., Yang X., 2013, *MNRAS*, 430, 767
 Chan K. C., Scoccimarro R., Sheth R. K., 2012, *Phys. Rev. D*, 85, 083509
 Cole S. et al., 2005, *MNRAS*, 362, 505
 Davis M., Efstathiou G., Frenk C. S., White S. D. M., 1985, *ApJ*, 292, 371
 Dekel A., Lahav O., 1999, *ApJ*, 520, 24
 Eisenstein D. et al., 2001, *AJ*, 122, 2267
 Eisenstein D. J., Seo H.-J., Sirko E., Spergel D. N., 2007, *ApJ*, 664, 675
 Feldmann R. et al., 2006, *MNRAS*, 372, 565
 Fry J. N., Gaztanaga E., 1993, *ApJ*, 413, 447
 Fukugita M., Ichikawa T., Gunn J., Doi M., Shimasaku K., Schneider D., 1996, *AJ*, 111, 1748
 Gao L., White S. D. M., 2007, *MNRAS*, 377, L5
 Gao L., Springel V., White S. D. M., 2005, *MNRAS*, 363, L66
 Gunn J. et al., 1998, *AJ*, 116, 3040
 Hartlap J., Simon P., Schneider P., 2007, *A&A*, 464, 399
 Heitmann K., White M., Wagner C., Habib S., Higdon D., 2010, *ApJ*, 715, 104
 Heymans C. et al., 2013, preprint (arXiv:1303.1808H)
 Hirata C., Seljak U., 2003, *MNRAS*, 343, 459
 Hirata C. M., Seljak U., 2004, *Phys. Rev. D*, 70, 063526
 Hirata C. M. et al., 2004, *MNRAS*, 353, 529
 Hirata C. M., Mandelbaum R., Ishak M., Seljak U., Nichol R., Pimbblet K. A., Ross N. P., Wake D., 2007, *MNRAS*, 381, 1197
 Hoekstra H., Jain B., 2008, *Ann. Rev. Nucl. Part. Sci.*, 58, 99
 Hoekstra H., Yee H. K. C., Gladders M. D., Barrientos L. F., Hall P. B., Infante L., 2002, *ApJ*, 572, 55
 Hogg D. W., Finkbeiner D. P., Schlegel D. J., Gunn J. E., 2001, *AJ*, 122, 2129
 Huff E. M., Eifler T., Hirata C. M., Mandelbaum R., Schlegel D., Seljak U., 2011, preprint (arXiv:1112.3143)
 Høg E. et al., 2000, *A&A*, 355, L27
 Ivezić Ž. et al., 2004, *Astron. Nachr.*, 325, 583
 Jeong D., Komatsu E., Jain B., 2009, *Phys. Rev. D*, 80, 123527
 Jing Y. P., Zhang P., Lin W. P., Gao L., Springel V., 2006, *ApJ*, 640, L119
 Jullo E. et al., 2012, *ApJ*, 750, 37
 Kaiser N., 1987, *MNRAS*, 227, 1
 Kaiser N., Squires G., Broadhurst T., 1995, *ApJ*, 449, 460
 Kaiser N. et al., 2010, in Stepp L. M., Gilmozzi R. H. J., Hall H. J., eds, *Proc. SPIE Conf. Ser. Vol. 7733, Ground-based and Airborne Telescopes III*. SPIE, Bellingham, A77330E
 Kazin E. A. et al., 2010, *ApJ*, 710, 1444
 Kitching T. D. et al., 2012, *MNRAS*, 423, 3163
 Komatsu E. et al., 2011, *ApJS*, 192, 18
 Landy S. D., Szalay A. S., 1993, *ApJ*, 412, 64
 Lawrence E., Heitmann K., White M., Higdon D., Wagner C., Habib S., Williams B., 2010, *ApJ*, 713, 1322
 Leauthaud A., Tinker J., Behroozi P. S., Busha M. T., Wechsler R. H., 2011, *ApJ*, 738, 45
 Leauthaud A. et al., 2012, *ApJ*, 744, 159
 Lewis A., Bridle S., 2002, *Phys. Rev. D*, 66, 103511
 Lewis A., Challinor A., Lasenby A., 2000, *ApJ*, 538, 473
 Lin H. et al., 2012, *ApJ*, 761, 15
 LSST Science Collaborations and LSST Project, 2009, *LSST Science Book*, version 2.0, preprint (arXiv:0912.0201), available at: <http://www.lsst.org/lsst/scibook>
 Lupton R. H., Gunn J. E., Ivezić Z., Knapp G. R., Kent S., Yasuda N., 2001, in Harnden F. R., Jr., Primini F. A., Payne H. E., eds, *ASP Conf. Ser. Vol. 238, The SDSS Imaging Pipelines*. Astron. Soc. Pac., San Francisco, p. 269
 Mandelbaum R., Seljak U., Kauffmann G., Hirata C. M., Brinkmann J., 2006a, *MNRAS*, 368, 715
 Mandelbaum R., Seljak U., Cool R. J., Blanton M., Hirata C. M., Brinkmann J., 2006b, *MNRAS*, 372, 758
 Mandelbaum R., Seljak U., Baldauf T., Smith R. E., 2010, *MNRAS*, 405, 2078
 Mandelbaum R., Hirata C. M., Leauthaud A., Massey R. J., Rhodes J., 2012, *MNRAS*, 420, 1518
 Mandelbaum R. et al., 2005, *MNRAS*, 361, 1287
 Marín F., 2011, *ApJ*, 737, 97
 Massey R. et al., 2007, *ApJS*, 172, 239
 Massey R., Kitching T., Richard J., 2010, *Rep. Prog. Phys.*, 73, 086901
 McCarthy I. G., Schaye J., Bower G., Ponman T. J., Booth C. M., Dalla Vecchia C., Springel V., 2011, *MNRAS*, 412, 1965
 Mehta K. T., Cuesta A. J., Xu X., Eisenstein D. J., Padmanabhan N., 2012, *MNRAS*, 427, 2168
 Miyazaki S. et al., 2006, in McLean I. S., Iye M., eds, *Proc. SPIE Conf. Ser. Vol. 6269, Ground-based and Airborne Instrumentation for Astronomy*. SPIE, Bellingham, p. 62690B
 More S., van den Bosch F., Cacciato M., More A., Mo H., Yang X., 2013, *MNRAS*, 430, 747
 Nakajima R., Mandelbaum R., Seljak U., Cohn J. D., Reyes R., Cool R., 2012, *MNRAS*, 420, 3240 (N12)
 Padmanabhan N., White M., Eisenstein D. J., 2007, *MNRAS*, 376, 1702
 Padmanabhan N. et al., 2008, *ApJ*, 674, 1217
 Padmanabhan N., Xu X., Eisenstein D. J., Scalzo R., Cuesta A. J., Mehta K. T., Kazin E., 2012, *MNRAS*, 427, 2132
 Perlmutter S. et al., 1999, *ApJ*, 517, 565
 Petrosian V., 1976, *ApJ*, 209, L1
 Pier J. R., Munn J. A., Hindsley R. B., Hennessy G. S., Kent S. M., Lupton R. H., Ivezić Ž., 2003, *AJ*, 125, 1559
 Refregier A., 2003, *ARA&A*, 41, 645
 Reid B. A., Spergel D. N., 2009, *ApJ*, 698, 143
 Reid B. A., White M., 2011, *MNRAS*, 417, 1913
 Reyes R., Mandelbaum R., Seljak U., Baldauf T., Gunn J. E., Lombriser L., Smith R. E., 2010, *Nat*, 464, 256
 Reyes R., Mandelbaum R., Gunn J. E., Nakajima R., Seljak U., Hirata C. M., 2012, *MNRAS*, 425, 2610 (R12)
 Rhodes J., Refregier A., Groth E. J., 2001, *ApJ*, 552, L85
 Richards G. et al., 2002, *AJ*, 123, 2945
 Riess A. G. et al., 1998, *AJ*, 116, 1009
 Rudd D. H., Zentner A. R., Kravtsov A. V., 2008, *ApJ*, 672, 19
 Sánchez A. G., Cole S., 2008, *MNRAS*, 385, 830
 Schlegel D. J., Finkbeiner D. P., Davis M., 1998, *ApJ*, 500, 525
 Schneider P., van Waerbeke L., Jain B., Kruse G., 1998, *MNRAS*, 296, 873
 Schrabback T. et al., 2010, *A&A*, 516, A63

- Scoccimarro R., 1998, MNRAS, 299, 1097
 Seljak U. et al., 2005, Phys. Rev. D, 71, 043511
 Semboloni E., Hoekstra H., Schaye J., van Daalen M. P., McCarthy I. G., 2011, MNRAS, 417, 2020
 Simon P., Hettterscheidt M., Wolf C., Meisenheimer K., Hildebrandt H., Schneider P., Schirmer M., Erben T., 2009, MNRAS, 398, 807
 Smith R. E., 2009, MNRAS, 400, 851
 Smith J. et al., 2002, AJ, 123, 2121
 Smith R. E., Scoccimarro R., Sheth R. K., 2007, Phys. Rev. D, 75, 063512
 Smith R. E., Hernández-Monteagudo C., Seljak U., 2009, Phys. Rev. D, 80, 063528
 Spergel D. N. et al., 2003, ApJS, 148, 175
 Spergel D. N. et al., 2007, ApJS, 170, 377
 Springel V., 2005, MNRAS, 364, 1105
 Stoughton C. et al., 2002, AJ, 123, 485
 Strauss M. et al., 2002, AJ, 124, 1810
 Swanson M. E. C., Tegmark M., Blanton M., Zehavi I., 2008, MNRAS, 385, 1635
 The Dark Energy Survey Collaboration 2005, preprint (astro-ph/0510346)
 Tinker J. L., Weinberg D. H., Zheng Z., Zehavi I., 2005, ApJ, 631, 41
 Tinker J. L. et al., 2012, ApJ, 745, 16
 Tucker D. et al., 2006, Astron. Nachr., 327, 821
 van Daalen M. P., Schaye J., Booth C. M., Dalla Vecchia C., 2011, MNRAS, 415, 3649
 van den Bosch F., More S., Cacciato M., Mo H., Yang X., 2013, MNRAS, 430, 725
 Van Waerbeke L. et al., 2000, A&A, 358, 30
 Xu X., Padmanabhan N., Eisenstein D. J., Mehta K. T., Cuesta A. J., 2012, MNRAS, 427, 2146
 Yasuda N. et al., 2001, AJ, 122, 1104
 Yoo J., Tinker J. L., Weinberg D. H., Zheng Z., Katz N., Davé R., 2006, ApJ, 652, 26
 York D. et al., 2000, AJ, 120, 1579
 Zehavi I. et al., 2005, ApJ, 621, 22
 Zentner A. R., Rudd D. H., Hu W., 2008, Phys. Rev. D, 77, 043507
 Zhan H., Knox L., 2004, ApJ, 616, L75

APPENDIX A: CALIBRATION OF THE METHOD

As a basic test, we use the data from the simulated LRG sample (Section 2.1) and check whether we can accurately recover the input cosmology using the analysis framework from Section 2.3. Such tests with various R_0 will allow us to determine the safest choice of R_0 to minimize systematic error without excessively increasing the statistical errors.

For this test, we fixed all cosmological parameters besides σ_8 , and varied R_0 , making sure that we can recover the true $\sigma_8 = 0.8$ for the simulations.²⁵ While doing this test, we allowed the lensing calibration and the bias parameters to be free parameters. Given that moving R_0 above $2 h^{-1}$ Mpc for the galaxy–galaxy lensing severely impacts the S/N, we consider only this value of R_0 for the lensing, but vary R_0 for the clustering from 2 to $6 h^{-1}$ Mpc, in steps of $2 h^{-1}$ Mpc. This procedure is also theoretically motivated since, as pointed out in Section 2.4, the clustering signal should be more strongly sensitive than the g–g lensing signal to the details of how galaxies occupy dark matter haloes on these scales. Shape noise was not added to the simulated LRG data, and the simulation volume is 40 times larger than the cosmological volume covered by the real

²⁵ We could have fit jointly for σ_8 and Ω_m . However, since those two cosmological parameters are strongly degenerate, we could easily (due to very small noise fluctuations in the simulations) be driven anywhere along that degeneracy, without it being a meaningful deviation. We therefore check that with Ω_m fixed we can infer the correct σ_8 , under the assumption that this shows we can infer the proper degenerate combination of Ω_m and σ_8 .

data. Thus, the cosmic variance is substantially smaller than that in the real data, and in any case, our dominant source of noise (shape noise) is not present. Because of this, we can trust the simulations to reveal low-level biases due to our fitting procedure, at the level of $\sim 0.2\sigma$ (where σ is the statistical uncertainty in the cosmological parameters in the fits to real data). For $R_{0,gg} = 2, 4, 6 h^{-1}$ Mpc, the best-fitting $\sigma_8 = 0.763, 0.795, 0.792$ (these are the global best-fitting values, not marginalized over nuisance parameters). The first value, for $R_{0,gg} = 2 h^{-1}$ Mpc, indicates a statistically significant bias in σ_8 . However, the results for larger R_0 are consistent with no bias, so we adopt $R_0 = 2$ and $4 h^{-1}$ Mpc for the g–g lensing and galaxy clustering, respectively. The fact that the most likely point agrees with the theory means that there is no inherent bias in the theory predictions with respect to our simulations.

We can also check the effect of priors and marginalization over lensing calibration bias and galaxy bias parameters. After marginalization over the galaxy bias parameters and the lensing calibration, the median of the likelihood is 0.78, which differs from the input value and the global best-fitting value of 0.8. Since our best-fitting model (maximum likelihood) is at the position of the input model, the discrepancy between the median and the input value must be due to the effect of the priors and the marginalization process. The median is the standard value quoted in the MCMC analyses, since it can be robustly estimated. It is also invariant under a monotonic transformation of the variable, i.e. the median of σ_8 is the same as the median of σ_8^2 assuming the same prior, which is believed to be useful since there is no good reason a priori to use the linear fluctuation amplitude σ_8 as opposed to the correlation function amplitude σ_8^2 . However, this does not mean that the median is invariant under the change of the prior, i.e. if we start with a uniform prior on σ_8 we obtain a different median than if we use a uniform prior on σ_8^2 . The only number that is prior independent is the maximum likelihood value, which is unstable in multidimensional MCMC analyses, since the likelihood surface is shallow and MCMC has difficulties finding the absolute maximum with a finite number of steps. It is nevertheless convenient that the main reported number agrees with the input value in simulations. Since a prior that is uniform in σ_8 does not result in this property, and since there is nothing especially natural about that choice of the prior, we will empirically choose a prior such that the median σ_8 agrees with the input value in simulations, and then report the median determined in a similar way in the data. If we apply a flat prior on σ_8^5 , the median increases to $\sigma_8 = 0.80$, and since this agrees with the input value we adopt this prior for the rest of the paper.²⁶ Note that as we add more data, such as additional SDSS data sets (we use three samples, not just LRGs as in the tests in this section) and *WMAP*, the effect of the prior is diminished and we converge on the true value. This is the reason to apply a prior, rather than a correction factor such as $0.80/0.78$, which would have an excessive impact in the case where we add more data.

The plots of simulated Υ are shown in Fig. 2, and we see that the simulated data and the best model agree reasonably well both for galaxy–galaxy lensing and galaxy clustering, with $b_2 = 0.25$ as the best-fitting value.

We also note that in the real data, when carrying out the fitting procedure, we see a qualitatively similar trend in $\sigma_8(R_{0,gg})$

²⁶ For those who wish to make cosmological parameter constraints using these data while exploring different choices of the prior, the MCMC chains and the data used for the fits can be downloaded directly from the first author’s website.

increasing with R_0 ; however, the change in σ_8 is larger in amplitude (but consistent with that given here within the errors). As a final sanity check of our procedure above, we carry out the analysis using another HOD sample, constructed from simulations with $\sigma_8 = 0.90$ and selected to mimic a higher luminosity and higher mass sample. For this HOD sample, with our adopted values of R_0 for g-g lensing and galaxy clustering and our prior on σ_8 , we find best-fitting and median $\sigma_8 = 0.90$ and 0.92 . The former number is completely consistent with the input cosmological model, reassuring us that our choice of R_0 is robust to significant changes in the galaxy mass and input cosmology. The latter number suggests that for large values of σ_8 , the adopted prior will cause a bias that is ~ 40 per cent of our statistical errors. However, we see no evidence for such a high σ_8 , and so this worst-case scenario is not an issue in practice.

APPENDIX B: WEAK LENSING SYSTEMATICS TESTS

In this Appendix, we present several tests of systematic error in the lensing signals, focusing exclusively on those tests that were not done for the same shape catalogue by R12.

B1 Calculation of Υ_{gm}

Since we use Υ_{gm} for cosmological parameter constraints, and it is a derived quantity that relies on determination of $\Delta\Sigma(R_0)$, here we present tests illustrating the accuracy of that determination.

As stated in Section 4.1, we determine $\Delta\Sigma(R_0)$ using power-law fits over a range of scales on which $\Delta\Sigma$ appears consistent with a power law, including R_0 itself to avoid extrapolation. In Fig. B1, we show (for all three samples) the observed $\Delta\Sigma(R)$ divided by the best-fitting power law for the chosen range of scales which are

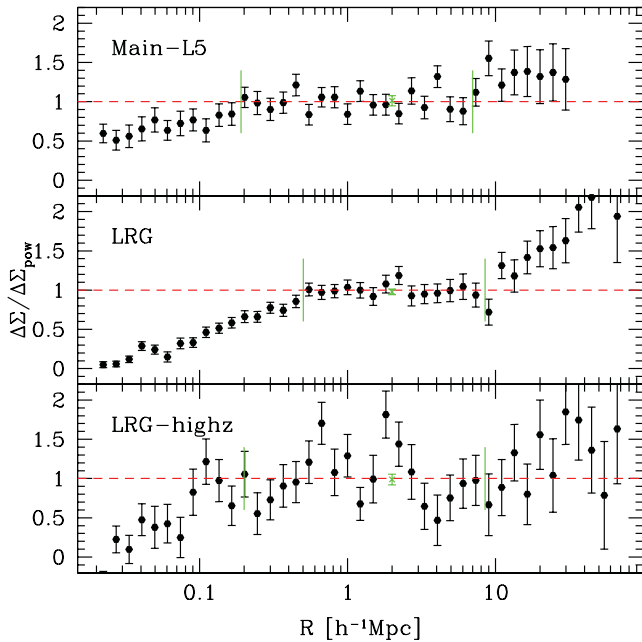


Figure B1. Lensing signals for the three samples (as labelled on the plot) divided by the best-fitting power law using the range of scales indicated by vertical solid lines. The horizontal dashed line shows the ideal value $\Delta\Sigma/\Delta\Sigma_{\text{pow}} = 1$. Also, a single point shown as a \times with its own error bar at $R_0 = 2 h^{-1}$ Mpc shows the jackknife mean value that was used for $\Delta\Sigma(R_0)$, and its jackknife error.

Table B1. Best-fitting power-law functions (as defined in Section B1) to $\Delta\Sigma(R)$ for a limited range of scales, used to estimate $\Delta\Sigma(R_0)$ and therefore Υ_{gm} .

Sample	$R_{\text{pow, min}}$ (h^{-1} Mpc)	$R_{\text{pow, max}}$ (h^{-1} Mpc)	$\Delta\Sigma_0$ ($h M_{\odot} \text{pc}^{-2}$)	α
Main-L5	0.2	7.0	2.49	-0.97
LRG	0.5	8.5	5.81	-1.22
LRG-highz	0.2	8.5	5.41	-1.08

indicated by vertical lines. This power law is determined from a fit to the jackknife mean $\Delta\Sigma$, weighted by the inverse variance (assumed to be diagonal, which is appropriate for these scales). Ideally, this ratio of observed signal to power law would be consistent with one for all scales between the vertical lines. In addition, we show the jackknife mean value of $\Delta\Sigma(R_0)$ and its jackknife error bar, again with respect to the best-fitting power law for the chosen range of scales and therefore with an ideal value of 1. It is clear that the power-law approximation is valid on the range of scales used, but the observed signal deviates from it strongly outside of that range. This power-law fit is used *only* for empirical determination of $\Delta\Sigma(R_0)$, not for any other purpose.

The best-fitting power-laws and ranges of scales used are defined as $\Delta\Sigma = \Delta\Sigma_0(R/R_0)^\alpha$ for $R_{\text{pow, min}} < R < R_{\text{pow, max}}$, where $\Delta\Sigma_0$ is in units of $h M_{\odot} \text{pc}^{-2}$. Given this definition, the power laws that went into Fig. B1 are described in Table B1.

B2 Correction for physically associated sources

The boost factors (equation 33) that implicitly went into those signals are shown in Fig. B2. As shown, the correction is very small (\sim per cent level) on the scales used for this measurement, $\gtrsim 2 h^{-1}$ Mpc. The size of the error bars indicates that there are ~ 1 per cent-level density fluctuations in the real catalogue on large

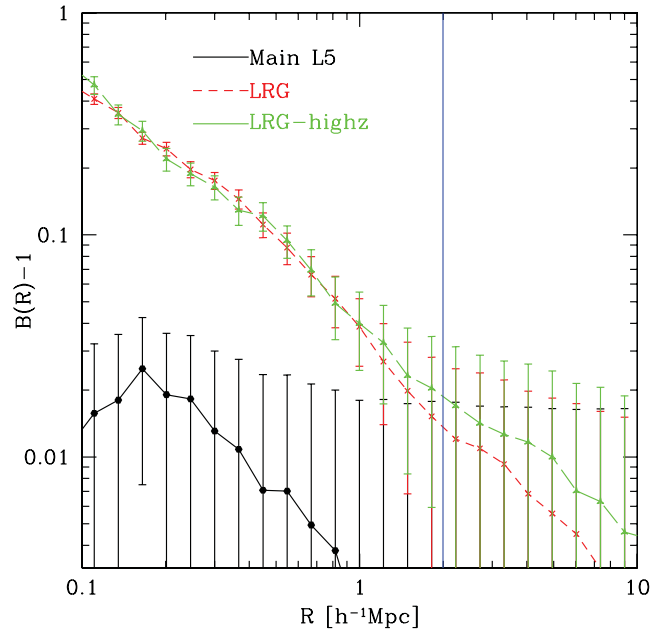


Figure B2. Boost factors $B(R) - 1$ as a function of separation for the three samples used in this analysis, as labelled on the plot. The vertical solid line at $R = 2 h^{-1}$ Mpc indicates the physical scales used for the cosmological constraints in this paper.

scales, perhaps due to dependence of the lens number density on systematics that are not properly reproduced in the random catalogues. This does not bias the lensing signal, it simply acts as a minor contribution to the statistical error budget, subdominant to shape noise.

B3 Intrinsic alignments

We must consider the contribution of intrinsic alignments to our measurement. In principle, they should only contribute if photo- z errors scatter galaxies that are actually physically associated with our lenses into the source sample, and if those physically associated galaxies have a tendency to align radially or tangentially with respect to our lenses. In principle, we expect a radial alignment for elliptical galaxies, which should follow the linear alignment model to some extent (Hirata & Seljak 2004); this alignment has been observed (e.g. Hirata et al. 2007) but primarily for bright red galaxies, rather than the faint ones that we use as sources in our lensing analysis. Disc galaxies are expected to align in a way that relates their disc angular momentum to the dark matter halo angular momentum, which leads to essentially no net radial or tangential alignment with respect to lens galaxies (Hirata & Seljak 2004).

Thus, our approach here is to assume that blue sources, which contribute ~ 70 per cent of the weight to the lensing measurement, contribute zero intrinsic alignment, and red sources contribute some amount that we must empirically constrain. A method for carrying out this empirical constraint is presented in Blazek et al. (2012); it relies on calculating shears of sources selected in different photo- z bins with respect to the lenses. That work shows that using this method, we can constrain intrinsic alignment contamination of the galaxy–galaxy lensing signal at $10 h^{-1}$ Mpc (the scale which roughly dominates our lensing constraints) to < 2 per cent for our LRG lens sample (which has the lowest statistical error and therefore is the most demanding in terms of systematics). Assuming that ~ 30 per cent of the source sample has at most a 2 per cent intrinsic alignment contamination, this translates to < 0.6 per cent intrinsic alignment contamination of our lensing signals. This is far subdominant to our other assumed systematic errors (e.g. 4–5 per cent for lensing calibration), so we assume that it is negligible for the purpose of these cosmological constraints.

B4 Ratio test

As described in Section 4.2.1, we apply a number of corrections for known sources of calibration bias such as photo- z error. To support the claim that we understand these effects well, we carry out ratio tests of the signals computed using the same lens sample and different source samples. After correcting for known calibration biases that are different for each sample, these ratios should simply be consistent with one within the errors (which are typically ± 0.06).

There are several ratio tests that we can carry out, each of which is sensitive to our understanding of several effects. For example, when dividing the sample into red and blue galaxies, we are most sensitive to differences in photo- z errors and to differences in the intrinsic ellipticity distribution of the red and blue galaxy populations. When dividing into faint versus bright galaxies, we are most sensitive to noise rectification bias and photo- z errors in the former. When dividing into well- versus poorly resolved galaxies, we are most sensitive to selection biases that couple the shear to the apparent size. When dividing into all sources versus only those with $z_{\text{phot}} > 0.45$, we are most sensitive to photo- z errors in the former (the photo- z errors in the latter are less important because of the larger redshift

separation between lenses and sources). Therefore, an ability to achieve a ratio of one in each of these four cases would suggest that we understand the different systematic errors that are affecting the lensing signals in each case well enough to constrain cosmology at the ~ 5 per cent level.

Our finding, using the LRG lens sample, is that in three cases the ratio is within 1σ of one. In the final case, the split into red versus blue sources, the ratio is 0.92 ± 0.06 ; thus the discrepancy is only a little more than 1σ , and since we expect such a case to turn up after doing several ratio tests, we conclude that the ratio tests do not indicate any major misunderstanding of the predominant systematic errors affecting the lensing calibration.

B5 Large-scale systematic shear

In this section, we present tests of the large-scale shear systematics. As noted in Mandelbaum et al. (2005), the presence of a coherent PSF ellipticity along the scan direction in the SDSS data can result in a non-zero tangential shear on large scales, where lens–source pairs may be lost due to survey edge effects. There, we corrected for this effect by subtracting off the g – g lensing signal around random points, but also noted that if the systematic shear correlates in some way with the lens number density, this correction may not be sufficient. Thus, we must test the accuracy of this procedure when using large-scale lensing signals to constrain cosmology.

In Fig. B3, we show the g – g lensing signal around random points for our three lens samples. As shown, it becomes significantly inconsistent with zero for scales above 10, 20 and 15 h^{-1} Mpc for Main-L5, LRG and high- z LRG, respectively. The reason for the different scales is that it is a systematic associated with an angular scale, which becomes different physical scales when we convert angular separation θ to R at the different typical lens redshifts. However, its magnitude also depends on the apparent magnitude and resolution factors of sources used, as we have confirmed

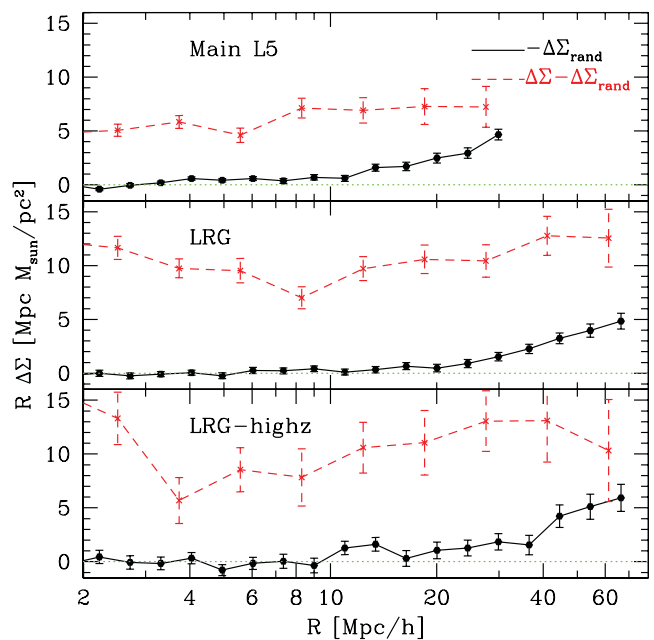


Figure B3. The black points and lines show $-R\Delta\Sigma_{\text{rand}}$, a measure of systematic shear in the source catalogue. Each panel is a different sample (Main-L5, LRG, LRG-highz from top to bottom). For reference, the actual signal that we use for science is also shown as the red dashed lines.

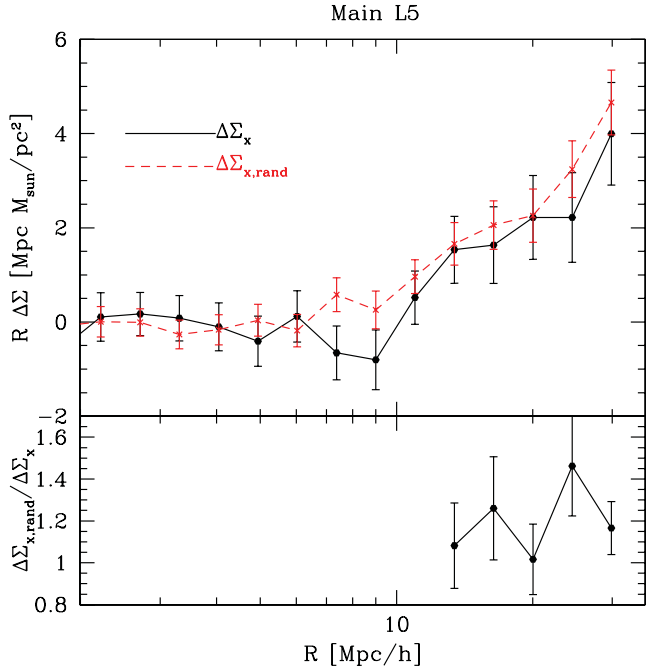


Figure B4. Top: the black solid and red dashed lines show $R\Delta\Sigma_{\times}$ and $R\Delta\Sigma_{\times,\text{rand}}$, respectively, for the Main-L5 sample. Bottom: for the scales that have a significant systematic shear signal, we show the ratio $\Delta\Sigma_{\times,\text{rand}}/\Delta\Sigma_{\times}$.

explicitly by dividing our source sample by source properties.²⁷ These two effects go in competing directions, driving the typical scale of the systematic error to increasing R as z increases, then at a certain point above $z \sim 0.3$, the typical scale starts to decrease again. For reference, this figure also shows the observed signal around real lenses in the same form ($R\Delta\Sigma$), to show at which point the systematic correction is comparable in size. Generally, on the maximum scale used for science, the systematic correction ranges from 1/3 to 1/2 of the real signal, and is one to two times larger than the statistical error.

Given the significance of this systematics signal on the largest scales used for our measurements, we must assess whether the assumptions behind the correction for it are correct (cf. Section 4.2). In order to do so, we rely on the following facts. First, if there is some coherent systematic shear, then depending on the survey geometry, it can also show up as a signal in the other shear component γ_{\times} on large scales. Secondly, there is no gravitational lensing signal in that shear component. Thus, we measure $\Delta\Sigma_{\times}$ around real lenses and $\Delta\Sigma_{\times,\text{rand}}$ around random points, and check to see whether they are consistent. An inconsistency would call into question the validity of this correction using random points.

As shown in Fig. B4 for one of the lens samples, we find that there is a significant signal in the \times shear component on the same scales as for the $+$ component, and $\Delta\Sigma_{\times,\text{rand}} \approx 1.25\Delta\Sigma_{\times}$ (actually it is $\sim 1.2\Delta\Sigma_{\times}$ in this figure; 1.25 is the result if we average over all the lens samples to reduce the noise). Taken at face value, this suggests that the systematic shear correlates with some factor that determines the effective lens number density, and that correlation is *not* properly taken into account by our procedure for producing

²⁷ This result is expected, because systematic errors in determination of the shear generically depend on both the S/N and apparent size of the source compared to the PSF; e.g. Bridle et al. (2010) and Kitching et al. (2012).

random catalogues. This finding is also consistent with the results in Section B2. There is likely a simple physical explanation for this issue related to the data processing; for example, very slight correlations of lens selection probability with the PSF full width at half-maximum, extinction, or sky level should also correlate with fluctuations in the systematic shear in the sources.

We consider the implications for the LRG sample, as an example. That sample has $\Delta\Sigma \sim 0.30 \pm 0.03$ and $\Delta\Sigma_{\text{rand}} \sim -0.10$ at $50 h^{-1} \text{Mpc}$. If we assume that $\Delta\Sigma_{\text{rand}}$ is overestimating the true systematic shear by a factor of 1.25, then that means we should have been subtracting -0.08 , not -0.10 , from the original signal to get our final $\Delta\Sigma$. Thus, our original $\Delta\Sigma$ should have been 0.28 ± 0.03 , a shift of $(2/3)\sigma$. The size of this correction compared to the statistical error suggests that we should impose the correction by simply dividing $\Delta\Sigma_{\text{rand}}$ by 1.25 before subtracting it to get our estimate of the lensing signal. Indeed, we applied corrections in this way to all signals used for science and shown in all plots in this paper.

As an additional test, we computed the signal while excluding all LRGs within $60 h^{-1} \text{Mpc}$ of a survey edge. The resulting systematic shear signal was consistent with zero, and the value of $\Delta\Sigma$ was unchanged on average on small scales, and decreased at the expected level on the largest scales. However, we merely present this test to validate our correction scheme; we do not use the signal with survey edges removed for science, because the statistical errors on a few $h^{-1} \text{Mpc}$ scales increase significantly (20 per cent).

Finally, we note that a non-negligible fraction of this systematic shear signal (~ 30 – 40 per cent) is due to an error in the SDSS PSF model identified in R12, which resulted in all PSF models in the r band in one of the camera columns having some spurious ellipticity. The remainder is due to the inadequacy of the adopted PSF correction method at removing the PSF ellipticity from the galaxy shapes.

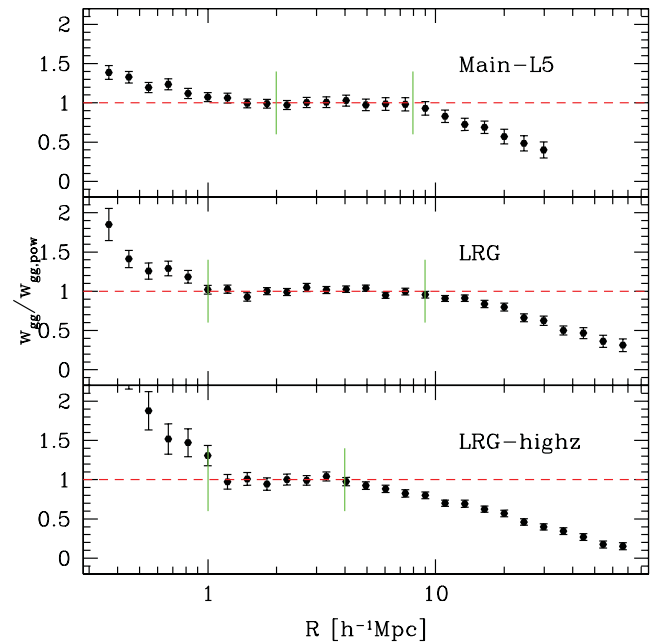


Figure C1. Clustering signals for the three samples (as labelled on the plot) divided by the best-fitting power law using the range of scales indicated by vertical solid lines. The horizontal dashed line shows the ideal value $w_{gg}/w_{gg,\text{pow}} = 1$.

APPENDIX C: GALAXY CLUSTERING SYSTEMATICS TESTS

C1 Calculation of Υ_{gg}

Since we use Υ_{gg} for our cosmological parameter constraints, and it is a derived quantity that relies on determination of $w_{\text{gg}}(R_0)$, here we present tests illustrating the accuracy of that determination.

As for the lensing signal $\Delta\Sigma$, we determine $w_{\text{gg}}(R_0)$ using power-law fits over a range of scales including R_0 on which w_{gg} appears consistent with a power law. In Fig. C1, we show (for all three samples) the observed $w_{\text{gg}}(R)$ divided by the best-fitting power law for the chosen range of scales which are indicated by vertical lines. This power law is determined from a fit to the jackknife mean w_{gg} , weighted by the inverse variance (assumed to be diagonal on these scales). Ideally, this ratio of observed signal to best-fitting power law would be consistent with the one between the vertical lines. It is clear that the power-law approximation is valid on the range of scales used, but the observed signal deviates from it strongly

Table C1. Best-fitting power-law functions (as defined in Section C1) to $w_{\text{gg}}(R)$ for a limited range of scales, used to estimate $w_{\text{gg}}(R_0)$ and therefore Υ_{gg} .

Sample	$R_{\text{pow, min}}$ (h^{-1} Mpc)	$R_{\text{pow, max}}$ (h^{-1} Mpc)	w_0 (h^{-1} Mpc)	β
Main-L5	2.0	8.0	35.4	−0.71
LRG	1.0	9.0	75.7	−0.83
LRG-highz	1.0	4.0	88.0	−0.64

outside of that range, which is what we expect for Λ CDM and typical models of scale-dependent bias.

The best-fitting power laws and ranges of scales used are defined as $w_{\text{gg}} = w_0(R/R_0)^\beta$ for $R_{\text{pow, min}} < R < R_{\text{pow, max}}$, where w_0 is in units of h^{-1} Mpc. Given this definition, the power laws that went into Fig. C1 are given in Table C1.

This paper has been typeset from a \LaTeX file prepared by the author.